Periodically Poled Ridge Waveguides and Photonic Wires in $LiNbO_3$ for Efficient Nonlinear Interactions

Thesis

Submitted to the
Department of Physics, Faculty of Science
University of Paderborn, Germany
for the degree
Doctor der Naturwissenschaften (Ph.D / Dr. rer. nat.)

By

Li Gui

Reviewers:
1. Prof. Dr. W. Sohler
2. Prof. Dr. K. Lischka

Date of the submission: November 12, 2010
Date of the defence examination: December 20, 2010

Abstract

Periodically poled $LiNbO_3$ (PPLN) waveguides have been successfully used for efficient nonlinear interactions using quasi phase matching (QPM) due to the fact that the optical wave is confined in the waveguide with a high intensity. A further increase in nonlinear conversion efficiency requires strongly reduced cross section dimensions which can be only achieved in a waveguide of a high refractive index contrast. Such a waveguide not only facilitates efficient nonlinear interactions but also enables fabrication of sub-micrometer periodical domain structures. Therefore, counter-propagating nonlinear interactions can be realized.

The aim of this work is to develop PPLN waveguides of high refractive index contrast and small cross sectional dimensions, and then to investigate various nonlinear interactions in such waveguides. Towards this goal, two different types of $LiNbO_3$ waveguides, i.e. ridge waveguides on X(Y)-cut substrates and $LiNbO_3$-on-Insulator (LNOI) photonic wires, are developed. The methods of fabricating periodical domain structures in such waveguides are investigated to enable quasi-phase-matching (QPM) nonlinear interactions.

First, ridge waveguides on X(Y)-cut $LiNbO_3$ substrates are fabricated using plasma etching and a subsequent Ti in-diffusion. A local poling technique is developed to fabricate periodical domain structures only in the body of the ridge guide. Various characterization methods have been used to evaluate the quality of the ridge guides as well as the periodical domain structures. A reduced mode size compared to a conventional Ti in-diffused channel waveguide is observed. The inverted domains inside the body of the ridge are sufficiently deep ($\sim$5 μm) to overlap the transmitted optical modes. As a result, a normalized SHG conversion efficiency of 16.5 % $W^{-1}cm^{-2}$ is obtatined, which is 50 % higher than that in a conventional Ti in-diffused channel waveguide. Moreover, as a promising feature, a strongly reduced sensitivity to photorefactive effects is observed. This could be of strong interest for the nonlinear applications using high optical power.

Second, periodically poled $LiNbO_3$-on-Insulator (PPLNOI) material platform is fabricated by direct bonding of PPLN in collaboration with Hu. PPLNOI photonic wires are then fabricated using Argon milling. 1st order SHG is demonstrated using a PPLNOI photonic wire of 3.2 μm periodicity; a parabolic dependence of the generated SH power vs. the fundamental power is observed. We also demonstrate the second approach of fabricating PPLNOI by directly poling $LiNbO_3$ thin film. The promises as well as challenges presented in our preliminary experiments are discussed in detail.

Contents

List of Figures

List of Tables

Chapter 1

Introduction

1.1 Motivation

The concept of integrated optics is using an optical waveguide as a basic structure to implement compact and robust devices which perform complicated functions for specific applications by integration. It was first introduced in the late 1960's. Since then, a lot of waveguide devices such as optical modulators, amplifiers and etc. have been developed and implemented in areas such as optical memories, optical sensors, and most successfully optical communications. By applying waveguide technologies in nonlinear optics, one can realize highly efficient nonlinear interactions. This is because that optical waves can be confined in a small cross section and maintained with high optical intensity over a long propagation length. Moreover, using a waveguide offers new possibilities in phase matching and various nonlinear interactions. Therefore, it is possible to develop multifunctional devices by integrating different nonlinear optical functions and/or peripheral waveguide components performing passive and active functions. Such an integration is essential for future applications.

$LiNbO_3$, also often referred to as "the silicon of nonlinear optics", is an excellent candidate for this application because of the following reasons: First, $LiNbO_3$ of optical quality is produced using well established techniques and available worldwide. Second, $LiNbO_3$ is transparent from 350 nm to 4.5 μm, providing low loss for both the fundamental and harmonic for visible light generation. Third and most important, $LiNbO_3$ has nonlinear coefficients among the largest of all inorganic materials. Last but not least, by taking advantage of the established technologies in $LiNbO_3$ integrated optics, one can make a complex optical circuit combining both linear and nonlinear functionalities on one single chip. In the last few decades, $LiNbO_3$ waveguides and quasi phase matching (QPM) technologies have been intensely investigated. However, the challenges always exist in several aspects. One is to achieve high nonlinear efficiency and stability, so that the high power light source based on nonlinear interaction can be realized. The other aspect is to realize versatile interactions, some of which one can not normally achieve using existing technologies, for example, counter propagating nonlinear interactions. Attractive applications of such a counter propagating nonlinear interactions include for example mirrorless optical parametric oscillator (OPO). The research presented in this

thesis was directed towards investigating new techniques of fabricating $LiNbO_3$ waveguides to achieve an enhanced nonlinear efficiency and lead a way in realizing counter propagating nonlinear interactions in $LiNbO_3$.

Developing a suitable material platform for the nonlinear interactions of interest is the starting point of this research. The strategy for developing such a material platform is briefly discussed in the next section. The central contributions of this research are then listed, followed with an overview of this dissertation.

1.2 Strategy for material development

$LiNbO_3$ Waveguide

$LiNbO_3$ is a synthetic dielectric material that doesn't exist in nature. It was first discovered to be ferroelectric in 1949 [5]. $LiNbO_3$ was first synthesized in single crystal form and investigated in detail at Bell Laboratories. This resulted in a cornerstone series of publications in 1966 about the structure and properties of this material [6, 7, 8, 9, 10]. Fabricating $LiNbO_3$ waveguides is essential for its use in integrated optics. Designing a waveguide for a specific application requires comprehensive consideration of the crystallographic orientation of the wafer, the composition of the material, the required refractive index contrast and most importantly the available fabrication techniques.

The key technique behind waveguide fabrication is to increase the refractive index of the material in a certain region where the light can be confined inside. Many techniques have been proposed over decades, some of them are well established such as Ti in-diffusion and proton exchange. However, proton exchanging only increases the extraordinary index, bringing a certain limitation for applications. In comparison, Ti in-diffusion increases both ordinary and extraordinary indices, and has been demonstrated with high performance of various functional devices.

The conventional $LiNbO_3$ waveguides are generally small channels under the surface of the wafer as sketched in figure 1.1(a). The light confinement is achieved due to the increase of the refractive index in the region of treatment (either Ti in-diffusion, proton exchange or etc.), except for the interface between the air and $LiNbO_3$ where the air has the refractive index of 1, much smaller than that of $LiNbO_3$($\sim$2.2). Intuitively, one might imagine to improve the light confinement greatly by using the interface between $LiNbO_3$ and air. This gives rise to the concept of a ridge waveguide as sketched in figure 1.1(b). Several works have been reported to fabricate $LiNbO_3$ ridge waveguides [11, 12, 13]. Hu et.al. demonstrated that a Ti in-diffused ridge waveguide on a Z-cut $LiNbO_3$ substrate fabricated by using wet-etching has a smaller mode size compared to a conventional channel waveguide [13]. Similar work can be done also in X- or Y-cut substrates but with a different technique [14]. Even though X- and Y-cut substrates are less frequently mentioned in the literature, they are favored for many applications such as a fully integrated optical parametric oscillators, where frequency conversion and electro- and acoustooptic functions are to be integrated in the same substrate.

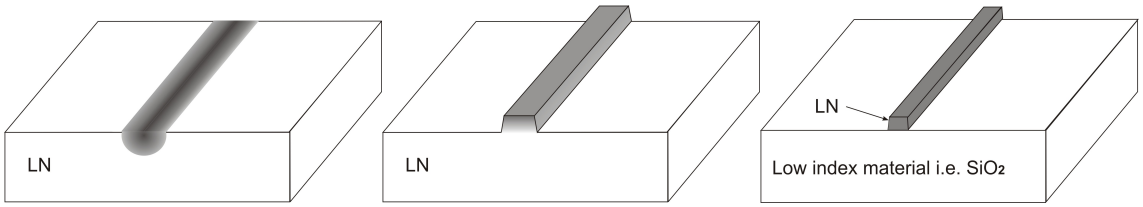

Figure 1.1: A sketch of (a) a conventional channel waveguide, (b) a ridge waveguide and (c) a LNOI photonic wire.

Inspired by silicon on insulator, so called "SOI" in the semiconductor industry [15, 16], the idea of $LiNbO_3$-on-Insulator (LNOI) waveguides also called "photonic wires" came naturally, but was not realized until the very recent years [17, 18, 19, 3]. A LNOI thin film is fabricated by ion-slicing and crystal bonding. A photonic wire is then fabricated on such a thin film as depicted in figure 1.1(c): the $LiNbO_3$ channel is sitting on top of the low index material SiO_2. Owing to the high contrast between the index of refraction of $LiNbO_3$ and the surrounding material, the dimensions of the waveguide can be as small as sub-micrometer for single-mode transmission. High index contrast also means that small-radius devices can be made. Therefore, high density integration becomes possible. Concerning the nonlinear interaction, the high index contrast and the small cross section of the waveguide result in extremely small mode size and excellent overlap of different modes, leading to an extremely high nonlinear efficiency. Moreover, with the size of the $LiNbO_3$ waveguide so small, periodically inverted domain structures (also referred to a "QPM" structure in this work) of a wavelength scale becomes achievable. Therefore, a broader range of nonlinear interactions, such as counter propagating nonlinear interactions, can be realized in $LiNbO_3$.

Essentially, both ridge waveguide and LNOI photonic wire are ridge-type waveguides. In this thesis, in order to avoid confusion, we refer "ridge waveguide" specifically to a ridge guide on a bulk $LiNbO_3$ substrate, and refer "photonic wire" to a waveguide fabricated in a LNOI thin film.

Periodical domain structures in $LiNbO_3$ waveguides

Periodical domain structures (QPM structures) are essential to obtain efficient nonlinear interactions in $LiNbO_3$ waveguides. $LiNbO_3$'s crystal structure and the concept of spontaneous polarization needs to be discussed first in order to understand this technique. As a typical ferroelectric material, $LiNbO_3$ has both paraelectric and ferroelectric phases. Figure1.2 (a) shows $LiNbO_3$'s crystal structure in its paraelectric phase at temperatures above its ferroelectric Curie temperature ($\sim$1200 °C). In the paraelectric phase, the lithium ions sit in an oxygen plane and the niobium ions are centered between two oxygen planes. These positions make the paraelectric phase non-polar [10]. When the temperature decreases from the Curie temperature, the lithium ions and niobium ions are forced to move into new positions. The positions of the lithium ions are equally

probable to be either above or below the oxygen plane, as shown in 1.2 figures (b) and (c). The charge separation resulting from this shift of ions relative to the oxygen octahedra causes $LiNbO_3$ to exhibit a spontaneous polarization. The spontaneous polarization is reversed when the lithium ions are moved from above the oxygen plane to below the oxygen plane (at the same time niobium ions are moved in the same direction with a smaller displacement) under the influence of, for example, an external electrical field. This process is called "domain inversion". A QPM structure requires a periodically reversed polarization along the propagation direction as sketched in figure 1.3. Theoretical analysis of a QPM nonlinear interaction is presented in chapter 2.

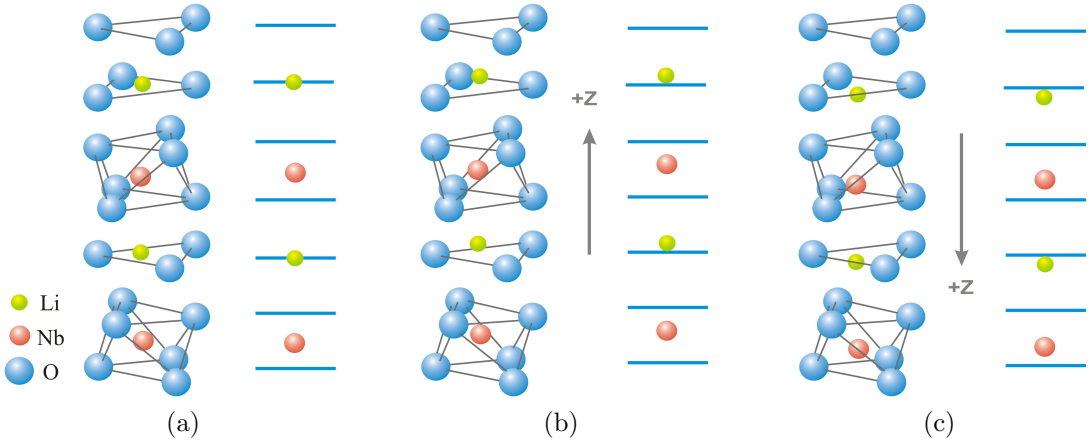

Figure 1.2: Atomic structure of $LiNbO_3$ in (a) paraelectric phase and (b, c) ferroelectric phases.

To create QPM structures in $LiNbO_3$, various approaches have been studied such as stacking of alternately oriented thin plates, or growth of periodic domain structures in ferroelectrics [20]. For waveguides where QPM is required only at the surface of the crystal, periodic annihilation of the nonlinear coefficient and periodic domain inversion by dopant in-diffusion in ferroelectrics [21, 22] have been employed. Years later, Yamada, et al. first reported bulk periodic domain formation in ferroelectrics by applying an electric field using lithographically defined periodic electrodes [23]. This last technique is referred to as electric field periodic poling. The electric field periodic poling has been explored mostly in a Z-cut $LiNbO_3$ substrate; a resulted periodically poled $LiNbO_3$ (PPLN) waveguide is sketched in figure 1.3 (a). The poling only succeeds when the electric field applied between +Z face and −Z face is high enough to overcome the coercive field E_c, generally ∼21 kV/mm for congruently melted $LiNbO_3$.

The periodic poling of a X- or Y-cut substrate has to be done differently to a Z-cut substrate because the direction of the spontaneous polarization is parallel to the surface as sketched in figure 1.3 (b). Several approaches have been proposed [24, 25, 26, 27, 28] to fabricate periodic domain structures on the planar substrate. Periodically poled ridge guides can be fabricated by lapping, polishing and mechanical micro-machining periodically poled $LiNbO_3$ (PPLN) layers, glued or bonded, respectively, to a $LiNbO_3$ substrate [12, 29]. The challenge of periodic poling in a X- and Y-cut substrate is that it is difficult

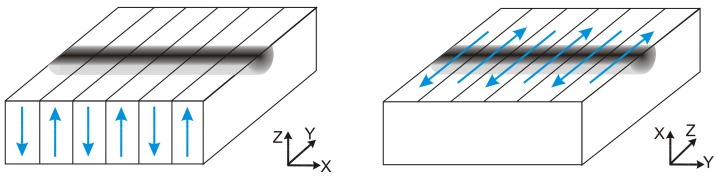

(a) (b)

Figure 1.3: Sketch of a PPLN waveguide on (a) Z-cut and (b) X-cut substrate. Arrows indicate the orientation of the Z axis.

to get the reversed domain deep enough to overlap the optical modes. Recently, a deep domain inversion in an 84 μm wide ridge on X-cut $LiNbO_3$ with a proton exchanged channel guide in its center was reported [30]. In the research presented in this thesis, a technique of fabricating QPM structures only in the ridge waveguide ("local periodic poling") is developed. A 14 mm long PPLN ridge waveguide on a X-cut substrate is fabricated and nonlinear interactions including SHG and cascaded interaction of SHG and difference frequency generation (DFG) are demonstrated.

Another task of this research is to fabricate QPM structures in LNOI thin films and furthermore periodically poled photonic wires, and to investigate nonlinear interactions in such a photonic wire. Compared to $LiNbO_3$ crystal we discussed above, an ion-implanted $LiNbO_3$ thin film has several special features. First, the LNOI thin film has been treated with a sequence of processes, including high dose ions implantation and annealing, in order to achieving successful bonding and splitting. Second, the film has a thickness of sub-micrometer. Third, surface defects are unavoidable from the fabrication process. All these features make the poling process significantly different from poling of a bulk $LiNbO_3$ crystal. Several methods are developed in this work to fabricate QPM structures in LNOI thin film.

1.3 Overview of this thesis

The central contribution of this research consists of two parts:

Part I : Techniques of fabricating periodically poled ridge waveguides on X- and Y-cut $LiNbO_3$ substrates are developed. Simulations of the optical modes and the interaction cross section, show a moderate improvement of both values, in turn an enhanced nonlinear efficiency. Two nonlinear interactions using such a ridge guide are studied: (i) second harmonic generation (SHG); (ii) cascaded interaction of SHG and difference frequency generation (Cascaded SHG/DFG). Experimental results are presented and discussed.

Part II: Fabrication and characterization of QPM structures in LNOI thin films and in LNOI photonic wires are investigated. Two methods are developed including (i) directly bonding of a PPLN substrate; (ii) domain inversion directly in $LiNbO_3$ thin

films. Periodically poled LNOI photonic wires are fabricated, and nonlinear interactions in photonic wires are studied.

Essential information about QPM nonlinear interaction, including a theoretical analysis of the nonlinear interactions studied in this work is presented in Chapter 2. Part I of this research is presented in Chapters 3 to 5. Chapter 3 introduces the techniques of fabricating a ridge waveguide on a X-cut substrate using plasma etching and the subsequent local periodic poling. Chapter 4 presents the characterizations of the ridge waveguide and periodic ferroelectric domains. Chapter 5 presents and discusses the simulation and experimental results of SHG and cascaded SHG/DFG in the waveguide described in chapter 3. Part II of this research is presented in Chapter 6. It includes the fabrication of LNOI thin films and photonic wires and different methods of fabricating periodically poled LNOI films. Last but not least, Chapter 7 concludes this dissertation and provides some suggestions for future work.

Appendix A presents the fabrication of sub-micron periodic photoresist gratings by using holographic lithography. This technique has been used in this work to fabricate periodical domains in bulk $LiNbO_3$ substrates as well as in periodically poled LNOI thin films.

Chapter 2

Theoretical background of QPM nonlinear interaction

Nonlinear optics deals with nonlinear interaction of light with matter. At high light intensities, a nonlinear response of the medium is induced. The nonlinear polarization is excited, which leads to the generation of a new electric field or modification of the phase and amplitude of the input optical wave. Numerous nonlinear optical phenomena have been discovered since 1961, when Franken et al. reported the first second harmonic generation (SHG) observed from a quartz crystal [31]. In this chapter, a theoretical analysis of second-order nonlinear interaction in waveguide structures is briefly discussed for understanding this physical phenomenon from the viewpoint of device design. Basic concepts are presented in this chapter; more detailed discussions can be found in textbooks [32, 33].

In this chapter, the nonlinear polarization induced by the electric field of an optical wave is introduced. The coupled-mode method is then used to describe the nonlinear interaction. Coupled-mode equations of two nonlinear interactions are studied in this research: SHG and cascaded SHG/DFG. The formulars are derived and discussed. The concept of QPM is introduced afterwards. The advantages of using a ridge guide and a LNOI photonic wire for nonlinear interactions are briefly discussed in the last section.

2.1 Nonlinear polarization and coupled-mode equations

In an optical medium, a dielectric polarization $\vec{P}$ is induced by the electric field of an optical wave $\vec{E}$. $\vec{P}$ can be expressed in general as (2.1).

$$\vec{P} = \varepsilon_0 \left\{ \chi^{(1)}\vec{E} + \chi^{(2)}\vec{E}\vec{E} + \chi^{(3)}\vec{E}\vec{E}\vec{E} + ... \right\}, \tag{2.1}$$

where ε_0 is the permittivity of vacuum, $\chi^{(q)}$ is the dielectric susceptibility tensor of the q-th order. The first term in (2.1) is the linear polarization. The second-order

nonlinear polarization $\vec{P}^{(2)} = \varepsilon_0 \chi^{(2)} \vec{E}\vec{E}$ is crucial for three-wave (with frequency ω_1, ω_2, ω_3 respectively) mixing processes i.e. SHG, when ω_3=$2\omega_1$=$2\omega_2$, and DFG, when ω_3=ω_1-ω_2. Often a tensor $\boldsymbol{d}$ is introduced as $\boldsymbol{d}_{ijk} = \frac{1}{2}\chi^{(2)}_{ijk}$. According to the Kleinman symmetry [34], $\boldsymbol{d}$ can be represented as a 3×6 matrix; for $LiNbO_3$ (point group: 3m) it takes the form:

$$\boldsymbol{d} = \begin{bmatrix} 0 & 0 & 0 & 0 & d_{31} & -d_{22} \\ -d_{22} & d_{22} & 0 & d_{31} & 0 & 0 \\ d_{31} & d_{31} & d_{33} & 0 & 0 & 0 \end{bmatrix}. \tag{2.2}$$

For simplicity, we assume purely transverse-mode fields in the waveguide (i.e. the TE and TM approximation). We therefore have only one transverse component of the electric fields of the wave, either parallel or perpendicular, with respect to the waveguide surface. Thus the electric field of the wave at frequency ω can be expressed as

$$\vec{E}_\omega(x, y, z, t) = \frac{1}{2}\left\{A(z)\mathscr{E}(x, y)exp[i(\omega t - \beta z)] + c.c.\right\}, \tag{2.3}$$

where $A(z)$ is the slowly varying amplitude, $\mathscr{E}(x, y)$ is the transverse-mode field distribution, β is the propagation constant, "c.c." stands for complex conjugation.

The electric field of the optical waves in the waveguide is

$$\vec{E} = \vec{E}_{\omega_1} + \vec{E}_{\omega_2}, \tag{2.4}$$

Substituting (2.3) into (2.4), and using d_{eff} denotes the effective value of $\boldsymbol{d_{ijk}}$ (in turn, $\chi^{(2)}_{ijk}$) for the actual process, the nonlinear polarization $P^{(2)}$ induced by the electric field $\vec{E}$ can be written as

$$P^{(2)} = \varepsilon_0 d_{eff}\vec{E}^2 = \varepsilon_0 d_{eff}\left(\vec{E}_{\omega_1} + \vec{E}_{\omega_2}\right)^2. \tag{2.5}$$

$$\begin{aligned} P^{(2)} = \varepsilon_0 d_{eff}\Big(&\frac{1}{4}A_1^2(z)\mathscr{E}_1^2(x, y)e^{i(2\omega_1 t - 2\beta_1 z)} + \frac{1}{4}A_2^2(z)\mathscr{E}_2^2(x, y)e^{i(2\omega_2 t - 2\beta_2 z)} \\ &+ \frac{1}{2}A_1(z)A_2(z)\mathscr{E}_1(x, y)\mathscr{E}_2(x, y)e^{i((\omega_1+\omega_2)t - (\beta_1+\beta_2)z)} \\ &+ \frac{1}{2}A_1(z)A_2^*(z)\mathscr{E}_1(x, y)\mathscr{E}_2^*(x, y)e^{i((\omega_1-\omega_2)t - (\beta_1-\beta_2)z)} \\ &+ \frac{1}{2}A_1(z)A_1^*(z)\mathscr{E}_1(x, y)\mathscr{E}_1^*(x, y) + \frac{1}{2}A_2(z)A_2^*(z)\mathscr{E}_2(x, y)\mathscr{E}_2^*(x, y) \\ &+ c.c.\Big). \end{aligned} \tag{2.6}$$

For a defined three-wave mixing (ω_3=$\omega_1 \pm \omega_2$), only one term from the right side of (2.6) possibly contributes the appreciable intensity in the generated radiation. The reason for this behavior is that the nonlinear polarization can efficiently produce an output signal only if a certain phase matching condition (which will be discussed at the end of this section) is satisfied, and usually this condition cannot be satisfied for more than one frequency component of the nonlinear polarization.

$$P_{\omega_3} = \varepsilon_0 d_{eff}A_1(z)A_2(z)\mathscr{E}_1(x, y)\mathscr{E}_2(x, y)e^{i((\omega_1+\omega_2)t - (\beta_1+\beta_2)z)}, \tag{2.7}$$

$$P_{\omega_3} = \varepsilon_0 d_{eff} A_1(z) A_2^*(z) \mathscr{E}_1(x,y) \mathscr{E}_2^*(x,y) e^{i((\omega_1-\omega_2)t-(\beta_1-\beta_2)z)}. \tag{2.8}$$

The equation (2.7) describes sum frequency generation (SFG) and (2.8) is associated to difference frequency generation (DFG).

The reason why the polarization plays a key role in the description of nonlinear optical phenomena is that a time-varying polarization can act as the source of new components at different frequencies of the electromagnetic field. The nonlinear wave equation can be written as

$$\left\{ \nabla^2 - \frac{n^2}{c^2} \frac{\partial^2}{\partial t^2} \right\} \vec{E} = \mu_0 \frac{\partial^2 \vec{P}^{(2)}}{\partial t^2}, \tag{2.9}$$

where n is the refractive index at the frequency of the electric field in concern, c is the speed of light in vacuum and μ_0 is the magnetic permeability of vacuum. Substituting (2.7) into the wave equation (2.9), coupled-mode equations are then derived from (2.9) under slowly-varying amplitude approximation. The coupled-mode equations describe the evolution of the fields in the propagation direction. Let us first consider a DFG process, in which a strong pump wave at frequency ω_p is mixed with a (usually weak) signal wave at frequency ω_s to generate a frequency-shifted idler wave at frequency $\omega_i = \omega_p - \omega_s$ via the second-order nonlinear susceptibility $\chi^{(2)}$. The coupled-mode equations describing this process with the propagation losses taken into account take the following form

$$\begin{aligned}
\tfrac{\partial A_i}{\partial z} &= -\tfrac{\alpha_i}{2} A_i - i\kappa_i {A_s}^* A_p e^{-i\Delta\beta z}, \\
\tfrac{\partial A_s}{\partial z} &= -\tfrac{\alpha_s}{2} A_s - i\kappa_s {A_i}^* A_p e^{-i\Delta\beta z}, \\
\tfrac{\partial A_p}{\partial z} &= -\tfrac{\alpha_p}{2} A_p - i\kappa_p A_s A_i e^{+i\Delta\beta z},
\end{aligned} \tag{2.10}$$

where α_j $(j = p, s, i)$ is the waveguide propagation loss at the respective wavelength. The difference of the propagation constants of the interacting waves $\Delta\beta$ is defined as:

$$\Delta\beta = \beta_p - \beta_s - \beta_i \ , \tag{2.11}$$

$$\kappa_j = \frac{d_{eff}\omega_j}{c n_j} \cdot \frac{\iint \mathscr{E}_s(x,y) \mathscr{E}_i(x,y) \mathscr{E}_p(x,y) \, \mathrm{d}x \, \mathrm{d}y}{\iint {\mathscr{E}_j}^2(x,y) \, \mathrm{d}x \, \mathrm{d}y}, \ j = p, s, i. \tag{2.12}$$

Solution

The solution of the equations (2.10) generally can only be expressed in integral formats and require numerical integration to obtain the results. For simplicity, we assume the waveguide is lossless, the input pump power is much larger than the signal power, i.e. $|A_{p,0}| \gg |A_{s,0}|$ and the DFG conversion efficiency is low, i.e. the pump power can be taken as constant in the waveguide. The last assumption is also known as

undepleted pump approximation. The equations (2.10) for an interaction through the propagation length L are then solved using the boundary condition $A_{i,0} = 0$ as

$$\begin{aligned} A_p(L) &= A_{p,0}, \\ A_s(L) &= e^{i\frac{\Delta\beta}{2}L} A_{s,0}[\cosh gL + i\frac{\Delta\beta}{2g}\sinh gL], \\ A_i(L) &= -i\kappa_i e^{-i\frac{\Delta\beta}{2}L}\frac{1}{g}A_{p,0}\sinh gL. \end{aligned} \tag{2.13}$$

$$g = \sqrt{\kappa_i\kappa_s|A_{p,0}|^2 - (\frac{\Delta\beta}{2})^2}. \tag{2.14}$$

Where the power of the optical wave is calculated as

$$P_j = \frac{\varepsilon_0 c n_j |A_j|^2}{2}\iint \mathscr{E}_k^{\,2}(x,y)\,\mathrm{d}x\,\mathrm{d}y,\ \ j = p,s,i. \tag{2.15}$$

The power levels of the interacting waves at the output of the waveguide ($z = L$) are

$$\begin{aligned} P_p(L) &= P_{p,0}, \\ P_s(L) &= P_{s,0}\cosh^2 gL, \\ P_i(L) &= \frac{\omega_i}{\omega_s}\frac{1}{g^2}\eta_{norm}P_{p,0}P_{s,0}\sinh^2 gL, \end{aligned} \tag{2.16}$$

$$g = \sqrt{\eta_{norm}P_{p,0} - (\frac{\Delta\beta}{2})^2}, \tag{2.17}$$

$$\eta_{norm} = \frac{2{d_{eff}}^2\omega_i\omega_s}{\varepsilon_0 c^3 n_p n_s n_i S_{eff}}, \tag{2.18}$$

$$S_{eff} = \frac{\iint \mathscr{E}_p^{\,2}(x,y)\,\mathrm{d}x\,\mathrm{d}y \iint \mathscr{E}_s^{\,2}(x,y)\,\mathrm{d}x\,\mathrm{d}y \iint \mathscr{E}_i^{2}(x,y)\,\mathrm{d}x\,\mathrm{d}y}{\left(\iint \mathscr{E}_p(x,y)\mathscr{E}_s(x,y)\mathscr{E}_i(x,y)\,\mathrm{d}x\,\mathrm{d}y\right)^2}. \tag{2.19}$$

g and η_{norm} are often called the gain coefficient and normalized conversion efficiency respectively. S_{eff}, denoted as an effective cross section, is the normalized overlap integral of the transverse mode distributions of the interacting waves. Efficiency optimization in waveguide devices requires designing the waveguide geometry to maximize the overlap integral, i.e. minimize the effective area.

The conversion efficiency of DFG is expressed as

$$\eta_{DFG} = \frac{P_i(L)}{P_{s,0}}, \tag{2.20}$$

$$= \frac{\omega_i}{\omega_s}\frac{\eta_{norm}}{g^2}P_{p,0}\sinh^2 gL, \tag{2.21}$$

$$\approx \frac{\omega_i}{\omega_s}\eta_{norm}L^2 P_{p,0}\,\mathrm{sinc}^2\,\frac{\Delta\beta}{2}L. \tag{2.22}$$

Equation (2.22) is obtained under the low gain limit, emphasizing the relationship of conversion efficiency to material properties (d_{eff} and n) and device geometry (S_{eff} and L), coupled pump power and the phase mismatching term ($\mathrm{sinc}^2(\Delta\beta L/2)$). For the perfect phase matched case where $\Delta\beta = 0$, the factor $\mathrm{sinc}^2(\Delta\beta L/2)$ approaches 1, and the intensity of the generated wave P_3 increases quadratically with z. This is because the generated wave maintains a fixed phase relation with respect to the nonlinear polarization and is able to extract energy efficiently from the pump wave. When $\Delta\beta \neq 0$, the conversion efficiency decreases as $\Delta\beta L$ increases, with some oscillations occurring. The reason for this behavior is that if L is greater than approximately $1/\Delta\beta$, the output wave becomes out of phase with its driving polarization, and the power flows from the signal and idler waves back into the pump wave. The length, through which a π phase shift is built between the output wave and its driving polarization, is defined as the coherence length L_c of the interaction.

$$L_c = \frac{\pi}{\Delta\beta}. \tag{2.23}$$

2.2 Quasi phase matching

The previous discussion shows that the phase matching condition $\Delta\beta = 0$ must be fulfilled in order to achieve efficient nonlinear interactions. This is often not automatically achieved due to the normal dispersion in the crystal. One of the established methods is using birefringent phase matching (BPM), where the anisotropy of a nonlinear crystal is used to find a unique propagation direction at which the interacting waves have the same phase velocity. However, BPM is not feasible in the integrated optics because an optical waveguide often orients along one of the crystallographic axes, at which BPM are not fulfilled. Moreover, the specific nonlinear coefficient (i.e. d_{33}, the largest nonlinear coefficient in $LiNbO_3$) can not be utilized in BPM because it requires that all the interacting waves have the same polarization, which is along Z-axis. Due to the limitations of BPM, a quasi-phase matching (QPM) technique is introduced.

The theory of QPM, first described by Armstrong, et al. [35] in 1962 and by Franken and Ward [31] in 1963, has been discussed and extended by numerous authors. In QPM, the interacting waves (for example, fundamental and SH waves in a SHG process) are allowed to have different phase velocities, and the phase difference of the wavefront of one wave relative to another reaches π over a distance called the coherence length L_c. A QPM $LiNbO_3$ structure, as shown in Figure 1.3, has a periodically inverted orientation of the Z-axis. An inversion of the direction of the Z-axis has the consequence of inverting the sign of the nonlinear coefficient d_{33}. The period Λ of the alternation of the crystalline axis is chosen equal to twice of the coherence length L_c of the nonlinear interaction. The nature of QPM is that, when each time the field amplitude of the generated wave is about to decrease as a consequence of the phase mismatch, a reversal of the sign of d_{33} occurs which allows the field amplitude to continue growing monotonically. Figure 2.1 shows, as an example, the growth of the converted SH power versus the interaction

length in BPM, QPM and non-phase matched conditions. In a non-phase matched interation, no continuous buildup of SH power is obtained. In a BPM interaction, the SH power increases parabolically. In a QPM interaction using d_{33}, the SH power grows continuously along the interaction length in a quasi-parabolic manner. With the advantage of waveguides for light confinement in mind, this growth can be maintained with high optical intensity within a long distance.

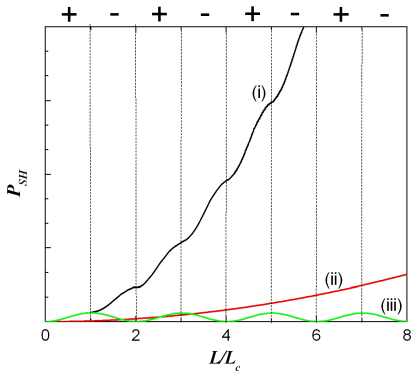

Figure 2.1: The growth of the SH power with propagation distance (divided by L_c) for (i) quasi phase matched, (ii) birefringent phase matched and (iii) non-phase matched interactions.

In a QPM structure, the spatially varying $d(z)$ can be expressed in a form of Fourier series

$$d(z) = \sum_m d_m exp(-imKz), \;\; K = \frac{2\pi}{\Lambda}, \;\; m = 1, 2, 3, ... \tag{2.24}$$

where mK is the grating vector associated with the mth Fourier component of $d(z)$. Assuming a rectangular structure of $d(z)$, the coefficient d_m given by

$$d_m = \frac{2}{m\pi} \sin(m\pi D) d_{eff}, \tag{2.25}$$

is the effective nonlinearity of the mth harmonic of the QPM grating, D is the duty cycle of the grating. Substituting $d(z)$ as nonlinear coefficient into the coupled-mode equations (2.10), the right hand sides of the equations are then expressed by a summation of the spatial harmonic terms. Only one term of them can contribute substantially to the nonlinear optical interaction, the other terms do not contribute substantially since they oscillate rapidly with z. Therefore, the coupled-mode equations have the similar form as in (2.10) with d_m as the nonlinear coefficient and $\Delta\beta$ replaced by $\Delta\beta_{QPM}$

$$\Delta\beta_{QPM} = \Delta\beta - mK. \tag{2.26}$$

The intensity of the generated wave calculated from the equation (2.16) is modified accordingly.

Most of the studies on QPM nonlinear interactions reported so far are interactions among copropagating waves as shown in figure 2.2(a). If a QPM structure with a

sufficiently short period is available, the nonlinear interaction with counter-propagating waves, e.g. backward propagation SHG, will become possible, as shown in figure 2.2(b). Calculation shows that a QPM structure for a backward propagating SHG with fundamental wavelength at 1550 nm would be ∼400 nm. There are certain advantages for counter-propagating nonlinear interaction. If both the input and output facets are antireflection (AR) coated at the fundamental wavelength, it is much easier to separate the second harmonic (SH) beam from the fundamental one. This is useful for so called mirrorless parametric oscillation [36] and parametric down-conversion (PDC). Counter-propagation interactions have unique spectral properties, for example, a much narrower spectrum width compared to that of the copropagating PDC, due to that the phase mismatch is limited by a much stricter condition. The simulation of single photon generation using counterpropagating PDC was reported by Christ et. al. [37]. It shows that the FWHM of the wavelength distribution is 0.09 nm for the backward propagating photon and 0.73 nm for the forward propagating photon. The narrow spectrum bandwidth of the backward propagating photon with no further filter required makes it well suited for a long distance transmission in optical fibers.

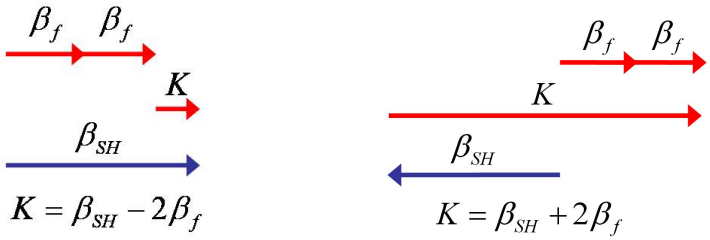

(a) (b)

Figure 2.2: Scheme of (a) a copropagating SHG and (b) a counter-propagating SHG.

2.3 Second harmonic generation

SHG is a special three-wave interaction process addressed in the first section, where two waves have the same frequency ($\omega_1 = \omega_2$) and the generated wave (ω_3) has the doubled frequency. The process is symbolically shown in figure 2.3. It can be illustrated as a process that two photons of the same frequency ω are annihilated and a photon of frequency 2ω is created. The coupled-mode equations governing SHG using a QPM waveguide can be expressed in the following form (subscripts 'SH' and 'f' denote SH wave and fundamental wave, respectively)

$$\begin{aligned} \frac{\partial A_{SH}}{\partial z} &= -\frac{\alpha_{SH}}{2} A_{SH} - i\kappa_{SH} {A_f}^2 exp[i\Delta\beta_{SHG} z], \\ \frac{\partial A_f}{\partial z} &= -\frac{\alpha_f}{2} A_f - i\kappa_f A_{SH} {A_f}^* exp[-i\Delta\beta_{SHG} z], \end{aligned} \tag{2.27}$$

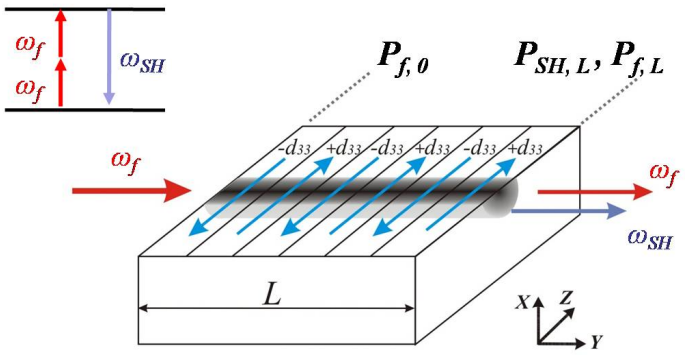

Figure 2.3: Schematic sketch of SHG in a waveguide on a X-cut $LiNbO_3$substrate. Inset: sketch of the energy conservation of SHG.

where α_{SH}, α_f are the waveguide propagation losses at fundamental and SH wavelength, respectively. Let us consider the actual interactions explored in this work, Type **I** process uses the nonlinear coefficient d_{33}, i.e. both waves have the same polarization which orients along Z-axis. The coupling coefficients are

$$\begin{aligned} \kappa_{SH} &= \frac{d_{33}\omega_{SH}}{\pi c n_{SH}} \cdot \frac{\iint \mathscr{E}_f{}^2(x,y)\mathscr{E}_{SH}(x,y)\,\mathrm{d}x\,\mathrm{d}y}{\iint \mathscr{E}_{SH}{}^2(x,y)\,\mathrm{d}x\,\mathrm{d}y}, \\ \kappa_f &= \frac{2d_{33}\omega_f}{\pi c n_f} \cdot \frac{\iint \mathscr{E}_f{}^2(x,y)\mathscr{E}_{SH}(x,y)\,\mathrm{d}x\,\mathrm{d}y}{\iint \mathscr{E}_f{}^2(x,y)\,\mathrm{d}x\,\mathrm{d}y}. \end{aligned} \tag{2.28}$$

With the QPM structure of the period Λ and a m-th order process implemented, the phase mismatch $\Delta\beta_{SHG}$ is

$$\Delta\beta_{SHG} = \beta_{SH} - 2\beta_f + m\frac{2\pi}{\Lambda}. \tag{2.29}$$

Solution

In the limit of an undepleted pump, an analytic solution can be derived. The amplitudes of the fundamental wave and generated SH wave after a propagation length of L are

$$\begin{aligned} A_f(L) &= e^{-\frac{\alpha_f}{2}z}A_{f,0}, \\ A_{SH}(L) &= -i\kappa_{SH}A_{f,0}^2\frac{e^{\left(i\Delta\beta_{SHG}+\frac{\alpha_{SH}}{2}-\alpha_f\right)L}-1}{i\Delta\beta_{SHG}+\frac{\alpha_{SH}}{2}-\alpha_f}e^{-\frac{\alpha_{SH}}{2}L}. \end{aligned} \tag{2.30}$$

The power of the fundamental wave and the SH wave can be calculated from the amplitudes above using the definition in (2.15); the conversion efficiency in a general case is then obtained as

$$\eta_{SHG} = \frac{P_{SH,L}}{P_{f,0}} = \frac{8d_{33}^2}{\varepsilon_0 c n_{SH} n_f^2 \lambda_{SH}^2 S_{eff}} g(L) P_{f,0}, \tag{2.31}$$

where

$$S_{eff} = \frac{\left(\iint \mathscr{E}_f{}^2(x,y)\,\mathrm{d}x\,\mathrm{d}y\right)^2 \iint \mathscr{E}_{SH}{}^2(x,y)\,\mathrm{d}x\,\mathrm{d}y}{\left(\iint \mathscr{E}_f{}^2(x,y)\mathscr{E}_{SH}(x,)\,\mathrm{d}x\,\mathrm{d}y\right)^2}, \tag{2.32}$$

$$g(L) = e^{-2\alpha_f L}\frac{\left(e^{\Delta\alpha L}+1\right)^2 - 4cos^2\left(\frac{\Delta\beta_{SHG}L}{2}\right)e^{\Delta\alpha L}}{\Delta\alpha^2 + (\Delta\beta_{SHG})^2}, \tag{2.33}$$

$$\Delta\alpha = \alpha_f - \frac{\alpha_{SH}}{2}.$$

Assuming a lossless waveguide, the efficiency in (2.31) can be written as

$$\eta_{SHG} = \underbrace{\frac{8d_{33}^2}{\varepsilon_0 c n_{SH} n_f^2 \lambda_{SH}^2 S_{eff}}}_{\eta_{SHG,norm}} sinc^2(\frac{\Delta\beta L}{2}) L^2 P_{f,0}. \tag{2.34}$$

For SHG with exact phase matching, the conversion efficiency increases with the coupled funmdamental power $P_{f,0}$ and propagation length L. Equation (2.34) provides guidelines of designing a QPM waveguide such that a high efficiency can be achieved i.e. by using a long waveguide with small cross section. A normalized SH efficiency of a conventional channel waveguide with an effective cross section of 57 μm^2 can be up to $\sim$53 $\%W^{-1}cm^{-2}$ in a lossless case. It should be noted such an efficiency can be achieved only with exact phase matching in a lossless waveguide and low fundamental power. The propagation loss and phase mismatch tend to not only reduce the efficiency but also broaden the bandwidth. With high fundamental power, the energy transfered from the fundamental wave into the SH wave can not be neglected. As a consequence, the generated SH power will increase linearly instead of parabolically with respect to the fundamental power. What is more, the onset of the photorefractive effect at a high fundamental power level also deteriorates the conversion efficiency.

2.4 Cascaded nonlinear interaction (SHG/DFG)

Besides the direct $\chi^{(2)}$ process discussed above, a cascaded $\chi^{(2)} : \chi^{(2)}$ process is often of special interest, when the interacting waves are not in the same frequency band [38]. This is because an optical waveguide, which transmits only the fundamental mode at a long waveguide (i.e. 1550 nm), can transmit multiple modes at a short waveguide (i.e. 775 nm). The propagation constant of different transverse mode is different. However, the QPM condition is only fulfilled for a specific transverse mode (typically fundamental mode) of each wave. Therefore, selectively exciting only the required transverse mode of each interacting wave is essential for an efficient interaction. In a cascaded $\chi^{(2)} : \chi^{(2)}$ process such as a cascaded SHG/DFG, both pump (also fundamental wave in this

case) and signal waves are within the same band. The interaction involves the cascading of SHG and DFG as shown in figure 2.4. The fundamental wave at ω_f is converted to frequency ω_{SH} by SHG. Simultaneously, the generated ω_{SH} serves as pump wave, and is mixed with the input signal ω_s to generate a wavelength-shifted idler ω_i ($\omega_i = \omega_{SH} - \omega_s = 2\omega_f - \omega_s$) by DFG.

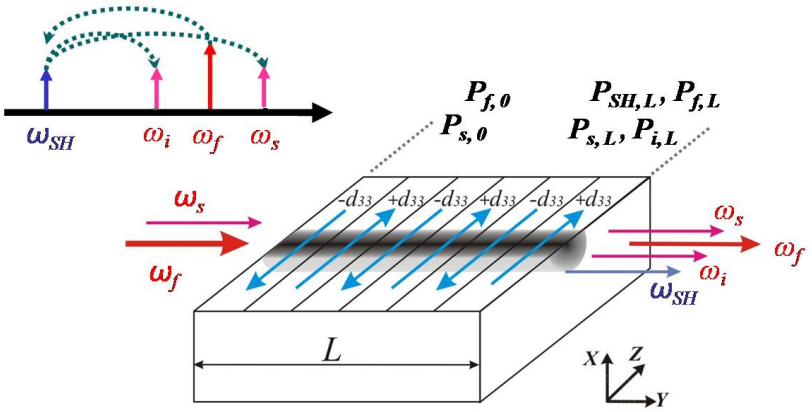

Figure 2.4: Schematic sketch of cascaded SHG/DFG in a waveguide on a X-cut $LiNbO_3$ substrate. Inset: sketch of frequency mixing.

Since in such a cascaded scheme all the input waves are within the same band ($\omega_f \approx \omega_s \approx \omega_i \;\; \omega_{SH} = 2\omega_f$) in this frequency-mixing process, coupling coefficients can be simplified such as $\kappa_f \approx \kappa_s \approx \kappa_i \equiv \kappa$ and $\kappa_{SH} = 2\kappa_f$. The coupled-mode equations can then be expressed in a simplified manner as

$$\begin{aligned}
\frac{\partial A_f}{\partial z} &= -\frac{\alpha_f}{2}A_f - i\kappa A_{SH}{A_f}^* e^{-i\Delta\beta_{SHG}z}, \\
\frac{\partial A_{SH}}{\partial z} &= -\frac{\alpha_{SH}}{2}A_{SH} - i\kappa {A_f}^2 e^{i\Delta\beta_{SHG}z} - i2\kappa A_s A_i e^{i\Delta\beta_{DFG}z}, \\
\frac{\partial A_s}{\partial z} &= -\frac{\alpha_s}{2}A_s - i\kappa {A_i}^* A_{SH} e^{-i\Delta\beta_{DFG}z}, \\
\frac{\partial A_i}{\partial z} &= -\frac{\alpha_i}{2}A_i - i\kappa {A_s}^* A_{SH} e^{-i\Delta\beta_{DFG}z},
\end{aligned} \tag{2.35}$$

$$\begin{aligned}
\Delta\beta_{SHG} &= \beta_{SH} - 2\beta_f, \\
\Delta\beta_{DFG} &= \beta_{SH} - \beta_s - \beta_i.
\end{aligned} \tag{2.36}$$

For such an interaction, significant pump depletion is required to convert the fundamental wave to its SH wave, which serves as the pump for DFG. Equations (2.35) also ignore the possible interaction between the fundamental wave and the signal wave via SFG, which will happen only when the input signal frequency is tuned too close to the fundamental frequency. It has been discussed before that such coupled-mode equations generally can only be solved using numerical methods. In order to get some insight into the conversion process, we derive a simplified analytic solution by assuming that pump depletion, propagation loss and group velocity mismatch can be ignored. Therefore, the

first two equations in (2.35) would be equivalent to (2.27). We also assume a constant signal intensity P_s. Under the phase matching condition ($\Delta\beta_{_{SHG}} = 0$ and $\Delta\beta_{_{DFG}} = 0$), we substitute the solution for SHG in (2.30) into the last equation of (2.35); under the low gain limit, we obtain the power of the idler wave P_i and the conversion efficiency from signal to idler in the following form

$$P_i \approx \frac{1}{4} \underbrace{\frac{8d_{33}^2}{\varepsilon_0 c n_{_{SH}} n_f^2 \lambda_{_{SH}}^2 S_{_{SHG,eff}}}}_{\eta_{SHG,norm}} \underbrace{\frac{32d_{33}^2}{\varepsilon_0 c n_i n_s n_f \lambda_i \lambda_s S_{_{DFG,eff}}}}_{\eta_{DFG,norm}} L^4 P_{f,0}^2 P_{s,0}. \tag{2.37}$$

$$\eta = \frac{P_i}{P_{s,0}} \approx \frac{1}{4} \eta_{SHG,norm} \eta_{DFG,norm} L^4 P_{f,0}^2. \tag{2.38}$$

The normalized conversion efficiency increases with the length of the device quadruple exponentially; thus a long device is advantageous to achieve a high conversion efficiency. However, in a practical device, due to pump depletion and waveguide propagation losses, the dependence on the device length is less than the fourth power.

2.5 Nonlinear interactions in ridge-type waveguides

As shown in (2.22), (2.31)and (2.38), the nonlinear conversion efficiency in a second order nonlinear interaction has a strong dependence on the device geometry, i.e. interaction length L and effective cross section S_{eff}. The interaction length one can achieve is generally limited by the fabrication techniques with the considerations of the propagation loss and quality of the periodic poling. The effective cross section is determined mainly by the material and the geometric dimension of the waveguide, which can vary significantly for different types of waveguide. The essential part of designing a highly efficient $LiNbO_3$ waveguide is to minimze S_{eff}. Therefore, a ridge waveguide is of increasing interest since it can improve the light confinement. The calculation in this section shows that it also improves the overlap between the transverse modes of the interacting waves, i.e. reduce S_{eff}. In this work, we simulate the optical fields in waveguides using a finite difference module provided by the commercial software OlympIOs. One of the nonlinear interactions of interest in this work is SHG at a fundamental wavelength of ∼1550 nm utilizing the nonlinear coefficient d_{33}. The discussion in the section will be focused in this interaction as an example. The analysis and conclusions also apply to other interactions such as DFG and cascaded SHG/DFG. Two types of ridge waveguides, Ti in-diffused ridge guide and LNOI photonic wire, are discussed.

The simulation of the optical modes in a Ti in-diffused ridge waveguide using the finite difference method has been discussed in [39] in detail, and will not be repeated in this thesis. The distribution of the refractive index through a Ti in-diffusion is calculated from the distribution of Ti^{4+} ions taking the material dispersion into account. The Ti^{4+} ion concentration is determined by the thickness of the Ti layer and the diffusion parameters i.e. temperature and duration. In this work, in-diffusion of Ti with the

thickness of 70, 80 and 90 nm respectively, is carried out at 1060 °C for 8.5 hours in O_2 environment. O_2 is required to reduce the out-diffusion of Li^+ ions at high temperature. In comparison, the simulation for a LNOI photonic wire is much more straightforward as the refractive index is homogeneously distributed in the material as growth.

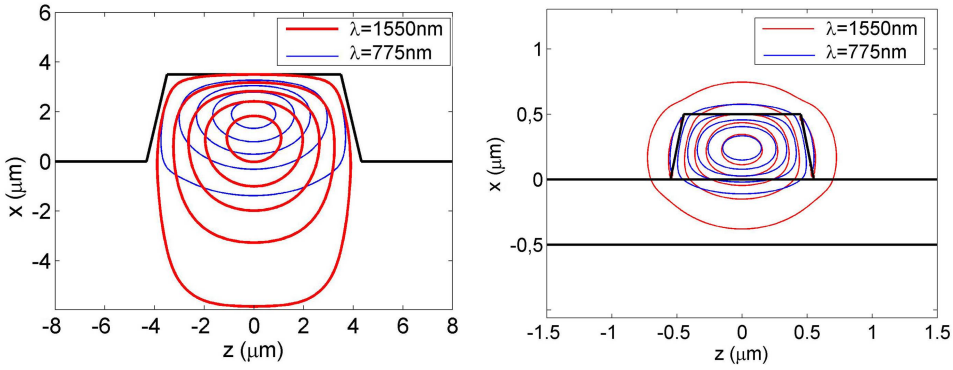

(a) (b)

Figure 2.5: Simulated optical intensity profiles for TE modes at 1550 nm (red curves) and 775 nm (blue curves) in (a) a ridge waveguide fabricated on X-cut Y-propagating $LiNbO_3$ with the top width of 7 μm and the height of 3.5 μm and (b) a X-cut photonic wire with the width of 1 μm and the height of 0.5 μm. The lines represent 10, 30, 50, 70 and 90 % of the peak intensity for both modes.

Figure 2.5 shows the simulated optical modes of both fundamental and SH waves in a ridge guide and a LNOI photonic wire. This ridge guide in figure 2.5(a) has a top width of 7 μm and a height of 3.5 μm; the thickness of the Ti stripe was 80 nm. The LNOI photonic wire in figure 2.5(b) has a width of 1 μm and a height of 0.5 μm. The improvement of the light confinement becomes evident by comparing the mode sizes of ridge-type waveguides with that of a conventional Ti in-diffused channel waveguide of 7 μm width in table 2.1. Let us first compare a Ti in-diffused ridge guide and a conventional waveguide. The optical mode of a Ti in-diffused ridge guide is reduced by one third in the horizontal direction compared to a conventional one, mainly due to the high refractive index contrast between the ridge body and the air. However, the mode size in the vertical direction does not differ much since the refractive index change induced by the Ti in-diffusion has a similar profile. In contrast to the Ti in-diffused ridge guide, which yields an improvement of light confinement mainly in the horizontal direction, a LNOI photonic wire presents an improvement of the mode size by a factor of 10 in both horizontal and vertical directions. This is due to the high index contrast with an almost symmetric geometry in all four interfaces. It is especially important to note that figure 2.5(b) shows a good coincidence of the centers of two optical modes, resulting in a nearly perfect mode overlap. Compared to a conventional waveguide, the effective cross section S_{eff} is reduced by one third using a Ti in-diffused ridge guide and nearly a factor of 100 using a LNOI photonic wire; accordingly the nonlinear efficiency could increase by a factor of 1.5 and 100, respectively, without taking the propagation losses into account.

	C. Ti in-diffused waveguide	Ti in-diffused ridge guide	LNOI Photonic wire
$X[\mu m]$	5.28	3.86	0.56
$Y[\mu m]$	3.54	3.36	0.4
$S_{eff}[\mu m^2]$	57	38.5	0.21

Table 2.1: Mode size in horizontal and vertical directions and effective cross section of a conventional Ti in-diffused channel waveguide, a Ti-diffused ridge guide and a LNOI photonic wire. The orientation and geometric design of the waveguides are described in the text above.

An additional improvement of the nonlinear efficiency is possible by using a ridge guide of different parameters i.e. waveguide dimensions and Ti thickness as shown in figure 2.6. When the Ti layer is thicker, the Ti^{4+} concentration inside the ridge is higher, and the increase of the refractive index is larger; therefore, both fundamental and SH modes are better confined closer to the upper surface than the ridge guides with lower Ti layer, resulting in a better overlap. Figure 2.6 also shows that a narrower ridge gives a better mode overlap. S_{eff} can be enhanced by a factor of 2 in a Ti in-diffused ridge guide with the optimal design.

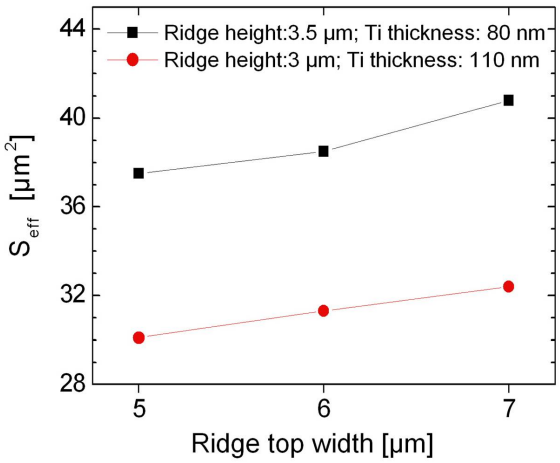

Figure 2.6: Comparison of S_{eff} of ridge guides with different parameters.

In practice, due to a relatively higher propagation loss in a ridge guide (i.e. ~1 dB/cm) compared to a conventional Ti in-diffused channel waveguide (i.e. ~0.1 dB/cm), the increase of the SH efficiency would be compromised to a certain degree. Figure 2.7 gives an example of the normalized SHG conversion efficiency deteriorating with the increase of the propagation loss for different interaction length, assuming fundamental wave and SH wave have the same propagation loss. However, the propagation losses could be reduced by improving the fabrication processes (see discussions in chapter 3 and 4). Therefore, a highly efficient nonlinear interaction in a low-loss ridge guide is achievable.

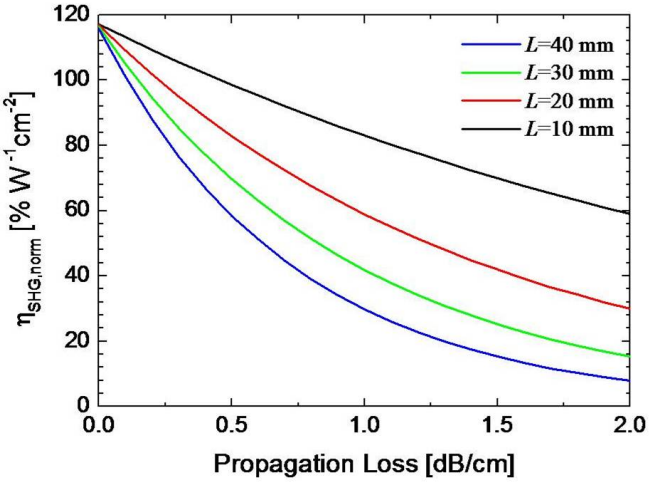

Figure 2.7: Normalized SH efficiency varies as a function of propagation loss and interaction length for a ridge guide with $S_{eff} = 38.5\ \mu m^2$, given $\alpha_f = \alpha_{SH}$.

Another advantage of using ridge guides is the potential of realizing wavelength conversion, where the input of one or more high intensity optical fields is required. As briefly mentioned before that in a congruently melt $LiNbO_3$ waveguide the photorefractive effect is prominent at high intensity level, and therefore deteriorates the conversion efficiency. Common methods of suppressing photorefractive effect are operating the system at a high temperature, generally $> 150\,°C$ or using MgO or ZnO doped $LiNbO_3$ instead. It requires either a complicated temperature control system or expensive material, i.e. increases fabrication complexity and cost. It was first observed by Nishida et.al. that a ridge waveguide on Z-cut $LiNbO_3$ shows high damage resistance at room temperature [40]. A similar phenomenon is observed in ridge guides on a X-cut $LiNbO_3$ substrate in this work. This interesting phenomenon could be due to that the electrons generated via photorefraction can move to the surface of the ridge, then be compensated from the ambient environment due to the unique geometry of the ridge. In this way, no sustained electric field generated by the photorefraction exists in the waveguide to induce the change of the refractive index. This property could be of strong interest for industrial applications.

Last but not least, a ridge-type waveguide, especially a photonic wire, has the potential in realizing counterpropagating nonlinear interaction. As discussed in section 2.2, the domain period required for a counter-propagating nonlinear interaction such as backward SHG is often in the submicron range. PPLN of such a period is difficult to be realized in a $LiNbO_3$ bulk crystal due to the difficulty of fabricating submicron electrodes and degradation of electric field contrast. With a ridge and a LNOI thin film, because the periodically poled volume is 2 - 3 orders of magnitude smaller than that of a bulk crystal, fabricating submicron periodical electrode is feasible. Several methods of fabricating submicron domains are studied in this work; results will be discussed in the corresponding section.

2.6 Summary

In this chapter, we have developed coupled-mode equations for guided-wave $\chi^{(2)}$ nonlinear interactions such as DFG, SHG and a cascaded SHG/DFG, and demonstrated theoretically that QPM is an effective phase matching technique in guided-wave nonlinear interactions.

Simplified solutions of all the coupled mode equations are solved to illustrate the dependence on several important parameters assuming no loss and no pump depletion. In SHG, we see that the conversion efficiency is typically proportional to the square of the fundamental power in SHG; in DFG, it is proportional to the product of the pump power and the signal power. In both cases, the conversion efficiency is proportional to the square of the interaction length, and inversely proportional to the nonlinear cross section.

The potential improvement of the nonlinear conversion efficiency using ridge guides and photonic wires due to a reduced nonlinear cross section has been discussed. The photonic wire is a favorable choice of waveguide since it can enhance the conversion efficiency by a factor of 100.

Chapter 3

Fabrication of PPLN ridge waveguides

This chapter presents the details of fabricating PPLN ridge waveguides on a X(Y)-cut $LiNbO_3$ substrate. In the first section, the fabrication of ridge waveguides on a X(Y)-cut $LiNbO_3$ substrate using plasma etching is introduced. This fabrication method was originally developed by Hu [41]. In the second section, local periodic poling of ridge waveguides is presented. The fabrication processes are illustrated using a X-cut $LiNbO_3$ substrate as an example. The actual processes are identical for X-cut and Y-cut $LiNbO_3$ substrates.

3.1 Ridge fabrication and Ti in-diffusion

Ridge waveguides on a X-cut $LiNbO_3$ are fabricated using inductively coupled plasma (ICP) etching and subsequent Ti in-diffusion. The substrate used in this work is a 1 mm thick X-cut congruent $LiNbO_3$ substrate from CrystalTech Inc. The essential processes are depicted in figure 3.1. The details of each step are illustrated in the following:

Step 1: Substrate preparation

The fabrication starts with a proper cleaning of the substrate surface. The cleanliness of the surface is essential for a good adhesion between the substrate surface and the metal layer which will be coated in the next step. Therefore, we use a three-steps cleaning process:

- Cleaning in H_2SO_4:H_2O_2 (9:1), also called "piranha", at 50 °C for 10 minutes. This cleaning solution can remove organic pollution on the sample.
- Cleaning in deionized water with soap at 50 °C for 10 minutes to eliminate remaining leftovers from the last step.
- Cleaning in H_2O:H_2O_2:NH_4OH (7:2:1), also known as RCA Standard Cleaning 1 (RCA SC-1), at 50 °C for 30 minutes. RCA SC-1 is useful to remove particles and organic residues on the surface.

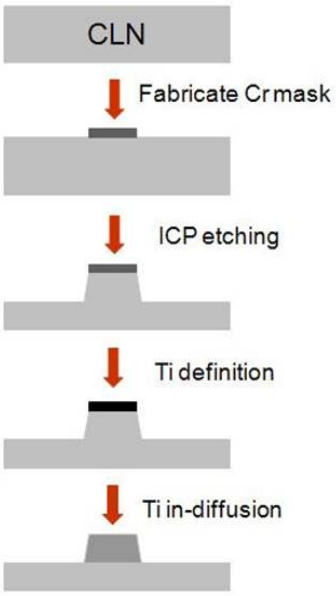

Figure 3.1: A flow chart of ridge waveguides fabrication.

Step 2: Fabrication of the Cr mask

The substrate is blow dried with nitrogen after cleaning, and then immediately put into the sputtering chamber. A 300 - 400 nm thick Cr layer is then sputtered on the substrate surface. The thickness of the Cr layer is designed depending on the height of the ridge and the etching rates of Cr and $LiNbO_3$ during ICP etching. With the ICP etching in a mixture of 15 sccm C_4F_8 and 15 sccm Helium, the ratio of the etching rate between $LiNbO_3$ and Cr is greater than 10:1. Once the Cr layer is deposited, a standard lithography process is made in order to transfer the waveguide structure from the e-beam written photomask to the sample. This is accomplished by using the positive photoresist Fujifilm OIR907-17, spun at 6000 rpm during 3 seconds, soft baked at 90 °C for one hour and exposed with a UV lamp in a mask aligner. Then the photoresist is hard baked at 130 °C for one hour and developed in OPD4290 developer. Afterwards, the remaining photoresist is used as a mask in a wet etching process of the Cr layer in a solution of 100ml H_2O, 5ml H_2SO_4 and 40 g Cerium (IV) sulfate. After the etching, a 10% H_2SO_4 solution is used to remove etching residues that remain on the surface of the substrate. Now the $LiNbO_3$ substrate is covered with Cr stripes of the width 8 - 10 μm, and is ready for ICP etching.

Step 3: ICP etching

Plasma etching is a very efficient, well controllable process well known from semiconductor technology. It is performed in a Plasma100 system (Oxford Instrument). Plasmas based on fluorine gases are generally used for etching $LiNbO_3$ due to the volatility of fluorinated niobate species at a temperature around 200 °C. The etching gas we use in this work is a mixture of 15 sccm C_4 F_8 and 15 sccm He. During

etching one of the etching products, LiF, is re-deposited on the surface of the sample. In the meantime carbon polymers as byproducts accumulate on the substrate surface. Both effects lower the etching rate. Therefore, we use a repeating process consisting of multiple runs. After each run of etching (empirically 3 - 4 mins), the sample needs to be taken out and cleaned in RCA SC-1 solution for 1 minute to remove the carbon polymers which appear as a brown layer on the substrate. One run of etching generally induces a depth of 300 - 400 nm. The ridge waveguides presented in this thesis as examples have a height of 3.5 μm. It requires generally 9 - 10 runs to reach such a depth. After the ICP etching is completed, the remaining Cr stripes have to be removed by a Cerium Sulfate solution and the sample is carefully cleaned. Figure 3.2 shows an etched ridge on a X-cut $LiNbO_3$ substrate. We use the term "undoped ridge" to refer to this ridge in order to distinguish it from a Ti in-diffused ridge. The surface of the substrate appears fairly rough due to the etching process. The width of the ridge top is generally $\sim$1 μm narrower than on the photomask due to the under-etching effect.

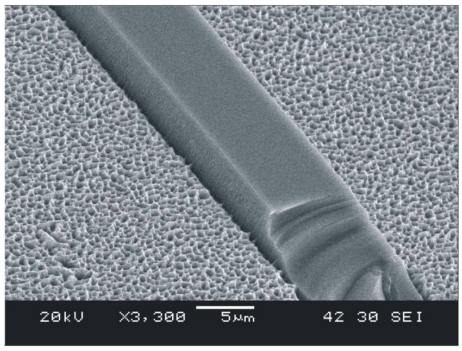

Figure 3.2: A SEM micrograph of an etched ridge.

Step 4: Ti deposition

With the ridge structure, the light confinement in the lateral direction is automatically achieved by the high refractive index contrast between $LiNbO_3$ and air. However, in the vertical direction, one has to increase the refractive index inside the ridge artificially. This could be done by either Ti in-diffusion or proton exchange. In this research, Ti in-diffusion is investigated. It is possible to take advantage of the unique geometric profile of a ridge structure to accurately create Ti stripes only on top of the ridges without an additional e-beam written photomask and lithographic steps. A flood exposure and lift-off technique is implemented as shown in figure 3.3.

This technique starts with spin-coating of a thin photoresist layer, for example, the OIR907-17, on the sample. Due to the embossed surface of the ridge top, the thickness of the photoresist on top of the ridge will be thinner than on the surrounding. Therefore, it is possible to make a short UV light illumination, i.e. insufficient exposure dose, which is only able to completely expose the upper layer

of the photoresist with the thickness on top of the ridges. Correspondingly, a short developing is followed to remove the exposed photoresist from the top of the ridges while leaving the rest of the photoresist on the substrate. A thin layer (70 - 80 nm) of Ti is then deposited homogeneously on the sample. The lift-off of Ti is done by soaking the sample into acetone till the photoresist and the metal on top of the photoresist cleared away. Ultrasonic bath is usually applied to speed up this process and get a better cleaned surface.

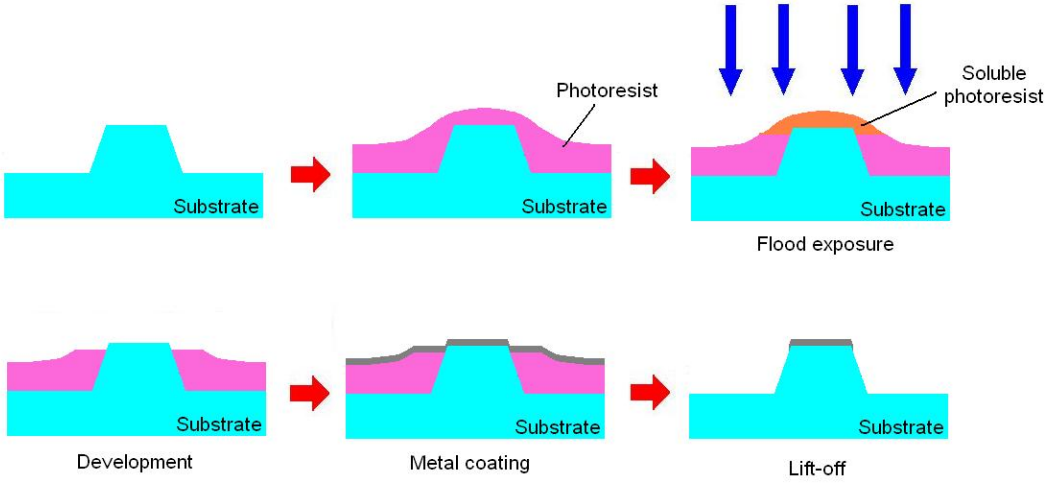

Figure 3.3: Scheme of the flood exposure technique used to deposit Ti only on top of the ridge.

Step 5: Ti in-diffusion

After the Ti stripe is properly fabricated on top of the ridge, the sample is sent to the diffusion oven where the diffusion procedure is applied:

- Heating up to 1060 °C during 1.5 hours in O_2 atmosphere.
- Diffusion during 7.5 hours in Ar atmosphere.
- Second diffusion during 1 hour in O_2 atmosphere. The second diffusion in O_2 is used to restore the oxygen into the $LiNbO_3$ structure that was out-diffused before.
- Cooling down to room temperature.

A Ti in-diffused $LiNbO_3$ ridge waveguide, also called a "doped ridge" in this thesis, is shown in figure 3.4. Compared to figure 3.2, the surface of the substrate is significantly smoothed due the diffusion at the high temperature, so is the side wall of the ridge. In this way, the propagation loss of the ridge waveguide due to scattering by the rough side walls will be reduced.

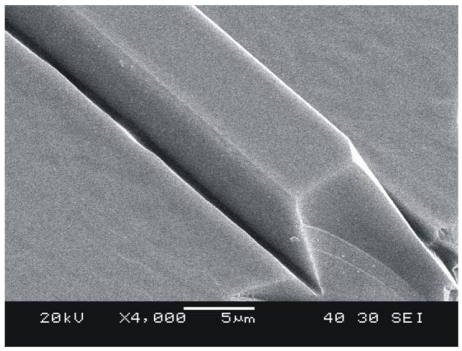

Figure 3.4: A SEM micrograph of a Ti in-diffused ridge waveguide.

3.2 Local periodic poling

Considering that the spontaneous polarization of a X-cut $LiNbO_3$ substrate is parallel to the surface, within a ridge geometry, this direction happens to be approximately perpendicular to the side walls of the ridges. The idea of the local periodic poling is to place the metal electrodes on both sides of the ridge, then apply an electric field between them, as depicted in figure 3.5. The distance between two side walls (<10 μm) is two orders of magnitude smaller compared to the thickness of a conventional Z-cut $LiNbO_3$ substrate (typically 0.5 mm), meaning that a roughly two orders of magnitude lower voltage is needed to overcome the coercive field E_c compared to that of poling a bulk $LiNbO_3$ crystal. The domain inversion presumably happens only in the body of the ridge as the electric field in the outer region is significantly lower.

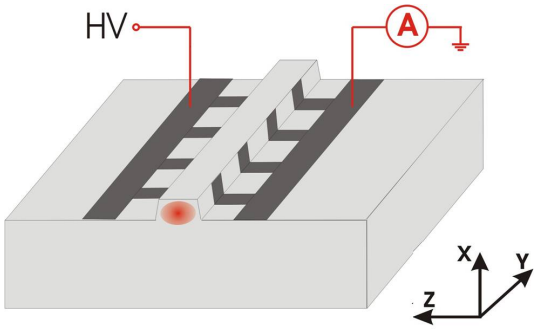

Figure 3.5: Scheme of the poling configuration for a ridge on X-cut LN.

The static electric field distribution is calculated in the cross section of the ridge using a finite difference method. Homogeneous electrodes are assumed for the calculations. A numeric derivation was made on a non-uniform grid of 512×512 points in an area of 60×50 μm^2 around the ridge, yielding as result the profile of the relevant component E_z of the electric field distribution [39]. Figure 3.6 simulated by Miguel Garcia Granda presents, as an example, the calculated electric field distribution in an undoped ridge with the height 4 μm and top width 9 μm, assuming 1 V applied to the left electrode and the right electrode grounded. As the coercive field of LN is ∼21 kV/mm, the applied

voltage should be at least 166 V to allow domain inversion to take place. First nucleation is expected at the upper edge of the ridge where the field is highest. In most of the cases, due to the imperfection of the electrodes, the actual applied voltage had to be higher than the simulated value.

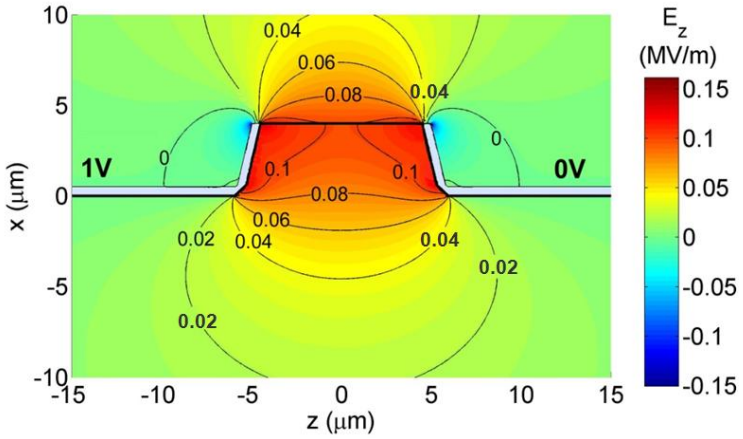

Figure 3.6: Calculated E_z (MV/m) in a ridge of 4 μm height and 9 μm width, assuming 1 V applied to the left electrode with the right electrode grounded.

Standard lift-off lithography is used to fabricate comb-like electrodes as depicted in 3.5. An image reversal photoresist with a relatively high viscosity is required for successful lift-off on the non-planar substrate. We use a thick photoresist AZ4533 (MicroChemicals) mixed with 1.2% imidazol as the image reversal photoresist. Spincoating the photoresist at 3000 rpm for 10 seconds results in a $\sim$4 μm thick photoresist layer on the planar substrate, sufficient to cover the top of the ridge. An E-beam written photomask is designed containing many groups of comb-like finger structures with period of 16.2 μm and 16.6 μm and different duty cycle ranging between 25 : 75 and 50 : 50 (finger width : interval width). The consideration of using different duty cycles comes from our experience of periodic poling of Z-cut $LiNbO_3$, where the domain inversion not only proceeds along the direction of the electric field but also grows laterally toward the neighbouring domain. After the photoresist is exposed and developed, a reversed electrode structure is transferred to the photoresist layer. A 100 nm thick Ti or Cr layer is then deposited homogenously on the substrate. The metal coated sample is soaked in acetone for some time in order to remove the photoresist and the metal on top of the photoresist. Figure 3.7 shows the top view of a fabricated electrode structure under an optical microscopy.

It is also possible to fabricate comb-like electrodes with fine periods. One approach is fabricating a fine periodical grating using the holographic lithography discussed in Appendix A. The fabrication consists of three major steps in the following.

Step 1: A thin layer of photoresist AZ4533 is spincoated over the surface. During the exposure, the photoresist on top of the ridge is protected by the photomask from being exposed. After the development, only a thin layer of photoresist on top of

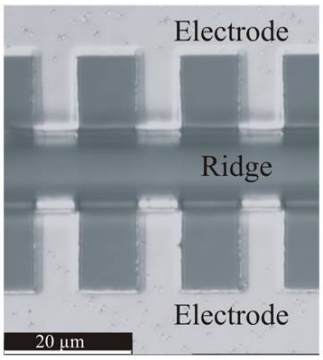

Figure 3.7: Top view of the electrodes of 16.6 μm period for a 9 μm wide ridge.

the ridge remains. This part of photoresist is used to avoid the direct connection between counter electrodes.

Step 2: A thin layer of photoresist SX AR-P 3500/6 is spincoated over the surface. The coated sample is then exposed using Lloyd's interferometric optical holography (see Appendix A) for 15 seconds and developed. Afterwards, a 100 nm thick Ti is evaporated over the surface. The undeveloped photoresist from the last two steps and Ti on top of it is removed in aceton bath.

Step 3: Standard lift-off lithography is performed in order to connect all the Ti strips in the same grating group, therefore, comb-like electrodes can be formed. A photomask with stripe structures parallel to the waveguide is used during the exposure. After Ti evaporation and subsequent lift-off, counterparts of comb-like electrodes are formed.

Fabricated comb-like electrodes of a period of 2 μm are shown in figure 3.8. Due to the unique topography of a ridge structure, the Ti finger tips are narrower towards to the ridge side walls. This approach is rather complicated and challenging as the quality of the resulting electrodes is highly influenced by the precision of lithography in each step. An advanced alternative could be using E-beam lithography to write photoresist gratings with fine periods. However, it is often time and cost consuming and not accessible in this work.

The poling experiments were done in an oil bath to maintain a high resistance between the two electrodes and to avoid surface currents as much as possible. Voltage pulses with different pulse durations and different numbers of pulses are applied from a computer controlled voltage amplifier for poling, and in the meantime the voltage across the ridge and the current from the ridge are monitored using a circuit shown in figure 3.9. A DC voltage amplifier controlled by a computer via D/A converter is used to provide a voltage in the range of 0 - 1000 V. 1% of the output voltage from the amplifier is output for monitory purpose. Voltages are detected by the computer via a A/D converter. Resistors $R1$, $R2$, $R3$ and $R4$ are carefully chosen to have enough sensitivity to measure the small signal while keeping $V1$ and $V2$ lower than the input

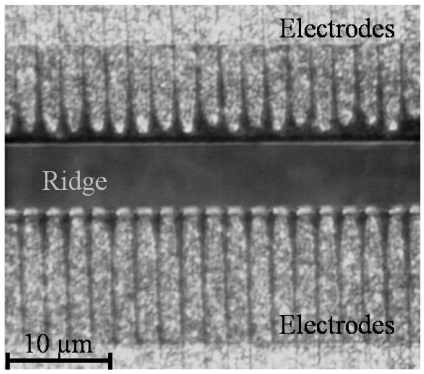

Figure 3.8: Top view of the electrodes of 2 μm period for a 8 μm wide ridge.

limit of the A/D converter. The actual voltage on the sample V_{LN} is calculated by $V_{LN} = \frac{R2+R3}{R3}V1 - V2$; the poling current I_{LN} is calculated by $I_{LN} = \frac{V2}{R4}$.

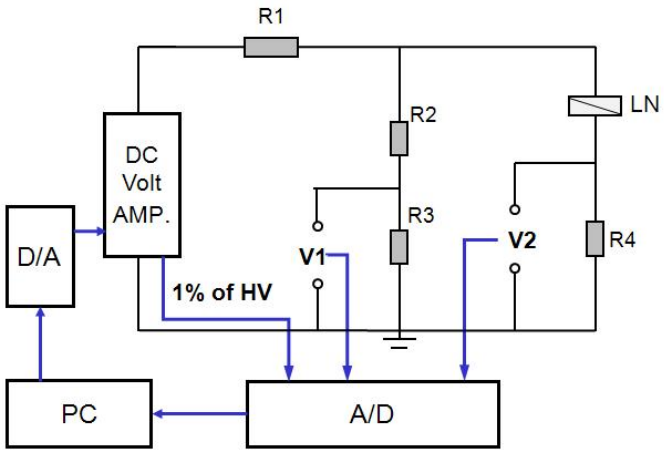

Figure 3.9: A sketch of the electric circuit for the local poling

Periodic poling in undoped and doped ridges has been investigated. Figure 3.10 presents the voltage/current-time characteristic for both an undoped ridge and a doped ridge of the same width and height during one single voltage pulse. The voltage is ramped up with a slope of 80 V/ms, kept constant for a certain time before ramped down to zero. For both undoped and doped ridge, the poling current abruptly rises when the voltage reaches a certain value, indicating the start of domain inversion.

In the undoped case (see figure 3.10(a)), the rise of the current starts at voltage of ∼180 V, which is consistent with the theoretical value calculated from electric field distribution. With the voltage continuing increasing, a second rising of the current appears when the voltage ramps up to ∼300 V, indicating domain inversion proceeding in a larger area. However, the current decrease when the voltage becomes stabilized is hard to explain. Afterwards, the current nearly stabilizes or decreases slightly with a constant voltage applied. Then it slowly drops to zero as the voltage ramps down. Considering the spontaneous polarization of congruent LN of 0.72 $\mu C/mm^2$ at room

temperature and the poled area of $\sim$0.1 mm^2 (four ridges were poled simultaneously), the total charge required for poling should be 0.14 μC. This value is significantly smaller than the measured total charge of $\sim$1 μC. We suspect that there might be some leakage current along the surface involved. However, the reason behind such a leakage current appearing only after domain inversion has taken place is not clear.

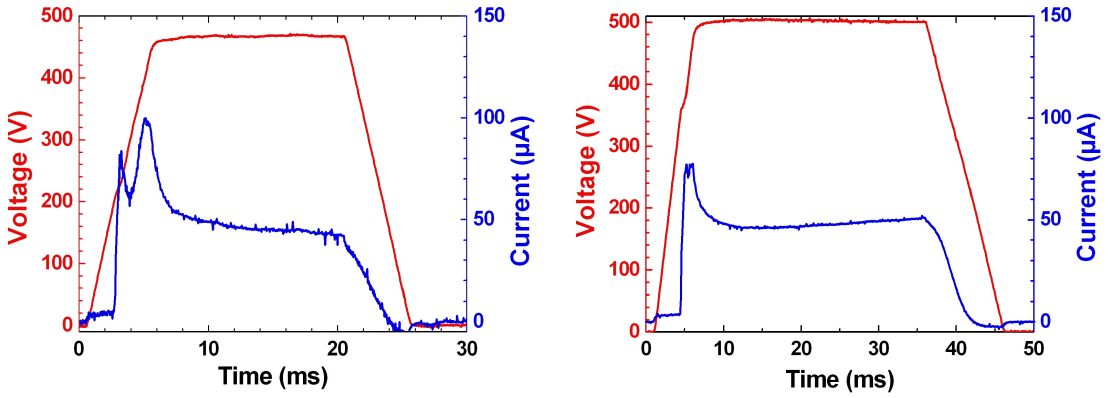

(a) (b)

Figure 3.10: Poling characteristics of (a) an undoped ridge and (b) a doped ridge of 8 μm width and 3.5 μm height.

In the case of poling a doped ridge waveguide (see figure 3.10(b)), domain inversion starts at a considerably higher voltage of $\sim$280 V. On one hand, this could be due to Li out-diffusion during annealing at the high diffusion temperature since the coercive field increases when the Li concentration decreases [42]. On the other hand, it has been observed in Ti in-diffused channel waveguide in Z-cut $LiNbO_3$ that the domain inverted area in Ti doped region is generally smaller than that in undoped region [43]. This phenomenon suggests that the coercive field of Ti doped $LiNbO_3$ could be slightly higher than that of undoped $LiNbO_3$. The higher electric field required for poling a Ti doped ridge guide could be the consequence of both effects.

When applying a chain of voltage pulses to the ridge, we observe that the largest charge is accumulated during the first pulse; it decreases fast with increasing pulse number as shown in figure 3.11. It might indicate that most of the domain inversion has been achieved by the first pulse alone. However there is still some remaining charge even in the very last pulse, which might be due to the leakage current. Such a behavior has already been observed previously [43]. The formation of a leakage current is not fully understood. One speculation is that the crystal lattices beneath the electrodes undergo a certain degree of damage due to the strong electric field applied, therefore, the leakage current can flow through the crystal. In most of our experiments, one or two pulses with 15 - 30 ms duration are used.

In principle, one can restore the polarization of the inverted domain by applying the electric field of the opposite polarity. For Z-cut $LiNbO_3$ crystal, the electric field required for restoring the inverted domain was found much lower than that required for

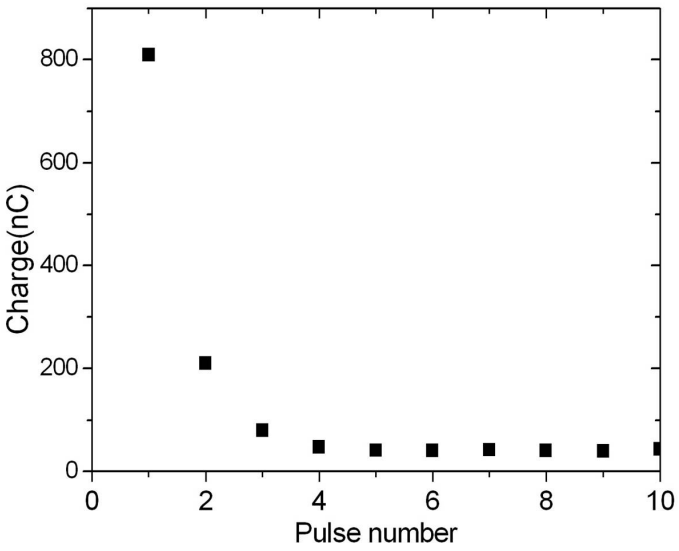

Figure 3.11: The accumulated charge per rectangular poling pulse of 270 V as function of the pulse number.

reversing an as-grow crystal [44]. Poling a ridge on a X-cut $LiNbO_3$ substrate using the electric field of a reversed polarity is tricky due to the existence of the leakage current. Figure 3.12 shows poling characteristics of periodically poling an undoped ridge on X-cut $LiNbO_3$ using a positive polarity electric field and subsequently a negative polarity electric field. Poling characteristics using a positive polarity electric field (red curve) is similar as we discussed in figure 3.10(a). When a negative polarity electric field (green curve) is applied, the current appears and increases along with the voltage. This near-ohmic behavior could be due to the leakage. When the voltage remains constant, the current stays at a lower value compared to the previous poling and decreases fast when the voltage decreases. One speculation is that, the area involved in the polarization restoration might be smaller than the poled area in the previous poling. This happens when the domain growth in the first poling is not complete, i.e. domain inversion starts from the +Z face has not completely reached the −Z face, resulting in a smaller poling area in the restoration poling than in the first poling.

The quality of the electrodes is important to the quality of the periodical domains. In practice, the imperfection from the fabrication, such as unsuitable duty cycle, asymmetric electrodes with respect to the central line of the ridge, and distorted finger tips, can lead to the incomplete domain growth. The voltage, duration and pulse number of the voltage pulses also play a role in domain growth in both longitudinal (direction from +Z face to −Z face) and lateral (along the ridge) directions. Moreover, a too strong electric field might cause damage of the crystal. A detailed discussion is given in the next chapter together with the characterization results of periodic domains.

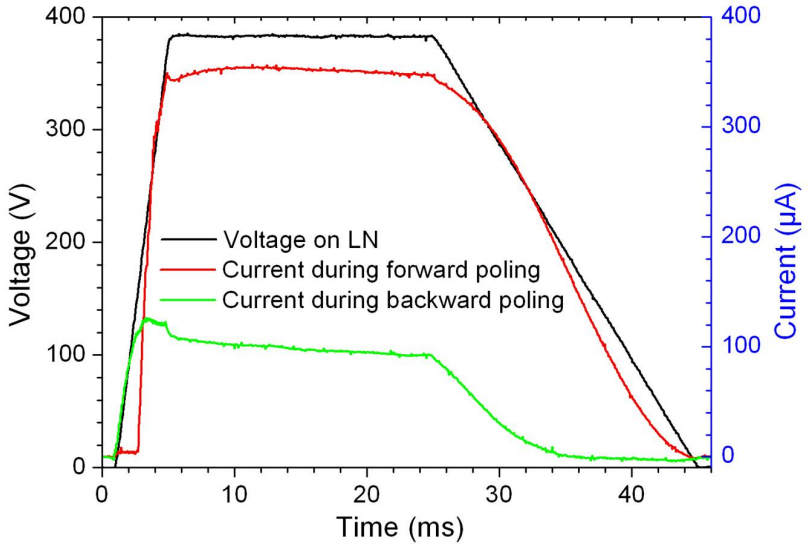

Figure 3.12: Poling characteristics of poling an undoped ridge on X-cut $LiNbO_3$ using a positive polarity electric field (red curve) and subsequently a negative polarity electric field (green curve). Voltage waveform is given in black curve.

3.3 Summary

In this chapter, the details of fabricating a periodically poled Ti in-diffused ridge guide on X(Y)-cut $LiNbO_3$ have been presented.

A ridge is fabricated using conventional lithography and ICP etching. Afterwards, a novel lift-off technique is used to define a Ti stripe only on top of the ridge. In-diffusion is performed in O_2 at 1060 °C for 8.5 hours.

After the ridge guide is fabricated, electric field assisted poling is performed to periodically reverse the spontaneous polarization of the crystal. This technique is called local periodical poling because domain inversion takes place in the body of the ridge only. In comparison to pole a bulk $LiNbO_3$ substrate, a very low voltage of a few hundred volts is sufficient for local periodical poling. However, a certain amount of leakage current has been observed after poling took place. The reasons of the leakage current and irreversible poling characteristics are not fully understood.

Chapter 4

Characterization of PPLN ridge waveguides

Different methods are applied to characterize ridge waveguides and periodically inverted ferroelectric domains inside the ridge waveguides. Section 1 presents the characterization of ridge waveguides by measuring the optical mode distribution, propagation loss and interaction cross section. Periodic ferroelectric domains are characerized using selective chemical etching and nonlinear confocal laser scanning microscopy(CLSM) respectively. The corresponding results are presented in section 2.

4.1 Waveguide properties

4.1.1 Propogation losses

The propagation losses are measured by analyzing the low-finesse Fabry-Perot resonances of a waveguide as shown in figure 4.1. The polished end faces of a waveguide form a low-finesse cavity. The cavity can be tuned by varying, either the wavelength of the propagating wave or the temperature of the sample. In this work, the temperature tuning is applied. The length of the sample increases with the increased temperature of the sample as a function of time. A coherent single-frequency laser beam at ∼1550 nm emitted from an external cavity laser (ECL) is launched into the waveguide and the output power is detected using an InGaAs photodiode. The time-dependent output current from the photodiode is recorded by a computer. The propagation losses are evaluated from the contrast of the resonances [45]:

$$\alpha = \frac{4.34}{L}(\ln R - \ln \tilde{R}), \quad \tilde{R} = \frac{1}{K}(1 - \sqrt{1 - K^2}) \;\; and \;\; K = \frac{I_{max} - I_{min}}{I_{max} + I_{min}}. \tag{4.1}$$

R is the reflectivity of the waveguide end faces; L is the cavity length in cm. K is the measured intensity contrast. α defines the upper limit of the propagation losses inside the cavity.

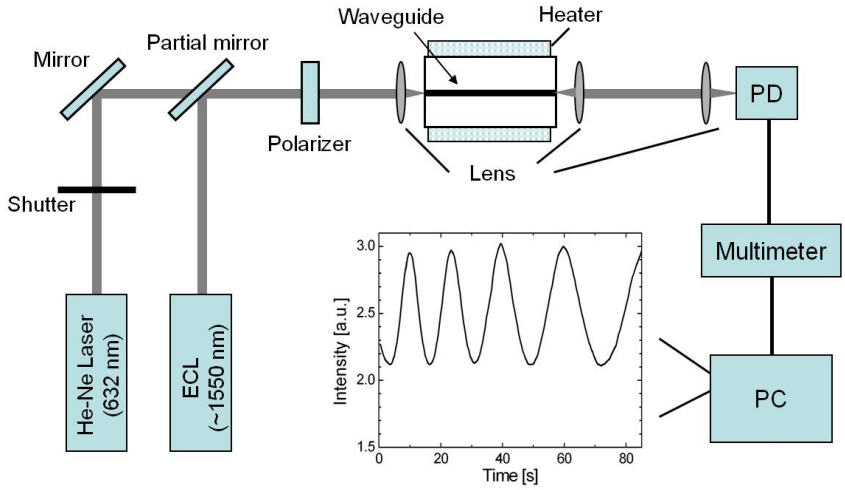

Figure 4.1: Schematic diagram of the loss measurement setup utilizing the low-finesse Fabry-Perot contrast method. PD: photodiode, ECL: external cavity laser.

The height and the top width of the ridge waveguides are mainly designed in such a way that the single mode transmission at a certain wavelength (1550 nm in this work) is guaranteed. For a Ti in-diffused ridge guide with a height of 3.5 μm and the original Ti layer of 70 - 80 nm thickness, due to the small refractive index contrast, the cut-off top width of the ridge guides for guiding the optical wave at 1550 nm is $\sim$ 4 μm. On the other hand, the ridge guides with a top width larger than 9 μm generally guide more than just the fundamental mode. Other factors such as propagation losses, nonlinear effective cross section and the feasibilty and reproducibility of the fabrication processes are also taken into account in the design. The propagation losses (mainly scattering losses) of the optical mode in a ridge guide of a smaller width is generally higher because the electric field is higher at the interface, and more scattering is induced. The relation between nonlinear effective cross section S_{eff} and the ridge top width as shown in figure 2.6 in section 2.5 indicates that a top width of 5 - 6 μm is prefered in order to minimize S_{eff}. With all these factors in mind, the ridge waveguides with a height of 3.5 μm and a top with of 6 - 8 μm are fabricated and investigated in this work. The lengths of the ridge guides are 13 - 27 mm.

Propagation loss of the optical mode in a ridge guide is mainly induced from the scattering of the electric field inside the ridge and at the interface. Plasma etching and other fabrication processes (lithography, wet etching of Cr, etc.) can bring in defects such as rough surface and pinholes. These defects will introduce large amount of scattering centers. Inhomogeneous Ti indiffusion also increases the loss because of the inhomogeneous refractive index distribution. Moreover, the crystal often undergoes a certain degree of damage during electric field assisted poling; scattering losses can be induced by such damage. The table 4.1 gives typical propagation losses at wavelength 1550 nm in TE and TM polarizations in ridge guides of different parameters.

For the ridge guides with top width within the range of 6 - 8 μm, as shown in table 4.1, there are several points worth noting. Firstly, the propagation loss of the optical mode

Ti thickness $[nm]$	70		80	
Top width $[\mu m]$	6.5	7.5	6	8
α_{TE} $[dB/cm]$	1.1	0.7	1.3	1
α_{TM} $[dB/cm]$	0.4	0.3	0.9	0.5

Table 4.1: Average propagation loss of Ti in-diffused ridge guides on X-cut $LiNbO_3$ at 1550 nm in both TE and TM polarization.

in a ridge guide on X-cut $LiNbO_3$ is generally higher than that of a ridge guide on Z-cut $LiNbO_3$ (0.2 - 0.5 dB/cm) fabricated by wet etching [13]. This is because the surfaces of ridges fabricated by plasma etching, especially the side walls, are rougher than those fabricated by wet etching. Secondly, the propagation loss increases with the decrease of the ridge top width (see the discussion above). Thirdly, ridge guides in-diffused with 70 nm thick Ti layer generally have lower losses than that with 80 nm thick Ti layer provided the in-diffusion process is identical and the geometric parameters of the ridge are comparable. This is because with thicker Ti, Ti^{4+} concentration is higher in the ridge and at the interface. This in turn introduces more scattering centers, therefore, higher loss. Last but not least, propagation loss of the ridge guide on X-cut $LiNbO_3$ in TE polarization is higher than that in TM polarization. This agrees with our experience in Ti in-diffused channel waveguide on Z-cut $LiNbO_3$. The optical mode with the electric field oscillating along the extraordinary axis (Z-axis) of $LiNbO_3$ usually undergos higher loss. The possible reason is that the optical mode, in which the electric field oscillates along Z-axis (TE mode in this work), generally has a smaller size (refer to section 4.1.2. The optical field confined inside the ridge is stronger, and the scattered optical field is in turn higher. This results in higher propagation loss.

4.1.2 Optical mode distribution

The transmission mode is measured using the experimental setup sketched in figure 4.2. The light path before the beam entering the waveguide is identical to that in figure 4.1 in section 4.1.1. An objective lens with high magnification (100X) is placed hehind the waveguide to magnify the near field distribution at the end face of the waveguide. This near field distribution is then imaged on an infrared camera. Figure 4.3 shows measured optical modes in both TE and TM polarizations from a Ti in-diffused ridge guide of a top width 7.5 μm and a height of 3.5 μm. A 70 nm thick Ti layer was diffused into this ridge guide. In both polarizations, a clear single mode is presented. The full width half maximum (FWHM) mode sizes are measured in the table 4.2 for ridge guides of different parameters. For a ridge waveguide on a X-cut $LiNbO_3$ substrate, the transmitted optical mode is smaller in TE polarization than in TM polarization. The horizontal mode size is mainly influenced by the top width of the ridge; it decreases with the decreased top width. The vertical mode size is, on the other hand, almost independent on the top width. The measured mode sizes agree with the calculated results presented in table 2.1 in section 2.5.

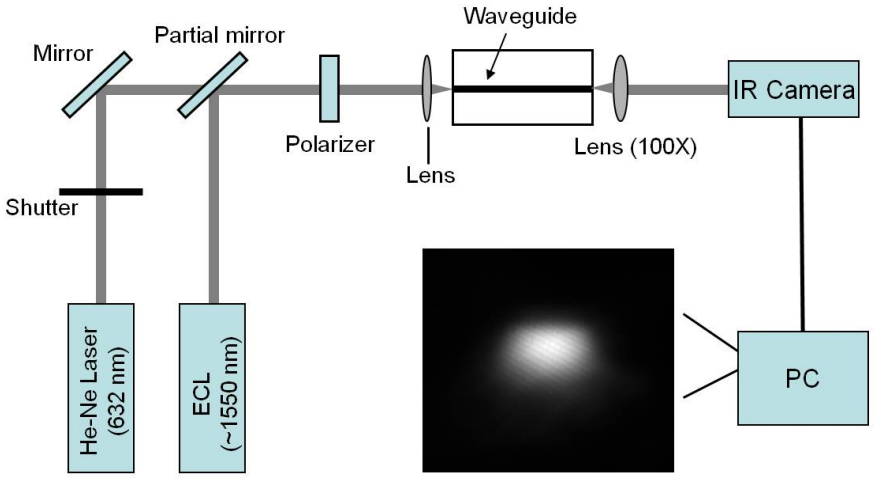

Figure 4.2: Schematic diagram of the setup to measure the mode profile. IR: infrared.

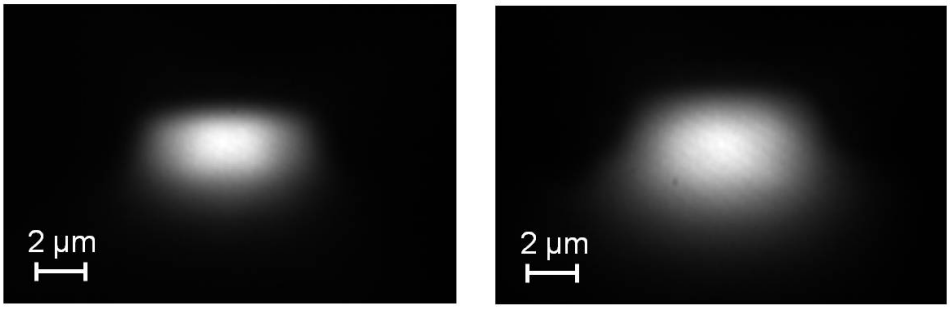

(a) (b)

Figure 4.3: Transmitted optical mode from a Ti in-diffused ridge guide of top width 7.5 μm and height 3.5 μm, Ti thickness 70 nm in (a) TE polarization and (b) TM polarization.

4.2 Periodic ferroelectric domains

4.2.1 Domain visualization using selective chemical etching

It is well known that $LiNbO_3$ ferroelectric microdomains can be visualized via selective chemical etching and imaging. The etching solution HF:HNO_3 is used for this purpose. In the inverted $LiNbO_3$ domains, both directions of Z- and Y-axis are rotated by 180°, while the crystallographic X-axis remains the same. +Z and −Z faces of $LiNbO_3$, as well as +Y and −Y faces, have significantly different etching rates in HF:HNO_3 solution. In HF:HNO_3 (HF concentration : 24%) solution, the etching rate for −Z face of

Ti th.	Ridge top	TE		TM	
$[nm]$	width $[\mu m]$	Hor. $[\mu m]$	Vert. $[\mu m]$	Hor. $[\mu m]$	Vert. $[\mu m]$
70	6.5	3.9	2.9	4.8	4.4
	7.5	4.3	3.0	5.2	4.2
80	6	3.6	3.2	4.6	4.8
	8	4.4	3.0	5.2	4.1

Table 4.2: Measured FWHM horizontal (Hor.) and Vertical (Vert.) mode sizes of Ti in-diffused ridge guides on X-cut $LiNbO_3$ at 1550 nm in both TE and TM polarization of ridge guides with different top width and Ti thickness (th.).

$LiNbO_3$ is 4.7 μm per hour at 60 °C; while +Z face remains unaffected [46]. Therefore, the difference in height between +Z and −Z faces is generated after etching, and can be observed using an optical microscope.

The samples are first immersed in the etching solution for 10 minutes, and then observed from the top using differential interference contrast optical microscopy. The samples are then cut through the ridges to reveal the cross sections of the ridges. The cross section faces are carefully polished before immersed into the etching solution. Another 10 minutes of etching is applied to reveal the domain patterns in the cross sections. Undoped ridges on X- and Y-cut $LiNbO_3$ and Ti in-diffused ridge on X-cut $LiNbO_3$ are investigated using this method.

Undoped ridge

Figure 4.4 presents corresponding results of an undoped ridge on X-cut $LiNbO_3$. From figure 4.4(a) and (b), a periodical etching of the ridge side wall is observed from the top and the side. The side walls of the ridge consist of a sequence of +Z- and −Z-faces, whereas the top surface is still a homogeneous X-face. The sample is then cut through the body of the ridge as shown in figure 4.4(d) and polished before etched again. The periodic domains in the body of the ridge are observed as shown in figure 4.4(c). A hexagonal shape of the domain wall is observed as marked with white dash lines in 4.4(c). The depth of the domains (in X-direction) corresponds to the height of the ridge as expected. The duty cycle of the periodical domain structure is ∼7:3 (width of inverted to non-inverted domain) in comparison with the duty cycle of the finger electrodes of 1:1. This indicates a certain degree of overpoling.

Figure 4.5 presents similar results of an undoped ridge on Y-cut $LiNbO_3$. From figure 4.5(a) and (b), a periodical etching of the ridge side wall is observed from the top and the side. In addition to the periodic etching on the side wall, a periodic modulation of the height of the ridge can be seen because the top face contains a sequence of +Y- and −Y-faces. The periodic domains in the body of the ridge are observed as shown in figure 4.5(c). An improved duty cycle of the domain structure close to 1:1 is attributed to the optimized design of the finger electrodes as well as the voltage pulse. The shape of the domains is significantly different with a depth somewhat smaller than on the X-cut substrate.

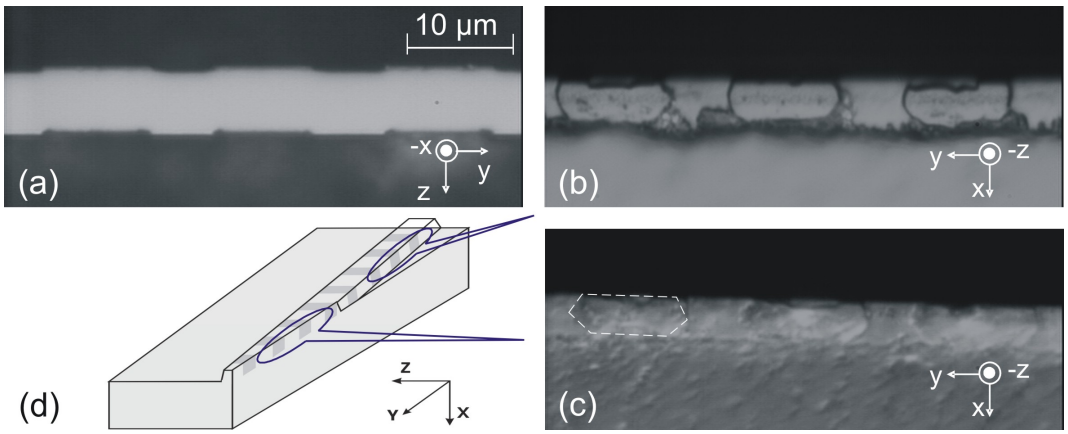

Figure 4.4: Selectively etched, periodically poled undoped ridge on X-cut $LiNbO_3$. (a) Top view. (b) Side view. (c) Side view after cutting the ridge. (d) Cutting scheme.

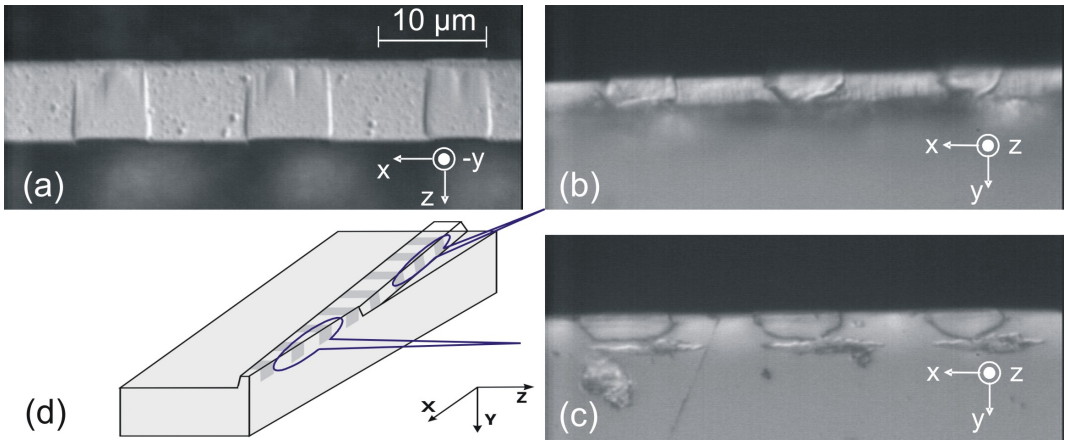

Figure 4.5: Selectively etched, periodically poled undoped ridge on Y-cut $LiNbO_3$. (a) Top view. (b) Side view. (c) Side view after cutting the ridge. (d) Cutting scheme.

Ti in-diffused ridge

Ti in-diffused ridge waveguides are etched in the etching solution. The top view of an etched ridge guide (etching time: 3 hours) is shown in figure 4.6(a); the etched cross section of this ridge guide is shown in figure 4.6(b) (cutting scheme is referred to figure 4.4(d)). In the top view, a periodically modulated pattern can be seen in both original + and −Z faces (ridge sidewalls). This indicates that the inverted domains extend from +Z face to −Z face. A hexagonal domain shape can be observed as indicated as dashed line in figure 4.6(b). Both figures show similar features as in figure 4.4(a) and (c). The duty cycle of the domain pattern is close to 1:1, suitable for efficient nonlinear interaction. Figure 4.7 presents the etched Z-face of another ridge guide on a X-cut $LiNbO_3$ substrate. The inverted domain pattern in the cross section of the ridge and on the side walls are presented respectively. A hexagonal shape of the inverted domain is clearly observed in figure 4.7.

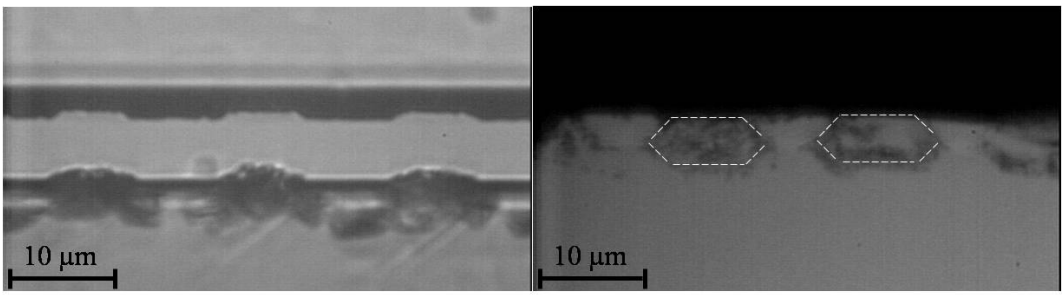

(a) (b)

Figure 4.6: (a) Top view and (b) cross section of a selectively etched, periodically poled Ti in-diffused ridge on X-cut $LiNbO_3$. The white dashed line in (b) indicate the hexagonal domain shape.

Ridge with periodical domains of 2 µm

As discussed in section 3.2, comb-like electrodes with fine periods can be fabricated. A ridge with such electrodes was poled and subsequently etched. The top view of the selectively etched ridge is presented in figure 4.8. The arrows indicate the locations of electrode fingers. However, the quality of the periodical domains, especially the duty cycle and the homogeneity is limited by the quality of the electrode fabrication (see the corresponding discussion in section 3.2). It can be improved by using E-beam lithography.

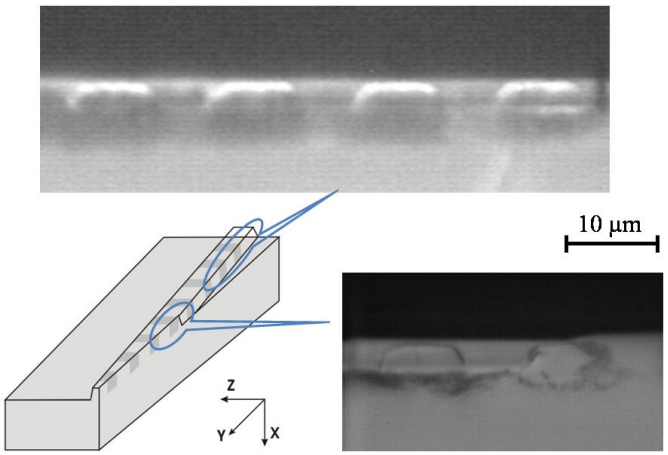

Figure 4.7: Side views of a selectively etched, periodically poled doped ridge on X-cut $LiNbO_3$.

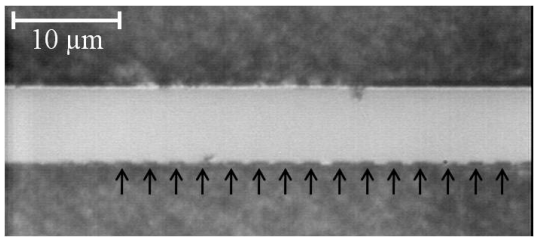

Figure 4.8: Top view of a selectively etched, periodically poled ridge of periodicity 2 μm on X-cut $LiNbO_3$.

Ferroelectric domains with different poling parameters

It has been briefly mentioned in section 3.2 that the voltage and duration of the voltage pulse used in the electric field assisted poling play an important role in domain growth. Figures 4.9, 4.10 and 4.11 show how the growth of the inverted domain is influenced by the pulse duration and voltage.

Figure 4.9 shows the results from a doped ridge on X-cut $LiNbO_3$. It has been known that, domain inversion generally starts at randomly distributed cites, also called "nucleation cites". Seed-like inverted domains then immediately grow from the nucleation cites. These seed-like domains are called "filament". With a very short voltage pulse, only a few filaments can be seen as in figure 4.9(a). With a long pulse, the inverted domain continues growing through the ridge, and simultaneously growing laterally. The consequence of the lateral growth is that the filaments will finally merge and a complete domain is formed and likely increases its volume with the pulse duration as shown in figures 4.9(b) and (c), and in figures 4.10 (a)-(c) as well.

Figure 4.11 shows the comparison of the domain inversion in the ridge poled using a voltage pulse of a fixed duration but of different voltage levels. The images in figure 4.11 are top views of the chemically etched ridges on Y-cut $LiNbO_3$. On the ridge poled with 300 Volts pulse as shown in figure 4.11(b), only a few flaments are observed, indicating

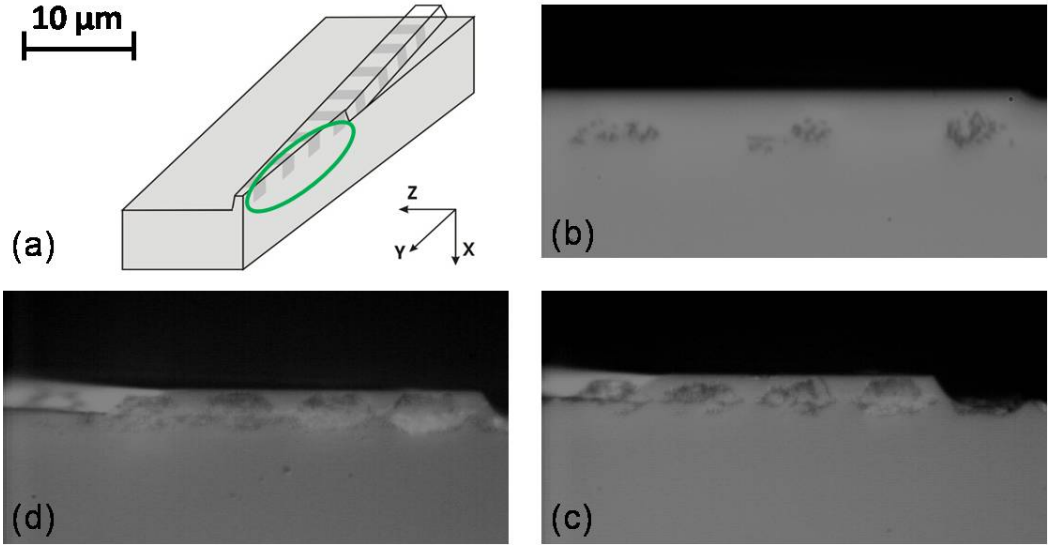

Figure 4.9: Selectively etched doped ridge of top width 8 μm on X-cut $LiNbO_3$ poled using a voltage pulse of (b) 500 Volts, 3 ms duration; (c) 400 Volts, 30 ms duration and (d) 500 Volts, 60 ms duration. (a) Cutting scheme, the circled area is imaged.

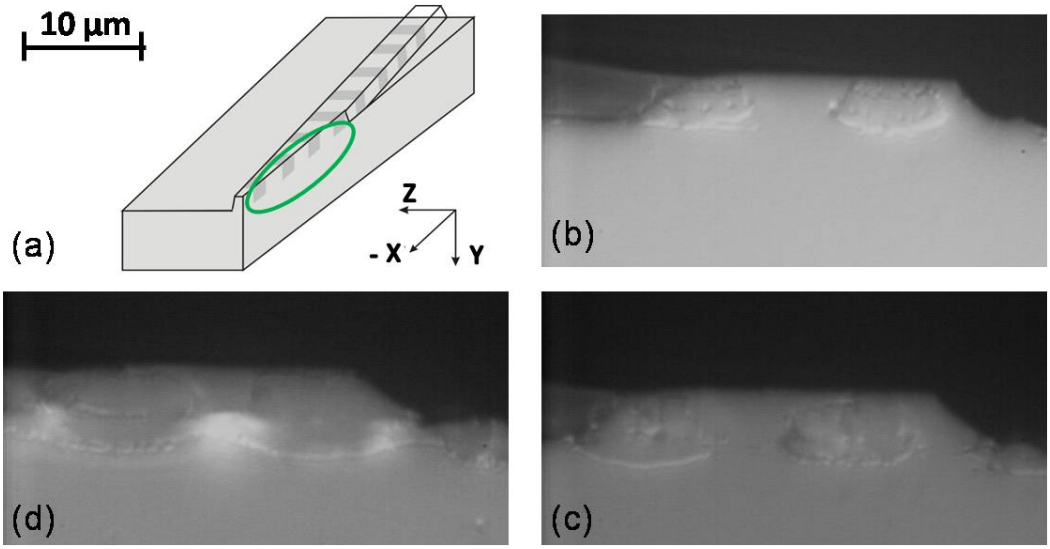

Figure 4.10: Selectively etched doped ridge of top width 7 μm on Y-cut $LiNbO_3$ poled using a voltage pulse of 600 Volts and different duration (b) 20 ms, (c) 30 ms and (d) 50 ms respectively. (a) Cutting scheme, the circled area is imaged.

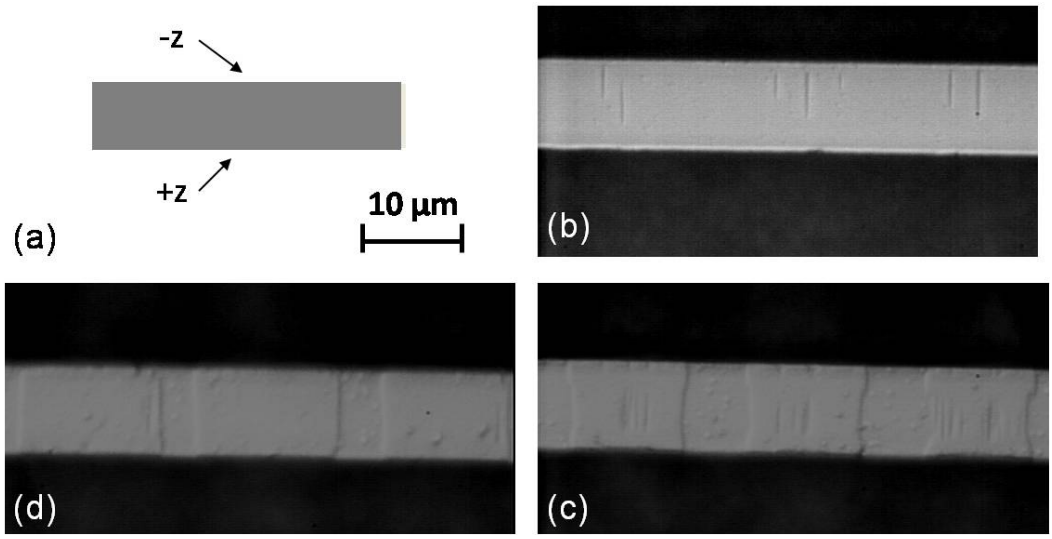

Figure 4.11: Top views of selectively etched undoped ridge of top width 8 μm on Y-cut $LiNbO_3$ poled using a 20 ms voltage pulse of (b) 300 Volts, (c) 500 Volts and (d) 700 Volts respectively. (a) Imaging scheme and $+z$ and $-z$ indicate the crystallographic orientation of the side walls of the ridge.

an insufficient domain inversion. The inverted area is evidently broader when a pulse of higher voltage was applied.

Material damage during poling

High voltage and long pulse duration not only broaden the inverted domains, but also induce surface damage in the region under the electrodes with positive polarity. This is due to the large amount of charges migrating through the surfaces rapidly during poling. The damaged crystal can be attacked by the etching solution much more easily than the intact crystal. Figure 4.12 shows examples of some surface damages of the ridge guides revealed by chemical etching. Dashed lines indicate the location of electrodes which have been removed by chemical etching. Figure 4.12(a) is taken from the top surface of a periodically poled ridge guide in which the tips of the comb-like electrodes reached the top surface of the ridge. Since the domain inversion typically starts in the vicinity of the electrodes tips, the region around the tips, the top surface near the edge in this case, suffers a certain degree of damage. Figure 4.12(b) is taken from the ground surface of a periodically poled ridge guide. An atomic force microscopy (AFM) image of a scratch-like mark is shown in figure 4.12(c). The damage appears typically as scratch-like lines along one direction which orients at $\sim 60^\circ$ with respect to the Z-axis. The surface damage induced by poling could introduce additional scattering centers; therefore, increase the propagation loss.

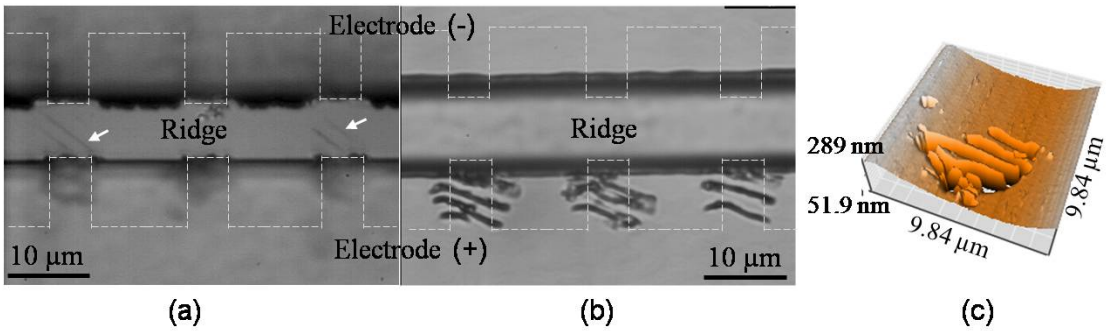

Figure 4.12: Images of surface damage on periodically poled ridge guides on a X-cut $LiNbO_3$ substrate revealed by chemical etching: (a) a top surface of a ridge guide where the electrode tips are on the top surface, (b) ground surface of the ridge guide; (c) AFM image of the scratch-like surface damage on the substrate.

4.2.2 Domain visualization using CLSM

Confocal laser scanning microscopy (CLSM) is regarded as a powerful nondestructive method of imaging material. Nonlinear CLSM is especially helpful for 3-D imaging of ferroelectric domains in the material such as $LiNbO_3$. Visualizing ferroelectric domains using CLSM is done in collaboration with the research group of "Optoelektronik und Spektroskopie an Nanostrukturen" (University of Paderborn); the measurements are performed by Berth et.al..

Experimental nonlinear CLSM setup used in this work is sketched in figure 4.13. In this special configuration the incoming laser beam is focused by an infinity-corrected microscope objective to a diffraction-limited spot. The signal to be detected is focused likewise by a detector lens onto the confocal pinhole. A pinhole placed in front of the detector is responsible for the confocal characteristic of the system. A pinhole of 2 μm diameter is typically used in this measurement. Information, which does not originate from the focal plane of the microscope objective, is faded out by this arrangement. The advantage of out-fading information from above or below the focal plane enables the confocal microscope to perform depth-resolved measurements. Image acquisition is accomplished by scanning the sample with a nano-positioner under the condition of a spatially fixed laser focus. A 3-D image can be obtatined by scanning of sequential levels. The adjustment of the optical system (pinhole modules, objectives, intermediate imaging, fiber-coupling, etc.) is driven by piezo-actuators, which are realized as piezoelectric inertial-drives. Two display-units (LED, CCD, beam splitter) are used for conventional microscopy. A detailed introduction of nonlinear CLSM and its application in imaging Z-cut PPLN can be found in [47].

In the linear operation mode, a Ti:sapphire laser (780 - 820 nm) operating in the continuous wave mode as well as a 100 mW diode pumped solid state laser (DPSSL) with an emission wavelength of 473 nm are available. By using the DPSSL the lateral

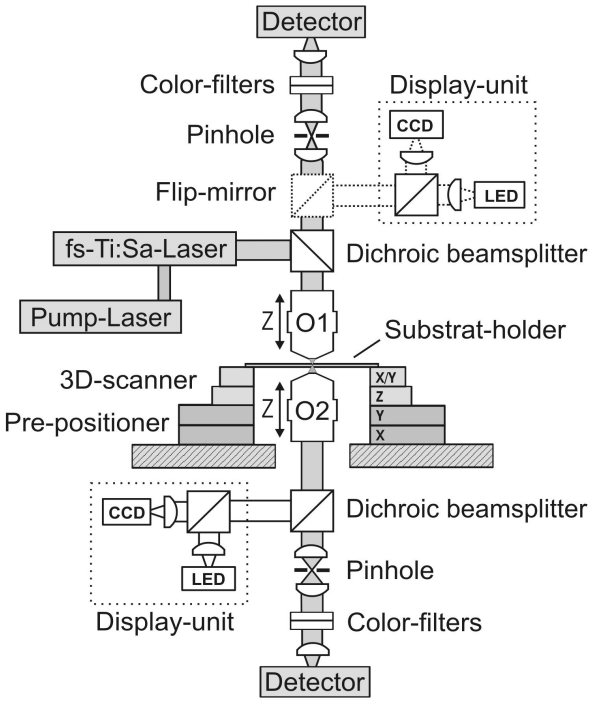

Figure 4.13: Sketch of the experimental nonlinear CLSM.

resolution was determined to be ∼300 nm and the axial resolution to ∼500 nm. A tomography image of the sample can be obtained using the linear mode. In the nonlinear operation mode, a 20 fs mode-locked Ti:sapphire laser (Femtosource C-20) is pumped by a frequency doubled Nd:YVO_4 laser. The Ti:sapphire laser with an average output power of 500 mW at a centre wavelength of 800 nm emits ∼100 fs pulses with a repetition rate of 80 MHz. For the spectral separation of the fundamental and the SH signal, dichroic beam splitters and additional colour bandpass filters are placed in the detection path. The SH signal is detected by single photon counters based on avalanche photodiode modules. A Glan-Thomson-prism is used for polarization analysis. Undoped ridge on X- and Y-cut $LiNbO_3$ has been investigated using nonlinear CLSM in this work. Figure 4.14 presents images of the top face of of an undoped ridge of 9 μm width and 2 μm height on X-cut $LiNbO_3$ using linear 4.14(a) and nonlinear 4.14(b) modes. Since the sample has been slightly etched in HF:HNO_3 beforehand, a faint periodic edge modulation can be seen in 4.14(a).

Figures 4.15 and 4.16 represent nonlinear CLSM images of undoped ridge on X-cut and Y-cut $LiNbO_3$ respectively. In both figures, strong SH signals are seen periodically along the ridge, and the period coincides with the duty cycle of the domain pattern. Signals are also detected from the surface on both sides of the ridge with somewhat different intensity; it is typically strong on the side where the positive electrode was originally placed. It is understood that the domain inversion in X(Y)-cut $LiNbO_3$ using a countering comb-like electrode takes place in a way, that starts from the positive side of the electrode, grows towards the countering electrode, in the meantime expands in

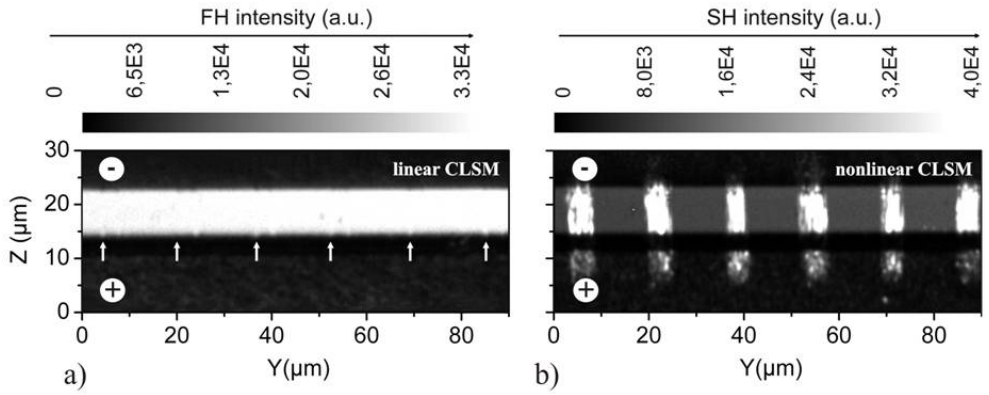

Figure 4.14: CLSM images of the top surface of an undoped ridge of 9 μm width and 2 μm height in (a) linear mode and (b) nonlinear mode.

the area beneath the positive electrode [43]. It is also noted that the samples have been previously etched in HF:HNO_3 solution. The crystal under the positive electrode often suffers damage from large amount of charge migration, the damaged crystal is easily attacked by the etching solution, resulting in rough surface. The strong signal seen from the surface originally under the positive electrode could be the scattered signal from the damaged surface.

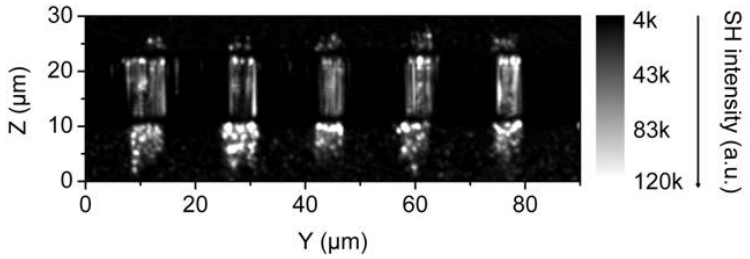

Figure 4.15: Nonlinear CLSM image of the top surface of a periodically poled undoped ridge on X-cut $LiNbO_3$.

However, the reason for strong signal detected inside the area where domain inversion took place is not entirely clear. According to the previous research in Z-cut PPLN, domain wall on the surface tends to induce less SH signal than the area far from the wall due to the scattering, whereas the situation becomes opposite when imaging the domain beneath the surface. What has been seen in X(Y)-cut $LiNbO_3$ is completely different from that in Z-cut PPLN. One possible cause could be the existence of the domain filaments or fragments embeded under the surface. In that case, the clear domain wall as we see in 4.4 does not exist, instead a group of small domain walls surrounding filaments or fragments may induce complex scattering and interference of the light. This can be seen more clearly in figure 4.17. Figure 4.17(b) shows a nonlinear CLSM image of scanning the top face of a periodically poled ridge, while the chemical etched cross section of this ridge is shown in figure 4.17(a). The inverted domains inside the ridge appear smaller and having more seed-like structures surrouding.

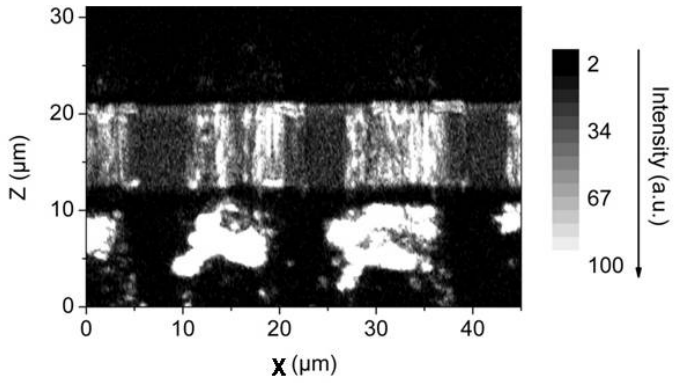

Figure 4.16: Nonlinear CLSM image of the top surface of a periodically poled undoped ridge on Y-cut $LiNbO_3$.

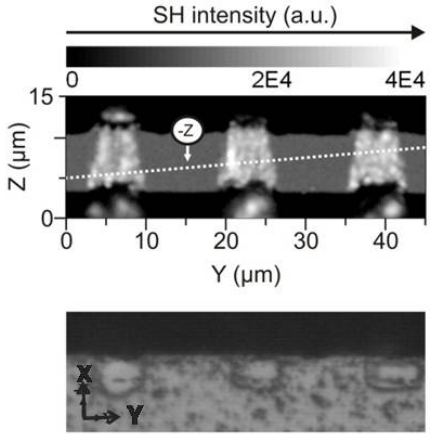

Figure 4.17: Charaterization of a periodically poled undoped ridge on X-cut $LiNbO_3$ using (a) nonlinear CLSM and (b) selective chemical etching. Graph (b) represents the etched cross section whose position is indicated as a dashed line in graph (a).

One advantage of using a nonlinear CLSM is that the inner structure of the material can be studied undestructively via 3-D scanning. In figure 4.18, images are taken in the Y-Z plane at different depth from the top of the ridge down to the substrate. The evolution of the SH signal inside the ridge overall decreases; the region of high intensity SH signal slightly shrinks along the depth and the intensity decreases faster in this region. Figure 4.19 scanning in the X-Y plane along the central line of the ridge shows a similar behavior as in figure 4.18. Both figures indicate that the domain inversion region is as deep as $\sim 4\ \mu m$ which is consistent with the results discussed in the last section.

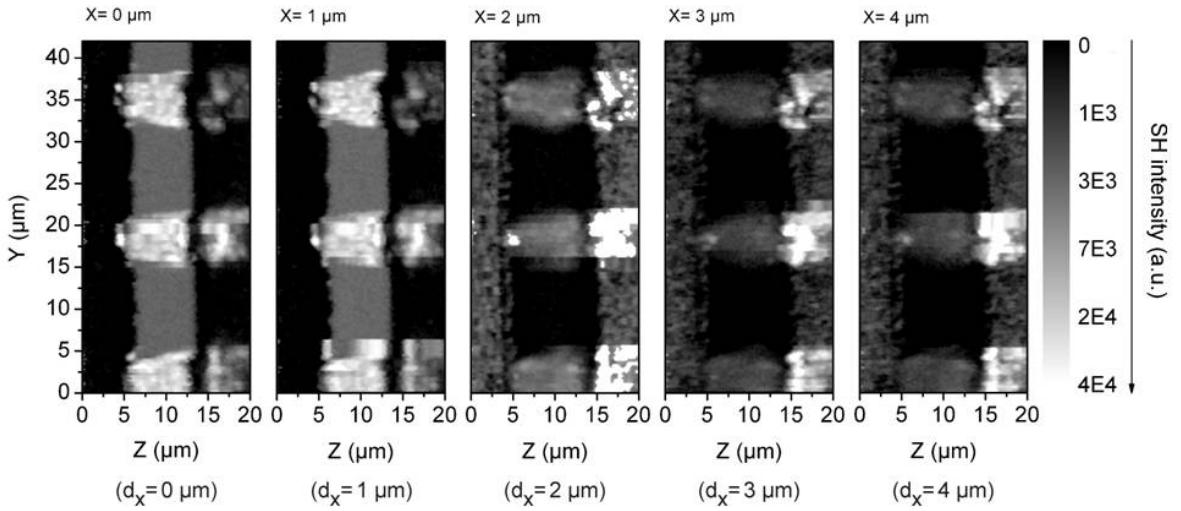

Figure 4.18: Nonlinear CLSM image of a periodically poled undoped ridge on X-cut $LiNbO_3$ at different depth.

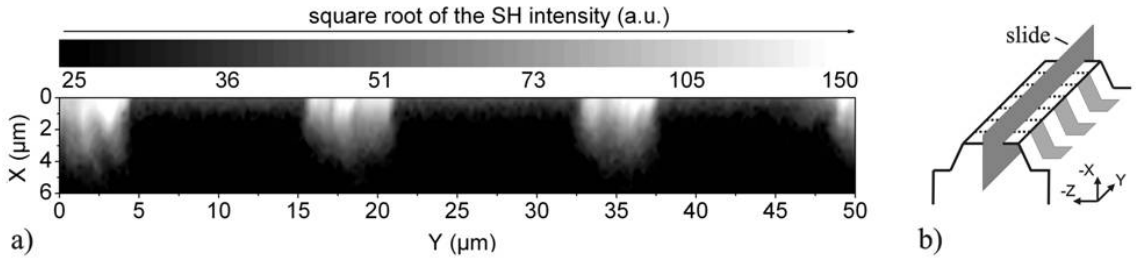

Figure 4.19: (a) Depth resolved nonlinear CLSM image of a periodically poled undoped ridge on X-cut $LiNbO_3$ scanned along the plane sketched in (b).

4.3 Summary

In this chapter, ridge guides and ferroelectric domains have been characterized.

Ridge guides are characterized in terms of waveguide propagation loss and mode size in both TE and TM polarizations. The propagation loss (mainly scattering loss) varies with the geometric design of the ridge and the thickness of Ti layer. In general, propagation loss in TE polarization is higher than in TM polarization; within the top width of 5 - 9 μm, the propagation loss decreases with the increase of the top width. Ridge guides, which have been used in this work to demonstrate nonlinear ineteraction, have the propagation loss of 0.7 - 1.2 dB/cm. The mode sizes of the ridge guide are evidently smaller than that of the conventional channel waveguide, typicallly $\sim$4 μm horizontally and $\sim$3 μm vertically in TE polarization.

Ferroelectric domains are characterized by two different methods: selective chemical etching and imaging; nonlinear CLSM imaging. Selective chemical etching is performed

on the surface of the sample as well as the cross section of the ridge after cutting through the ridge and polishing. The result reveals that a successful poling in the ridge on X-cut $LiNbO_3$ induces a hexagonal domain shape which agrees with the common knowledge of $LiNbO_3$ ferroelectric domains. The inverted domain is as deep as up to $\sim 5\ \mu m$, sufficient to overlap the transmitted mode inside the ridge guide. The duty cycle of the periodic domains can be controlled by optimizing the duty cycle of the comb-like electrodes together with the duration and voltae of the voltage pulse(s) applied during poling. Nonlinear CLSM imaging, as a powerful nondestructive method, has been applied to investigate some of our ridge guides. The domain profile on the surface as well as in the depth are imaged using this method. The results agree with that obtained from the selective chemical etching. Although a solid explanation of why the inverted domain induces higher signal has not been reached, the existence of filaments in the inversion area could be one reasonable speculation.

Chapter 5

Nonlinear optical interactions

Nonlinear optical interactions, specifically SHG and cascaded SHG/DFG, are ivestigated using a periodically poled Ti in-diffused ridge guide on X-cut $LiNbO_3$. The experimental setups are presented. The tuning characteristics and power characteristics of SHG are discussed in section 1. The experimental results of cascaded SHG/DFG are discussed in section 2.

5.1 Second harmonic generation (SHG)

SHG is investigated using periodically poled Ti in-diffused ridge waveguides on X-cut LN of different geometric dimensions (top width, ridge height and length). The period of the periodically poled section is 16.2 μm and 16.6 μm respectively. The two different periodicities combined with temperature tuning allow to vary the phase matching wavelength up to 1560 nm. The end faces of the waveguide have been carefully polished in order to couple the light efficiently. The measurement setup is sketched in figure 5.1. An external cavity laser (ECL) is used to tune the fundamental wavelength λ_f in steps of 1 pm around λ_f =1550 nm. A polarization controller is used to adjust the polarization of the beam. The interaction is designed for converting a fundamental wave of TE polarization into a SH wave of TE polarization. An erbium doped fiber amplifier (EDFA) is then used to amplify the optical power of the fundamental wave. In this way, the tuning characteristics can also be measured at high fundamental power. The fundamental wave is coupled to the waveguide by fiber butt coupling with some index matching oil between fiber and waveguide end face. In this way the reflectivity of the front face was reduced to $\sim$3.6 % from $\sim$14 %, determined by the index step between LN and air. The light is coupled out from the waveguide by either free space coupling using a focusing lens or by fiber butt coupling. A Silicon photodiode is used to measure the generated SH power. The experiments are operated at room temperature; a temperature controller is used to keep the sample at 25 °C.

Figure 5.2 presents a typical SHG tuning characteristic as generated second harmonic power P_{SH} versus λ_f =$\sim$1548 nm together with the transmitted fundamental power P_f. The ridge waveguide is 13 mm long and has a domain period of 16.6 μm, and it has a

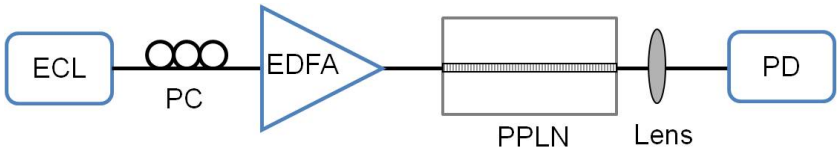

Figure 5.1: Sketch of a setup for SHG characterization. ECL: external cavity laser. PC: polarization controller. EDFA: erbium doped fiber amplifier. PD: photodiode.

cross section of 6.5 μm width and 3.5 μm height. Fabry-Perot resonances of both waves are observed. The resonances are induced by the cavity with approximately 3.6 % and 14 % mirror reflectivities. Similar to the method used in section 4.1.1, the resonances allow evaluating precisely the propagation losses of 1.0 dB/cm for this waveguide at 1550 nm. The intra-cavity modulated fundamental power in turn modulates the generation of the second harmonic power. Due to the nonlinear interaction the corresponding resonances become narrower; moreover, they are also modified by Fabry-Perot resonances at the second harmonic wavelength λ_{SH} (see inset of the figure 5.2). Fitting a theoretical SHG tuning characteristic (red curve in figure 5.2) to the average of the experimental result yields a good agreement of theoretical and measured bandwidth of 0.8 nm demonstrating the excellent homogeneity of the periodically poled waveguide along the interaction length.

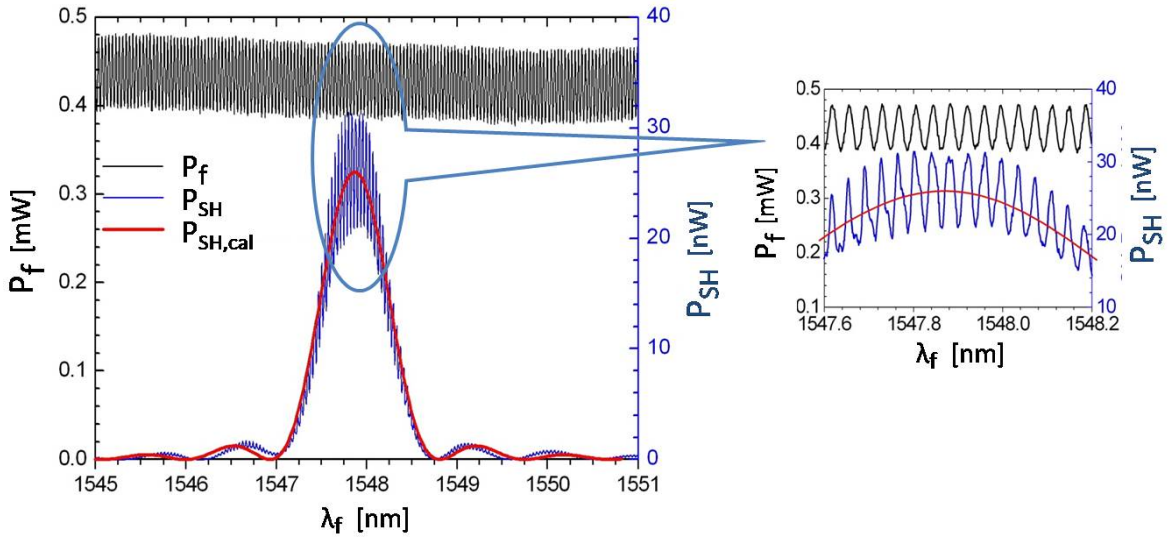

Figure 5.2: Generated SH and transmitted fundamental powers as a function of the fundamental wavelength for a 14 mm long, periodically poled ridge waveguide on X-cut LN. Inset: Results around the maximum efficiency plotted with higher resolution.

SHG was also investigated as function of the fundamental power up to ~700 mW; the tuning characteristics at different coupled fundamental power levels are shown in figure 5.3. With increasing fundamental power, the phase matching wavelength (the peak of the tuning curve) shifts slightly to shorter wavelength, and the tuning charac-

teristic becomes asymmetric. This could be due to the influence of the photorefractive effect at high fundamental power. As the scanning is from shorter wavelength to longer wavelength, the increase of the effective index induced by photorefraction leads to the blue-shift of the phase matching wavelength.

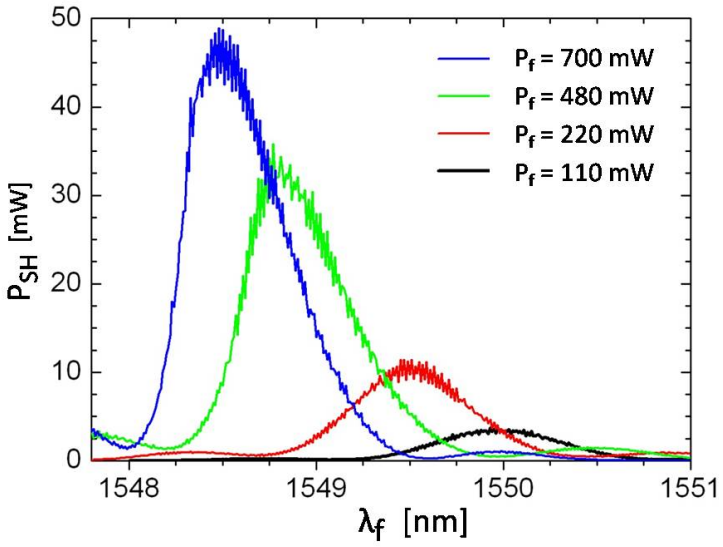

Figure 5.3: Tuning characteristics at different coupled fundamental power levels: SH power vs. fundamental wavelength.

The power characteristics of this ridge waveguide are measured at different fundamental power levels as shown in figure 5.4. At low power levels (see figure 5.4(a)) a parabolic dependence is observed, well described by an efficiency of 28 % W^{-1} normalized to the coupled fundamental power. It is calculated as the ratio of out-coupled SH power and the square of in-coupled fundamental power. The efficiency normalized to coupled fundamental power and the interaction length is 16.5 % $W^{-1}cm^{-2}$. This value is ∼50 % increased compared to the efficiency of a conventional Ti in-diffused channel waveguide. However, the measured efficiency is still lower than the theoretical conversion efficiency of 36 % $W^{-1}cm^{-2}$. This could be due to a non-ideal duty cycle of the domain structure, and larger ridge dimensions (therefore, a larger nonlinear cross section) than necessary for a maximum SHG. At higher fundamental power levels (see figure 5.4(b)), SH power first increases parabolically with respect to the fundamental power up to ∼260 mW. At even higher fundamental power levels, the growth of SH power appears to be approximately linear with respect to the increasing fundamental power. This is due to pump depletion and the onset of photorefractive effects. The SH power up to ∼50 mW is generated by this ridge guide at a fundamental power of ∼700 mW.

In spite of the influence of photorefraction, the high SH power shows a good stability with time at room temperature, as shown in figure 5.5. In other words, this ridge waveguide on X-cut $LiNbO_3$ has a lower susceptibility to the photorefractive effects than a conventional channel waveguide. This phenomenon has been first observed in a Z-cut

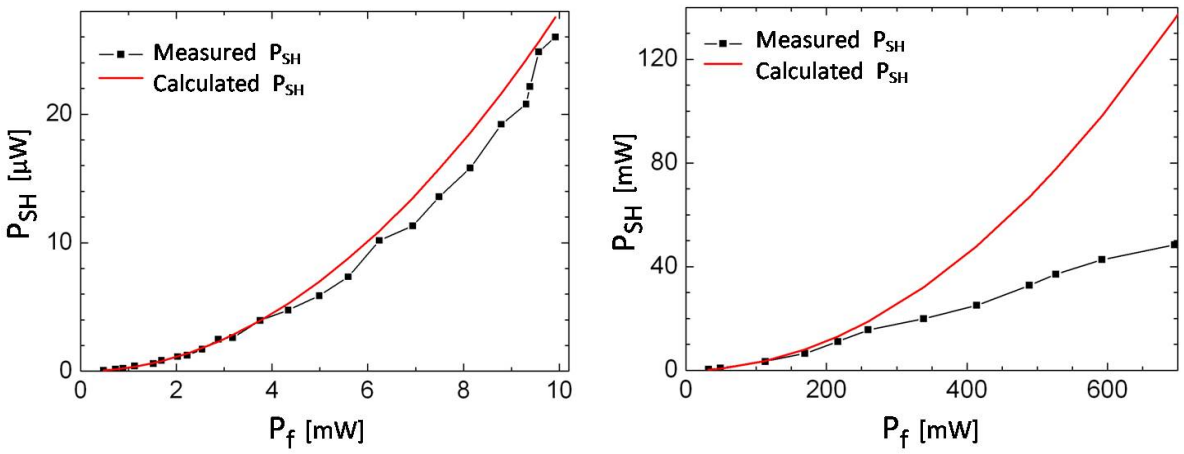

(a) (b)

Figure 5.4: Power characteristics at (a) low fundamental power levels and (b) high fundamental power levels: SH power vs. fundamental power.

$LiNbO_3$ ridge guide by Nishida et. al. [40]. The mechanism of the low susceptibility of photorefractive effects could be that the electrons generated via photorefraction can move to the surface of the ridge, then compensated from the ambient environment due to the unique geometry of the ridge. Therefore, no sustained electric field generated by the photorefraction exists in the waveguide to induce the change of the refractive index. Such a high power stability is of special interest for the practical use of PPLN waveguides. In this way, no complicated heating system is required in the nonlinear optical devices such as wavelength converter.

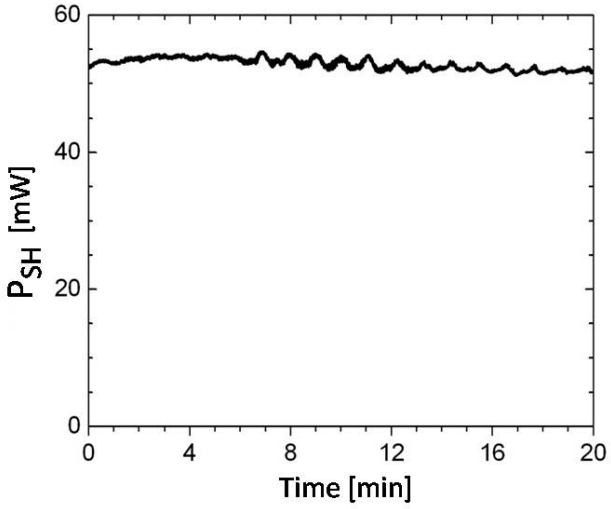

Figure 5.5: Generated SH power as a function of time at room tempeature.

The tuning of the SH wavelength with respect to the fundamental wavelength could be achieved by temperature tuning. Figure 5.6 shows the tuning characteristic at the

same coupled fundamental power at different temperature. The phase matching wavelength shifts towards longer wavelength with increasing temperature. This is due to the dependence of the refractive index of $LiNbO_3$ on the temperature. The actual SH power at the phase matching wavelength slightly decreases at the higher temperature due to the degradation of the coupling efficiency.

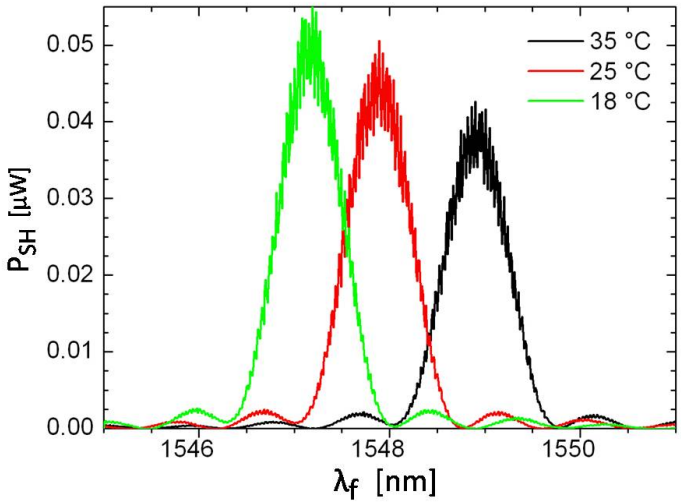

Figure 5.6: Tuning characteristics at different temperature.

Tuning characteristic of the waveguide in a broader fundamental wavelength range (1500∼1570 nm) is measured in a ridge guide of 14 mm long, 16.6 μm QPM structure and a cross section of 8.5 μm width and 3.5 μm height. The tuning characteristic is shown in figure 5.7. Three phase matching peaks are observed at λ_f =∼1503, ∼1548 and ∼1560 nm respectively. The SH modes at the peak fundamental wavelengths are taken by a CCD camera as shown in the insets of figure 5.7. The highest SH power at the fundamental wavelength λ_f =∼1548 nm is due to TE_{00} mode of SH wave generated from TE_{00} mode of fundamental wave. The SH mode observed at the fundamental wavelength λ_f =∼1560 nm is due to TE_{10} mode of SH wave generated from TE_{00} mode of the fundamental wave. Similarly, the SH mode observed at the fundamental wavelength λ_f =∼1503 nm is due to TE_{20} mode of SH wave generated from TE_{00} mode of the fundamental wave. However, the generated SH power of these two modes are much weaker than the SH power of TE_{00} mode generated at the phase matching at λ_f =∼1548 nm.

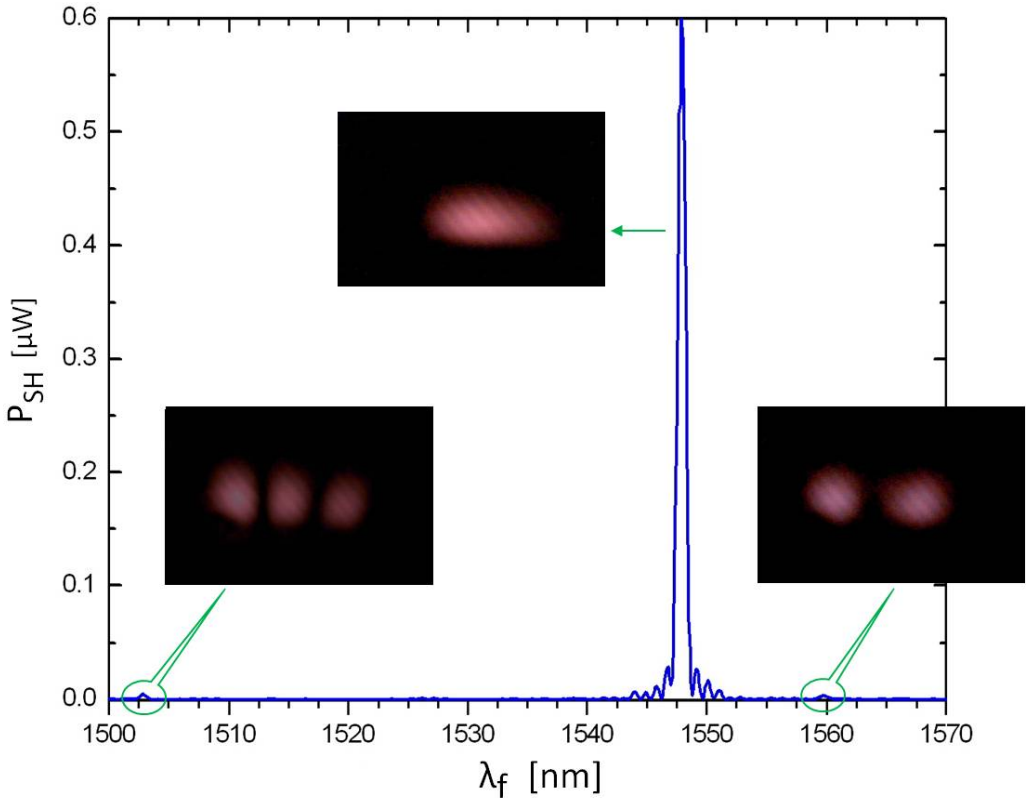

Figure 5.7: SH generation in a broad fundamental wavelength range: SH power vs. fundamental wavelength.

5.2 Cascaded second harmonic generation and difference frequency generation (cSHG/DFG)

Wavelength conversion based on a cascaded scheme as discussed in section 2.4 is demonstrated using a periodically poled Ti in-diffused ridge waveguides on X-cut LN of 13 mm length and 16.6 μm period. The schematic diagram of the experimental setup is sketched in figure 5.8. The fundamental wave is generated by ECL, then amplified using an EDFA. The signal wave is supplied by a distributed feedback laser (DFB) at ∼1555.5 nm. Both the fundamental wave and signal wave are coupled into the waveguide via a circulator and fiber butt coupling. A fiber bragg grating (FBG) is inserted between DFB and circulator in order to reflect the fundamental wave back to the circulator. Polarization controllers are used to adjust both fundamental and signal waves to TE polarization. The spectrum from the waveguide is measured using an optical spectrum analyser (OSA).

The calculated evolutions of the power levels of the interacting waves are shown in figure 5.9 as a function of the interaction length (the coupled fundamental power of

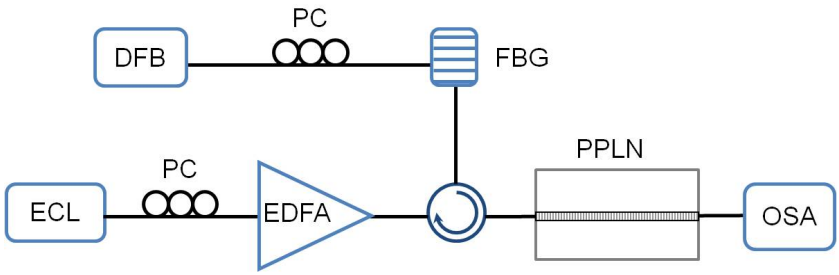

Figure 5.8: Sketch of a setup for cascaded SHG/DFG characterization. ECL: external cavity laser. PC: polarization controller. EDFA: erbium doped fiber amplifier. DFB: distributed feedback laser. OSA: optical spectrum analyser. FBG: fiber bragg grating.

$\sim$200 mW). According to the discussion in section 5.1, the normalized efficiency of SHG is 16.5 $\%W^{-1}cm^{-2}$. However due to the short length of the sample (13 mm), the overall conversion efficiency for SHG is 28 $\%W^{-1}$. Because of the low power of a SH wave, the following DFG can be considered as a non-pump depletion process. In figure 5.9, the fundamental power decreases with the interaction length due to both propagation loss and pump depletion in SHG process. The SH power increases parabolically along the interaction length. The signal power decreases due to the propagation loss. The generated idler wave first increases quadruply as a function of the interaction length, then shows a weaker growth due to both the propagation loss and the decrease of signal power. The conversion efficiency of this cascaded process is -26.5 dB, evaluated as the generated idler power devided by signal power at the end of the interaction length.

The output of the waveguide is measured in the wavelength range of 1540 - 1557 nm at the fundamental power of $\sim$200 mW, as shown in figure 5.10. The fundamental wave at 1548.5 nm generates SH wave at 774.25 nm. This SH wave and the signal wave at 1555.5 nm then generate the idler wave at 1541.5 nm. A conversion efficiency of -29 dB is obtained from the spectrum. This efficiency is close to the calculated conversion efficiency in figure 5.9. The generated idler wave also shows a good stability as shown in figure 5.11, in accordance with the stable SHG discussed in section 5.1.

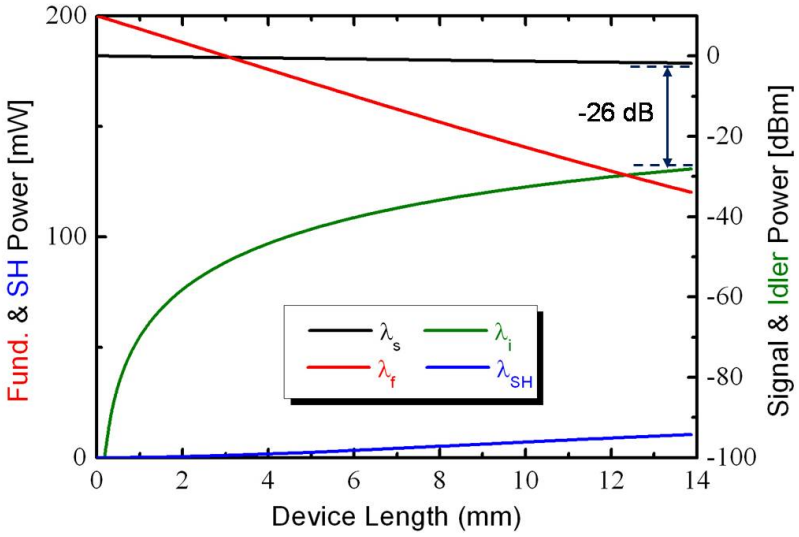

Figure 5.9: Calculated power evolution of fundamental, SH, signal and idler waves in cSHG/DFG interaction assuming a coupled pump power of ∼200 mW: fundamental power and SH power are in linear scale on the left vs. interaction length; signal power and idler power are in logarithm scale on the right vs. interaction length.

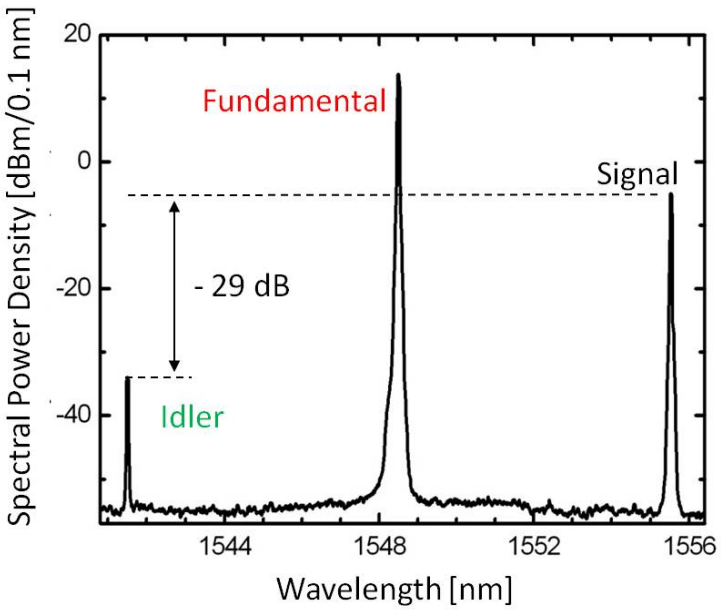

Figure 5.10: Measured spectral power of fundamental, signal and idler waves in cSHGDFG interaction at a coupled pump power of ∼200 mW (Resolution: 0.1 nm): spectral power density vs. wavelength.

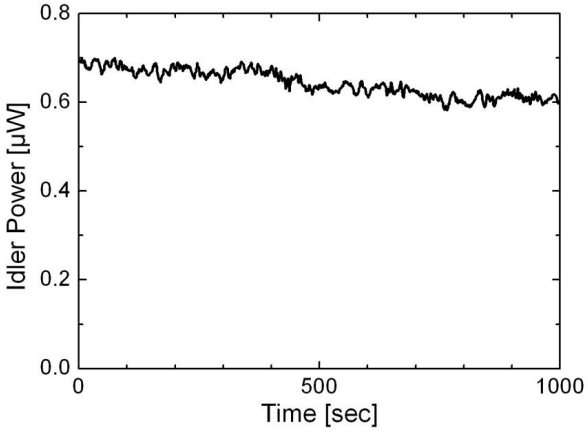

Figure 5.11: Generated idler power vs. time at room temperature.

5.3 Summary

In this chapter, nonlinear interactions are investigated using periodically poled Ti in-diffused ridge waveguides on X-cut $LiNbO_3$ at room temperature.

The tuning characteristics and power characteristics of SHG in Ti in-diffused ridge guides are investigated. A normalized conversion efficiency of 16.5 % $W^{-1}cm^{-2}$ is obtained. This normalized efficiency is 50 % higher than that in a Ti in-diffused conventional channel waveguide. A stable SH power up to ∼50 mW is obtained.

Wavelength conversion based on a cascaded SHG/DFG scheme is also demonstrated using such a ridge waveguide. A conversion efficiency of −29 dB from a signal wave to an idler wave is measured when ∼200 mW fundamental power is coupled, close to the calculated efficiency of −26.5 dB.

Good stability of both the generated SH wave in SHG and the idler wave in cascaded SHG/DFG at room temperature shows that the Ti in-diffused ridge waveguides on X-cut $LiNbO_3$ have lower susceptibility to the photorefractive effects compared to Ti in-diffused $LiNbO_3$ channel waveguides. This property enables room temperature operation of high power nonlinear interaction, leading to broad interest in the actual applications.

The conversion efficiency in both processes could be further improved. This will be achieved by reducing the propagation loss of the waveguide and improving the quality of the periodical domains especially the duty cycle and using a longer waveguide.

Chapter 6

Periodically poled LNOI material platform and photonic wires

As discussed in sections 1.2 and 2.5, $LiNbO_3$ waveguides of high refractive index contrast are of increasing interest. The high refractive index contrast enables ultra-small waveguide cross sections below 1 μm^2 (see figure 6.1 (a)) and bending radii smaller than 10 μm (see figure 6.1 (b)). Therefore, ultra-compact photonic devices and circuits can be developed. Researchers from CUDOS [2] have blueprinted the next generation of optical systems built in miniaturised photonic chips of the order of only millimetres in size (see figure 6.2).

In contrast to photonic wires in Silicon-On-Insulator (SOI) [48], LN offers excellent electro-optic, acousto-optic, and nonlinear optical properties; moreover, it can be easily doped with rare-earth ions to become a laser active material. Therefore, LN photonic wires will enable the development of a wide range of active integrated devices. They comprise electro-optical modulators, tunable filters, nonlinear wavelength converters, and amplifiers and (tunable) lasers of different types. Due to high mode intensities even at moderate optical power levels, devices of a high efficiency can be expected. It is promising that ultra-compact and highly efficient $LiNbO_3$ based photonic chips will be realized in the near future.

The most promising method of fabricating high index contrast waveguides is to use ion-slicing and crystal-bonding techniques, also called "smart-cut" technique. The concept of Lithiun Niobate-On-Insulator (LNOI) (in this work, the insulator is SiO_2) and its fabrication technique are inspired from Silicon-on-Insulator (SOI) technology [49]. In this work, 3" LNOI wafers fabricated by Hu [50], are used to produce ridge waveguides of submicrometer dimensions, also called LNOI "photonic wires". In order to explore nonlinear interactions in a photonic wire, a periodical domain structure is required to enable QPM interactions. Two approaches of fabricating periodically poled LNOI thin films are investigated in this work in collaboration with Hu: (i) direct bonding of PPLN and (ii) poling of a LNOI thin film. The progress of the fabrication of periodically poled LNOI (PPLNOI) material platform is presented in the first section of this chapter. In the second section, the fabrication of PPLNOI photonic wires and the results of SHG in such photonic wires are presented and discussed.

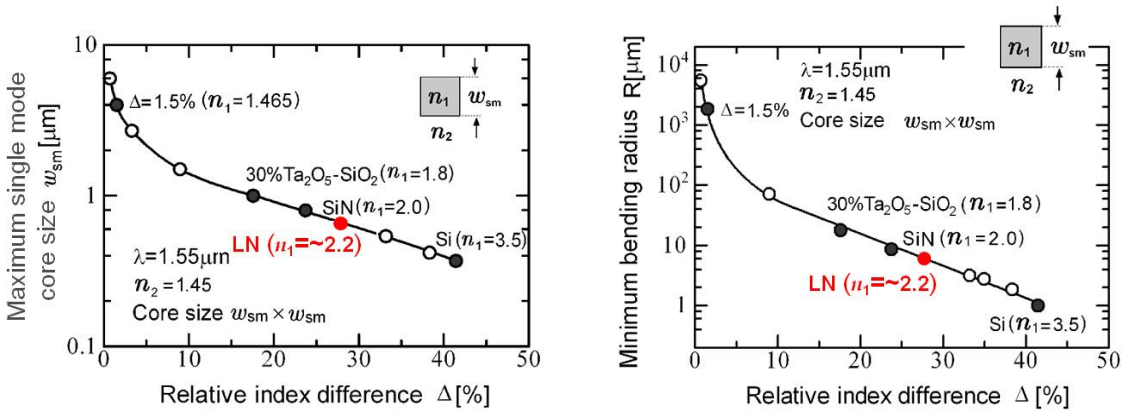

(a) (b)

Figure 6.1: (a) Relation between maximum single mode core size and relative index difference Δ. (b) Relation between minimum bending radius and relative index difference Δ. $\Delta = \frac{{n_1}^2-{n_2}^2}{2{n_1}^2}$. The red dots refer to $LiNbO_3$ as the core material. The figures are taken from [1].

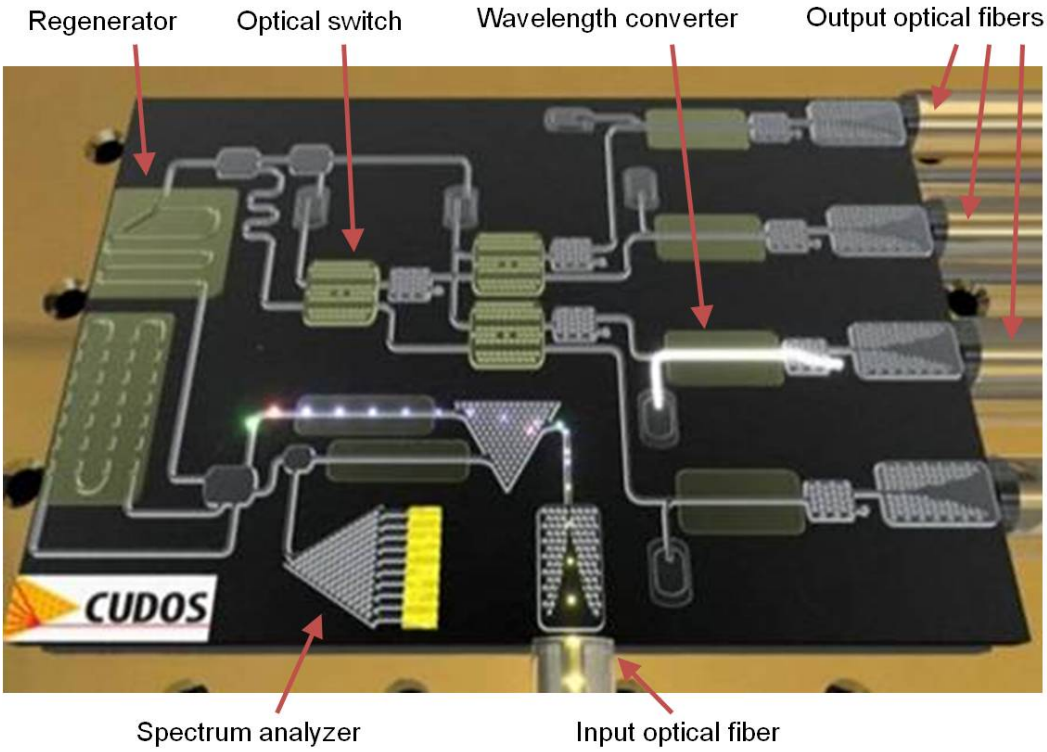

Figure 6.2: The next generation of optical systems built in a photonic chip, taken from the website of CUDOS [2].

6.1 PPLNOI material platform

6.1.1 Fabrication of LNOI

The key to fabricate LNOI wafers is the ion-slicing and crystal-bonding process developed by Hu [3, 50]. The basic fabrication procedure is sketched in Figure 6.3, and it consists of the following steps:

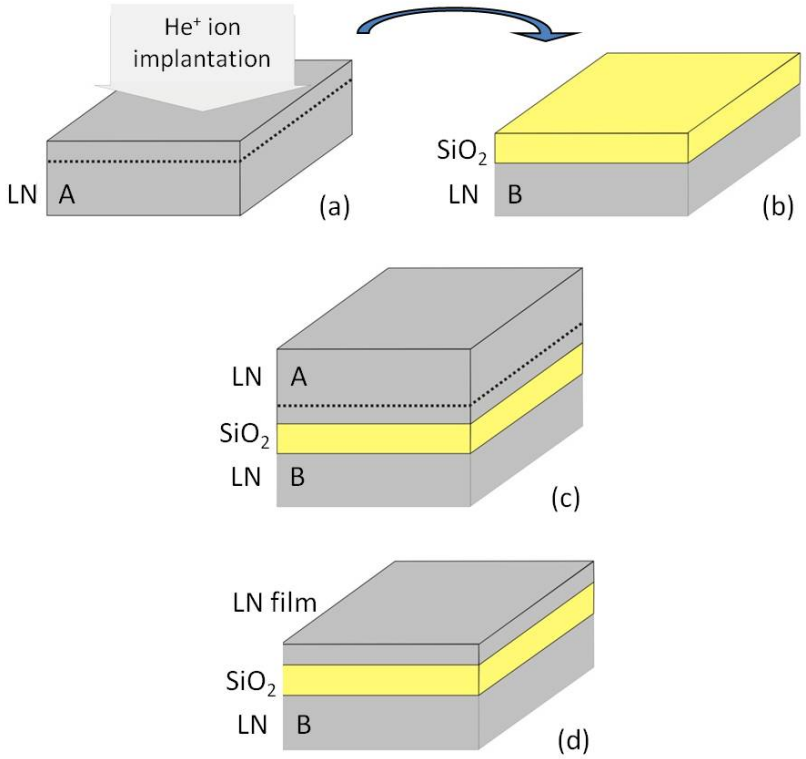

Figure 6.3: Fabrication of a LNOI wafer: (a) Ion implantation of the $LiNbO_3$ wafer A; (b) SiO_2 deposition on the $LiNbO_3$ wafer B; (c) Crystal bonding and splitting; (d) Annealing and CMP polishing.

Step 1: Wafer preparation (see figure 6.3 (a) and (b))

Two Z-cut congruent $LiNbO_3$ wafers of 0.5 mm thickness are prepared in parallel. $-Z$ face of wafer A (in figure 6.3 (a)) and $+Z$ face of wafer B (in figure 6.3 (b)) are well polished. Wafer A is then implanted by 250 - 350 keV He^+ ions with a dose of 4×10^{16} $ions/cm^2$ forming an amorphous layer underneath the surface. Wafer B, used as a handle wafer, is coated with a SiO_2 layer by plasma enhanced chemical vapour deposition (PECVD).

Step 2: Crystal bonding (see figure 6.3 (c))

Before crystal bonding, the surfaces of both wafers are carefully cleaned. Two wafers are then bonded together. The bonded pair of wafers is then annealed at elevated temperatures (165 °C and then 190 °C) to improve the bonding strength. By a further annealing procedure at 228 °C, a thin LN layer splits along the He^+ implanted layer and remains on the SiO_2-$LiNbO_3$ substrate.

Step 3: Annealing and Polishing (see figure 6.3 (d))

After crystal bonding, the sample is further annealed at 450 °C for 8 hours to increase the bonding strength. A chemical mechanical polishing (CMP) process is applied to reduce the surface roughness to below 1 nm and to remove the amorphous layer induced by ion implantation. A LNOI wafer of 3 " diameter fabricated by Hu is shown in figure 6.4.

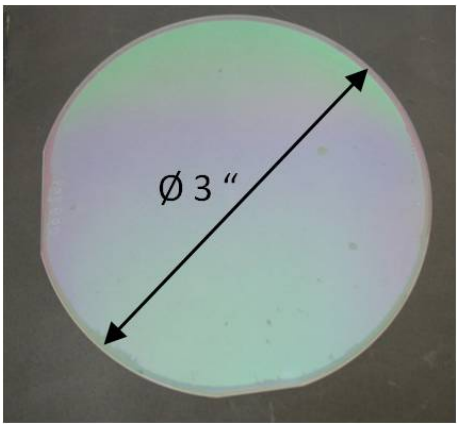

Figure 6.4: An optical micrograph of a fabricated LNOI wafer of 3" diameter taken from [3]

According to the application, various types of LNOI wafers have been fabricated using the same process but with slight modifications. For example, wafer A could be a doped $LiNbO_3$ or a periodically poled $LiNbO_3$ substrate; additional layers such as metal layers can be added into the stacked structure. These structures are discussed in more detail in the following section.

6.1.2 Direct bonding of PPLN

As mentioned above, wafer A can be a periodically poled $LiNbO_3$ substrate. In this approach, He^+ ions are implanted into a PPLN substrate using the same ion energy and dose as presented in section 6.1.1. Because ion-implantation is not sensitive to the orientation of the spontaneous polarizations of $LiNbO_3$, a uniform amorphous layer is formed beneath the surface of the PPLN substrate. The rest of the fabrication is

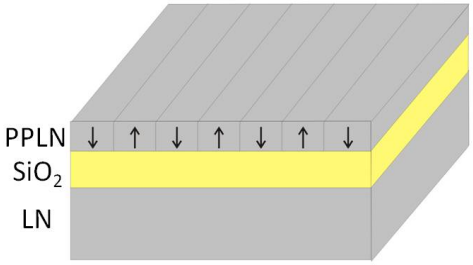

Figure 6.5: Sketch of a PPLN-SiO_2-LN thin film.

identical to the process sketched in figure 6.3. Figure 6.5 is a sketch of a PPLN-SiO_2-LN thin film.

In order to fabricate such a periodically poled LNOI thin film, PPLN substrates of a good quality are required. The basic concept of fabricating of a PPLN substrate is illustrated in figure 6.6. A thin layer (2 - 3 μm thick) of photoresist is spin-coated on a bulk $LiNbO_3$ substrate (6.6 (a)). The sample is then baked for 30 minutes at $\sim$90 °C. Afterwards, the sample is exposed and developed using either conventional photolithography or holographic lithography depending on the periodicity (6.6 (b)). A hard-baking process follows to improve the adhesion between the photoresist and the substrate surface. The baked sample is then placed inside a customized sample holder in which a high electric field is applied to the sample to invert the spontaneous polarization (6.6(c)). The detailed processes such as exposure, hard-baking and poling are different for fabricating a QPM structure of a large periodicity (generally $\geq$ 4 μm) and small periodicity. The poling concepts applied in these two different periodicity regimes are illustrated schematically in figures 6.7 (a) and (b). The details are discussed in the following.

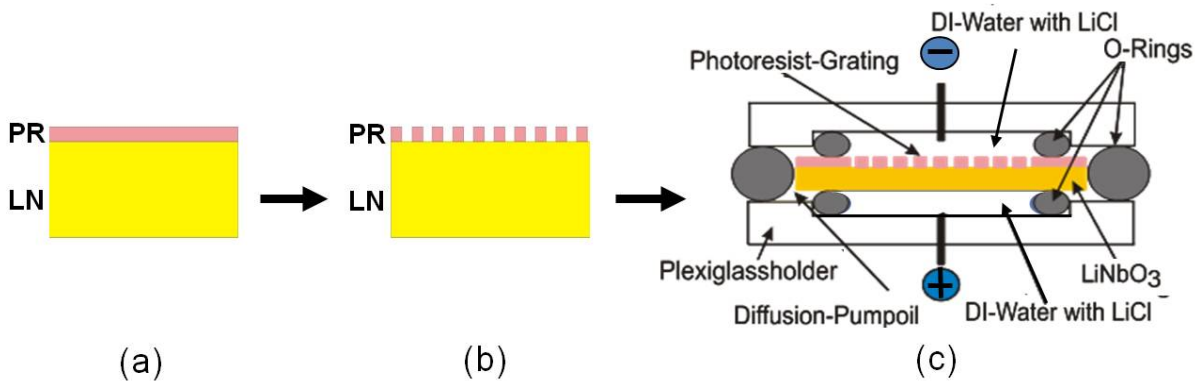

Figure 6.6: Fabrication of a PPLN substrate: (a) spin-coating of photoresist; (b) exposure and development of photoresist; (c) periodical poling.

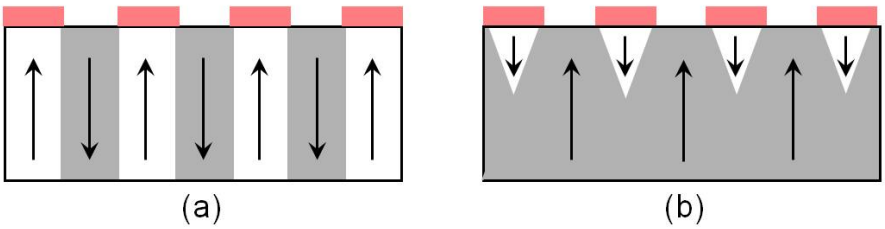

Figure 6.7: Two poling schemes: (a) conventional poling ($Q = 2 \times P_s \times A$); (b) overpoling ($Q > 2 \times P_s \times A$). The arrows represent the directions of the spontaneous polarization.

A QPM structure of large periodicity ($\Lambda \geq 4\mu m$)

To create a large periodicity QPM structure, a conventional photolithography and poling method is applied. The AZ4533 photoresist is spin-coated on the +Z surface of a $LiNbO_3$ substrate as shown in figure 6.7 (a). After the sample is exposed by a UV radiation through a photomask for ∼60 seconds and subsequently developed in a developing solvent, a photoresist grating of the desired periodicity is generated. The sample then undergoes a three-step hard-baking process (100 °C, 120 °C and 140 °C in sequence, 1 hour at each temperature) to progressively improve the adhesion between the photoresist and the substrate surface. During periodical poling, a positive high voltage is applied on the +Z face of the sample to overcome the coercive field strength of $LiNbO_3$ of ∼21 kV/mm while the −Z face is grounded. The domain nucleations start from the edges of the electrode on the +Z face, then grow towards the −Z face and simultaneously spread laterally but at a much lower speed. The poling process is controlled by monitoring the current flow through the crystal. The applied voltage is reduced gradually to 0 V after the accumulated charge reaches an empirically determined value to get a 50 % duty cycle of the domain structure. This calculated charge Q is determined by

$$Q = 2 \times P_s \times A, \tag{6.1}$$

where P_s is the spontaneous polarization of $LiNbO_3$ (∼0.72 $\mu C/mm^2$), A is the area of the region where domain inversion is supposed to happen. This poling technique is well established to fabricate a large periodicity QPM structure. When the required periodicity comes down to a few micrometers, the photoresist grating of a sufficient thickness and duty cycle is difficult to be realized using conventional photolithography due to its resolution limit. Therefore, the contrast of the electric field strengths between a clear region and a photoresist covered region is not large enough to invert the spontaneous polarization only in the clear region. This results in uncontrolled domain inversion in the whole region.

After poling and carefully cleaning the sample, the PPLN substrate is ready for ion-implantation and the subsequent processes as discussed in section 6.1.1.

A QPM structure of small periodicity ($\Lambda < 4\mu m$)

As the conventional poling method (see above) has a limitation in the small periodicity range, the "electric field over-poling" (also called "surface poling") technique [51] using a photoresist grating defined by holographic lithography is applied in this work. The mechanism of electric field over-poling can be understood in the following (see figure 6.7 (b)). A photoresist grating of the desired periodicity is fabricated on the $-$Z face of the $LiNbO_3$ substrate using holographic lithography (see Appendix A). Afterwards, the sample undergoes a hard-baking (100 °C and 130 °C in sequence, 30 minutes at each temperature) to progressively improve the adhesion between the photoresist and the substrate surface without seriously deteriorating the photoresist pattern. The sample is then ready for periodical poling. In electric field over-poling, a positive high voltage is applied on the unpatterned +Z face to generate an electric field strength somewhat higher than the coercive field strength of $LiNbO_3$ of ∼21 kV/mm, generally 21.5 - 23 kV/mm. A typical poling characteristic in figure 6.8 shows the applied voltage, the current through the sample and the accumulated charge with respect to the time. The current starts flowing when the applied voltage ramps up to ∼10.5 kV, indicating the onset of domain nucleations. Domain nucleations start on the unpatterned +Z face and grow towards the patterned electrode on the $-$Z face; simultaneously the domains grow laterally and start merging with the neighboring domains. After the inverted domains reach the $-$Z face, they continue merging underneath the photoresist. The key of over-poling is to stop the merging of the neighbouring domains in time when small regions underneath the photoresist remain unpoled. This is achieved by controlling the accumulated charges. The applied voltage is reduced gradually after the accumulated charges reach a value which is higher than the calculated value Q determined from equation (6.1). Empirically we use $2 \times Q$. Therefore, the duty cycle of the periodical domain grating would be slightly larger than 50%. On the contrary to the literature [51], which claims that the over-poling can be done with photoresist gratings on either the +Z or $-$Z face, we observe the successful over-poling only when the photoresist gratings are on the $-$Z face.

QPM structures of periodicities of 1 - 3 μm have been successfully fabricated in $LiNbO_3$ by using this technique. Figure 6.9 presents a PPLN substrate of a periodicity of 1.7 μm fabricated using this method. This sample is etched in HF:HNO_3 solution for a few minutes to reveal the domain patterns. The original $-$Z face (figure 6.9 (a)) shows clearly a periodical pattern without serious degradation of the duty cycle. The micrograph of the original $-$Y face (figure 6.9 (b), cross section) shows clearly how the domains merge laterally. However, the depth of the unpoled area is generally larger than ∼3 μm, significantly deeper than the thickness of the thin film (<1 μm), which is to be fabricated later by the "smart-cut" process. For a sub-micrometer periodicity, the quality of the QPM structure (i.e. homogeneity and duty cycle) is degraded due to the inhomogeneous photoresist pattern and the insufficient thickness of the photoresist grating (see discussion in Appendix A). Figure 6.10 presents images of two areas of an etched original $-$Z face of a PPLN substrate of a periodicity of 800 nm. In figure 6.10 (b), the large area of the surface is homogeneously poled, only some small regions (see the "islands") are periodically poled.

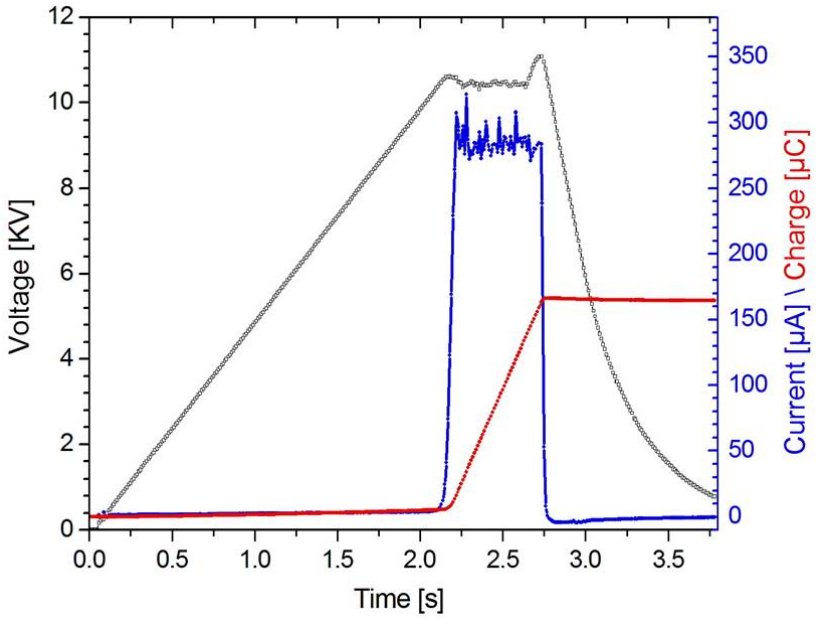

Figure 6.8: A typical characteristic of an electric field over-poling experiment: voltage (black curve), current (blue curve) and charge (red curve) vs. time.

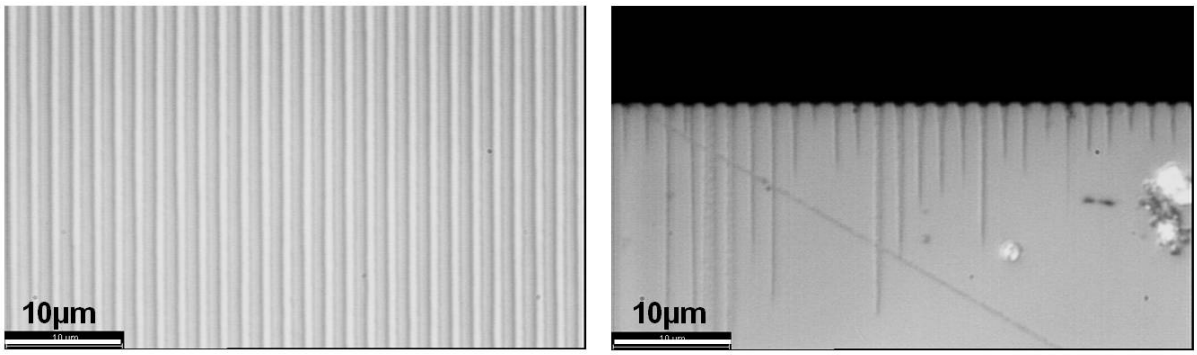

(a) (b)

Figure 6.9: Optical micrographs of a PPLN substrate of a periodicity of 1.7 μm after selective chemical etching: (a) the original $-$Z face and (b) the original $-$Y face.

The fabricated PPLN substrate is carefully cleaned. A small part of the substrate is cut out for the purpose of evaluating the domain pattern. The rest of the substrate is used for fabricating a LNOI thin film as discussed in section 6.1.1. A periodically poled LNOI thin film of a periodicity of 3.2 μm is then fabricated, as shown in figure 6.11. Figure 6.11 (a) shows the original $-$Z face of the small part of the PPLN substrate after selective chemical etching; 6.11 (b) shows the surface of the periodically poled LNOI thin film of the same periodicity.

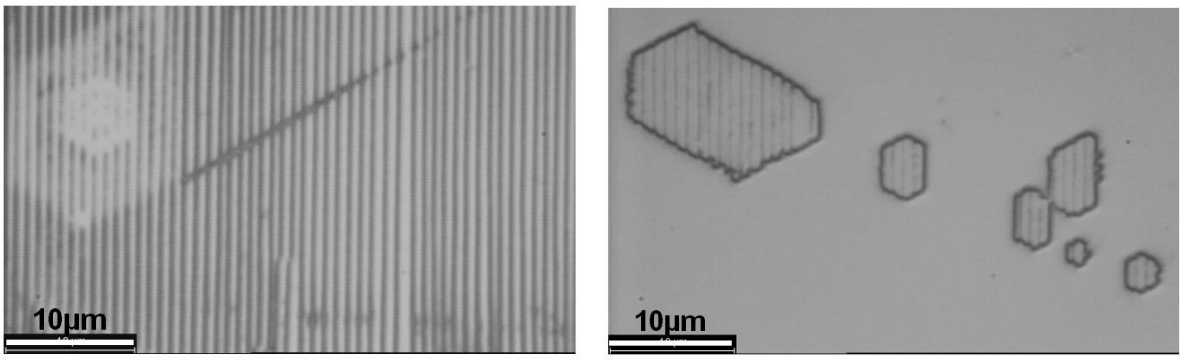

(a) (b)

Figure 6.10: Optical micrographs of two different regions on the original −Z face of a PPLN substrate of a periodicity of 0.8 μm after selective chemical etching.

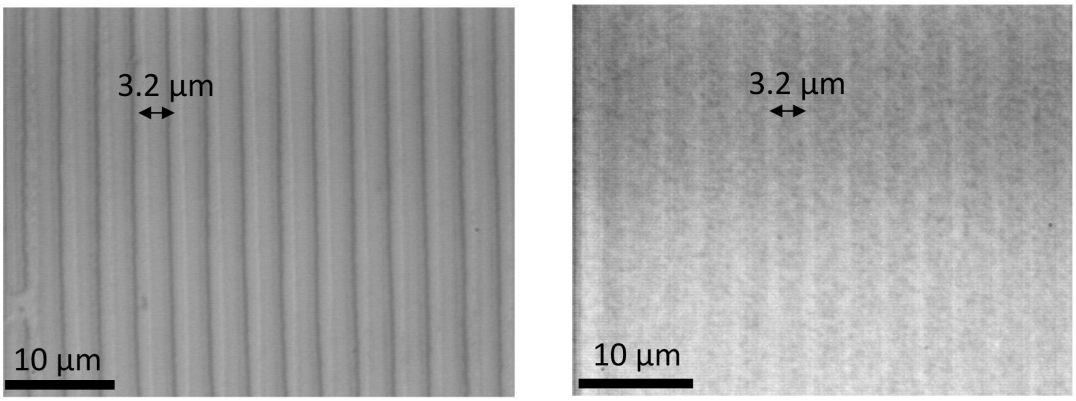

(a) (b)

Figure 6.11: Optical micrographs of (a) a PPLN substrate of a periodicity 3.2 μm and (b) a LNOI thin film of the same periodicity.

6.1.3 Poling of LNOI

The second approach of fabricating a periodically poled LNOI thin film is to directly invert the spontaneous polarization of the LN thin film. To realize it, both surfaces (upper and lower) of the LN thin film must have a direct contact with the elctrodes. This is shown in figure 6.12: a LN thin film is sandwiched between a top electrode and a thin Ti layer as bottom electrode. The top surface of the thin film is the +Z face. The top electrode is fabricated using either photolithography or holographic lithography. A voltage is applied on the top electrode and the bottom Ti layer is connected to the

ground. An electric field of the strength higher than 21 kV/mm is generated between the top and bottom electrodes in order to invert the spontaneous polarization in the $LiNbO_3$ thin film. Because the thickness of the thin film is less than 1 μm, it can be directly poled by applying a very low voltage (a few tens of volts). The great potential of this approach is that a high quality top electrode of a sub-micrometer periodicity can be fabricated using holographic lithography since only a very thin photoresist grating is required. Due to the small thickness of the film, a high contrast electric field can be generated to induce the poling.

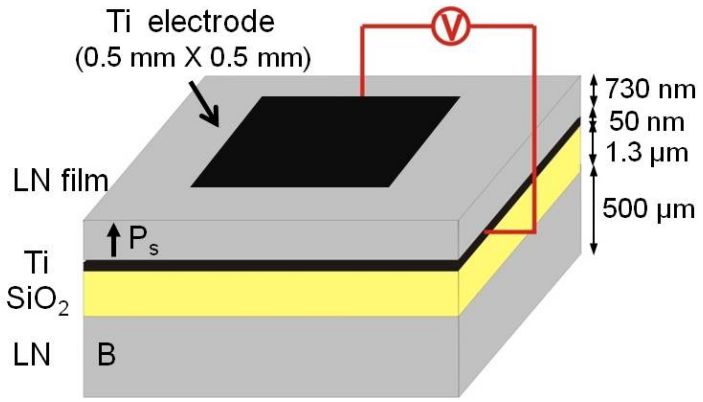

Figure 6.12: A sketch of a LN-Ti-SiO_2-LN structure with a top electrode and poling scheme.

During poling, the applied voltage and the generated current are monitored. Figure 6.13 presents the measured current as a function of the applied voltage. First, a negative voltage is applied to the +Z face of the $LiNbO_3$ thin film. As the electric field has the same direction as the spontaneous polarization, we expect no current flowing. However, with the increase of the voltage, the current starts to rise when the voltage is greater than 50 V and continues increasing exponentially with the increased voltage. When the voltage decreases from the 200 V to 0 V, the current decreases correspondingly. This current we observed in the negative voltage range could be the leakage current. In the positive voltage range, the current appears when the voltage surpasses ~25 V. This voltage is ~60 percent higher than ~16 V calculated from the coercive field of bulk $LiNbO_3$ of ~21 kV/mm. This might be due to the partial oxidation of the Ti layer beneath $LiNbO_3$ thin film during annealing. The oxidation results in an TiO_2 layer beneath the $LiNbO_3$ thin film. Since TiO_2 is a dielectric material, the extra voltage required for poling compensates the voltage drop in this layer. Another possible explanation is that the coercive field of $LiNbO_3$ thin film becomes higher than that of the bulk $LiNbO_3$ during the fabrication processes, for example, due to Li^+ out-diffusion during annealing. After this current appears, the material shows an ohmic behavior (see the following discussion). We suspect that the observed current is not entirely induced by the domain inversion, because it is higher than the expected current by an order of magnitude.

Figure 6.14 shows, as an example, the poling characteristic of inverting the sponta-

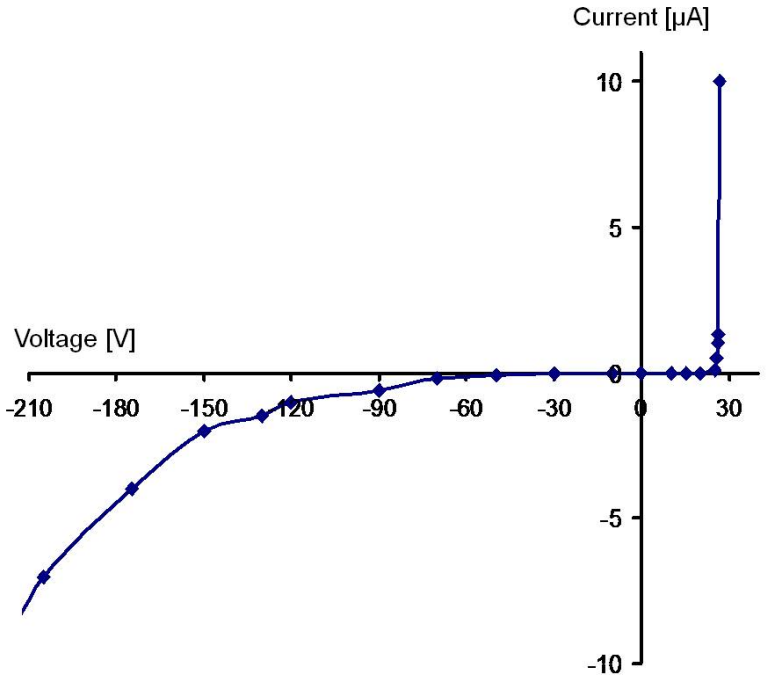

Figure 6.13: The induced current as a function of the applied voltage.

neous polarization of such a thin film. According to the progression of the current, the poling characteristic can be divided into four different regions. In region I, a current of $\sim$0.8 μA appears during the ramping of the applied voltage due to the dielectric property of $LiNbO_3$. The structure of a thin layer of $LiNbO_3$ sandwiched between top and bottom electrodes essentially functions as a capacitor. Given the area of the electrodes and the thickness of the film, the calculated capacitance of the structure used in this experiment is $\sim$100 pF. Theoretically this results in a charging current of 0.5 μA when the voltage ramps up at a rate of 5 kV/s. In region II, the voltage on the sample is kept constant and there is no detectable current. In region III, a current up to 3.5 μA appears. The voltage in this region decreases because of the voltage drop on the series resistor (see figure 3.9). It is worth to point out that, at which moment this current appears is rather unpredictable. It varies randomly from sample to sample. The voltage is ramped down gradually to 0 V in region IV. The ohmic behavior in this region indicates that the crystal might be damaged due to dielectric breakdown. Therefore, the current observed in region III might be the leakage current induced from dielectric breakdown and not the charge migration induced from poling. This leads to the difficulty of controlling the progress of the domain inversion.

The poling is first done with a homogeneous top electrode as shown in figure 6.12. The top electrode is fabricated using the lift-off technique (see section 3.2). Domain inversion is observed after the sample has been selectively etched. Figure 6.15 presents the domain inversion in two different samples. The domain inverted area appears as a cluster of small triangle regions. This is surprising since it is well known that $LiNbO_3$ do-

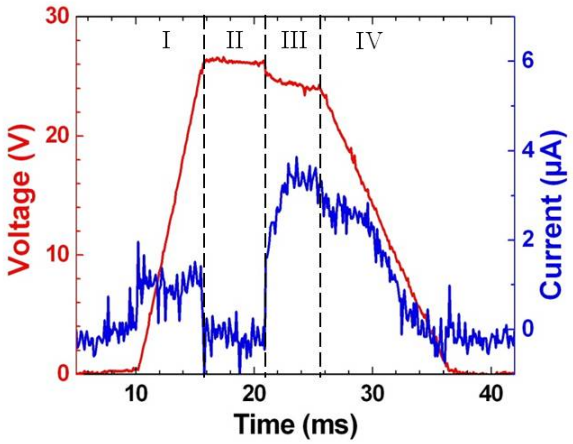

Figure 6.14: The poling characteristic during the voltage pulse of 26 V: the applied voltage and measured current vs. time.

mains on the +Z face have a hexagon shape. Because the domain inverted area is much smaller than the electrode covered area, we speculate that the domain inversion proceeded for a short time but was automatically terminated after the dielectric breakdown set in. A similar experiment is done with a grating top electrode as shown in figure 6.16 (a). Domain inversion is observed in a small region which contains a few grating fingers and part of the connecting strip as shown in figure 6.16 (b).

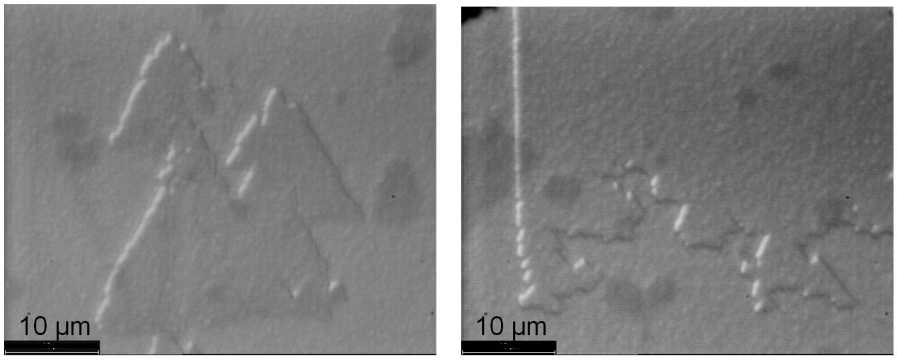

(a) (b)

Figure 6.15: Optical micrographs of the surfaces of poled LN thin films after selective chemical etching.

After poling is completed, the metallic Ti layer beneath the LN film has to be oxidized to TiO_2 in order to avoid absorption losses. This can be done by a high temperature annealing for many hours until the film becomes transparent. A preliminary experiment of annealing the sample for 6 hours at 450 °C and 600 °C subsequently increases the transmission of the sample from 10% to 40%, indicating partial oxidation of the metallic Ti layer. The optimum annealing parameters are under investigation.

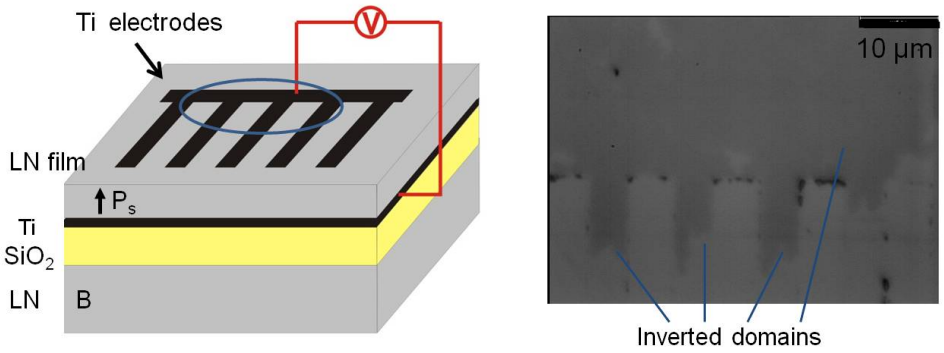

(a) (b)

Figure 6.16: (a) Scheme of periodical poling of a LNOI thin film. (b) Optical micrographs of the domain inverted area after selective chemical etching. The circle in (a) indicates how the domain inverted region is corresponding to the electrode pattern.

6.2 PPLNOI photonic wires

Fabricating photonic wires in a PPLNOI platform and the first experimental results of investigating nonlinear interactions in PPLNOI photonic wires are presented and discussed in this section. This part of work is done in collaboration with Hu.

6.2.1 Fabrication and optical properties

PPLNOI photonic wires are fabricated by plasma etching a PPLNOI thin film. According to our experience in Ar milling, the rates of milling a +Z face and a −Z face of $LiNbO_3$ are the same. Photoresist (OIR 907-17) stripes of 1.7 μm thickness and 1 - 7 μm width are used as etch mask, defined by photolithography. The sample was etched by Ar milling for 60 min in a Plasma100 system (Oxford Instruments). The etching rate is ∼10 nm per minute. Figure 6.17 (a) shows a SEM micrograph of a photonic wire of 1 μm top width and ∼730 nm height; figure 6.17 (b) is a sketch of the cross section of this wire. The dark stripe underneath is the SiO_2 cladding. The side walls of the wire have a slope of ∼27°. Figure 6.18 presents the top views of the fabricated PPLNOI photonic wires of 9 μm and 3.2 μm periodicity, respectively, observed using an optical microscope.

The optical mode distribution and the propagation loss are measured using the methods discussed in section 4.1. The experimental setups are similar to the ones shown in figures 4.1 and 4.2 with a certain modification in order to couple the light in and out of the photonic wire efficiently. The objective lens used for coupling the light into the

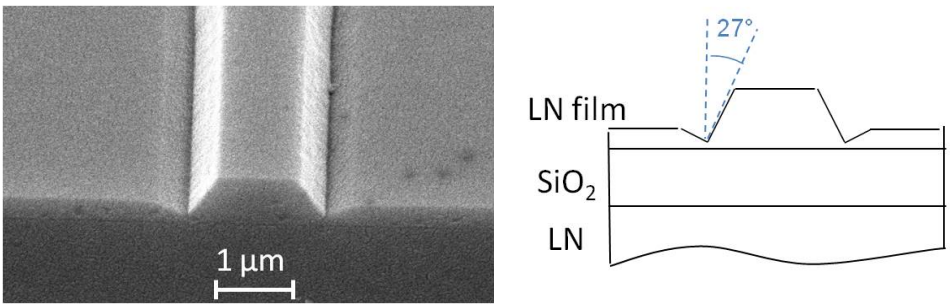

(a) (b)

Figure 6.17: (a) SEM micrograph of a LNOI photonic wire of 1 μm top width taken from [3]. (b) A sketch of the cross section of the photonic wire.

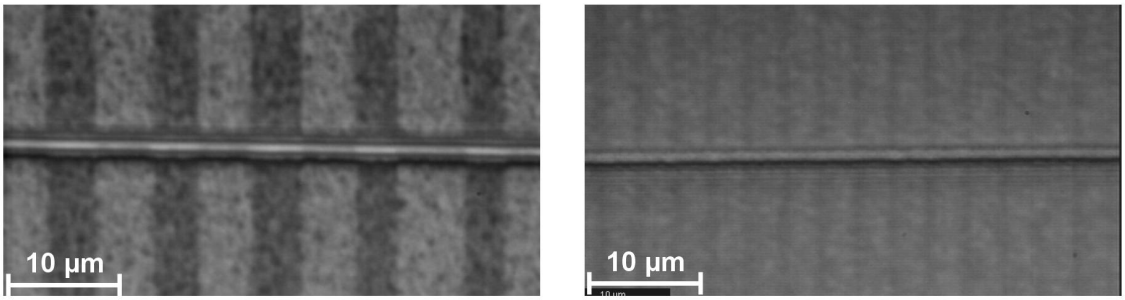

Figure 6.18: Optical micrographs of PPLNOI photonic wires of 1 μm width and a periodicity of (a) 9 μm and (b) 3.2 μm.

wire has a 60X magnification (NA: 0.8). An objective lens of a 100X magnification (NA: 0.9) is used to magnify the near field distribution of the guided mode. Figure 6.19 shows the measured (6.19 (a)) and calculated (6.19 (b)) distribution of the fundamental TM mode in a photonic wire of 1 μm top width. The measured propagation losses of the TM mode and TE mode are 9.9 dB/cm and 12.9 dB/cm, respectively.

The effective refractive indices n_{eff} of the photonic wire at different wavelengths are required to determine the periodicity of the domain structures for nonlinear interactions. Due to the high index contrast of the photonic wires and their small cross section dimensions, n_{eff} of the wire varies considerably as function of the wavelength between the bulk index of LN and that of SiO_2. n_{eff} for a fundamental mode of TM polarization in the photonic wire discussed above was calculated as function of wavelength using a FDTD solver (Lumerical Inc.), as shown in figure 6.20. The group index n_g is measured using the method described in [52, 53, 54]. The measured and calcuated group indices as shown in figure 6.20 are in good agreement.

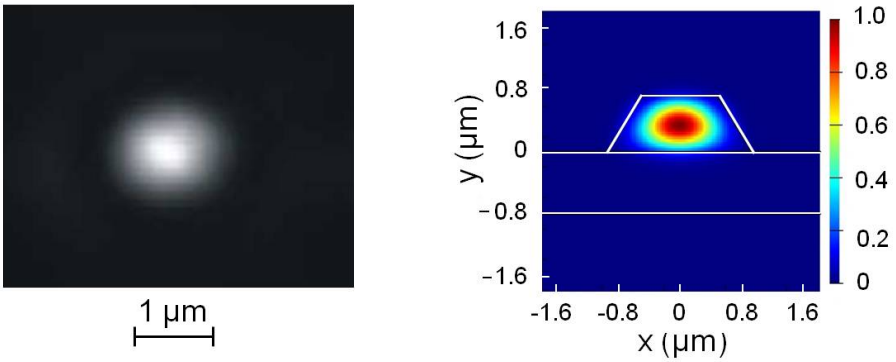

(a) (b)

Figure 6.19: Measured (a) and calculated (b) intensity distribution of the fundamental TE mode in a photonic wire of 1 μm top width and 730 nm height, taken from [3].

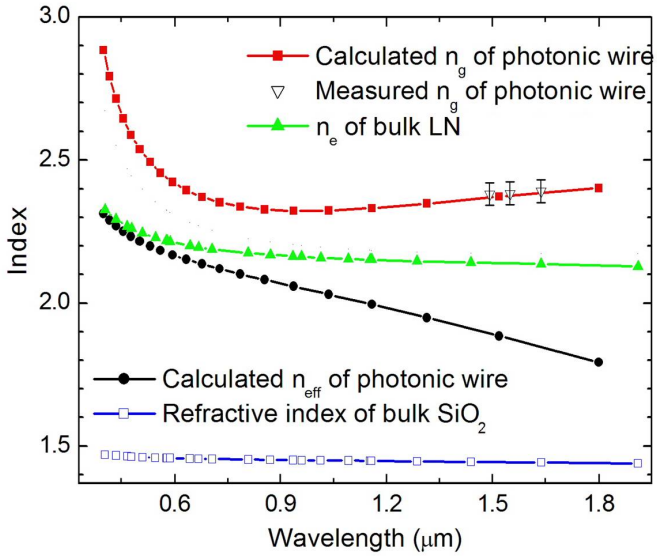

Figure 6.20: Calculated effective indices n_{eff}, calculated and measured group indices n_g for the fundamental mode of TM polarization in a photonic wire of 1 μm top width versus the wavelength. The refractive indices of bulk $LiNbO_3$ and SiO_2 are displayed for comparison. This graph is taken from [3].

6.2.2 Nonlinear interactions in PPLNOI photonic wires

As shown in figure 6.20, the effective index of the photonic wire is significantly different than the index of bulk $LiNbO_3$. Therefore, the periodicity of a QPM structure required for a nonlinear interaction is also significantly different. Figure 6.21 presents the calcu-

lated periodicities of a QPM structure in a photonic wire required for 1st order type-0 SHG in which fundamental and SH waves are of TM polarization. It is called 1st order because the 1st harmonic term of the periodically modulated $d(z)$ contributes to the nonlinear interaction, i.e. m=1 in equation 2.26. The periodicities are calculated for photonic wires of a height of 730 nm and a width of 1 μm and 7 μm respectively. Only the nonlinear interaction between TM_{00} mode of the fundamental wave and TM_{00} mode of the SH wave is considered. Due to the small size of the photonic wire, the effective index of the optical mode in the photonic wire varies significantly in wires of different geometric dimensions. Therefore, a slight deviation of the periodicity of the periodical domains will induce a large shift of the phase matching wavelength. For a fundamental wavelength of 1064 nm, a QPM structure of 3 μm periodicity is required in a photonic wire of 1 μm width, while a 3.3 μm periodicity is required in a photonic wire of 7μm width.

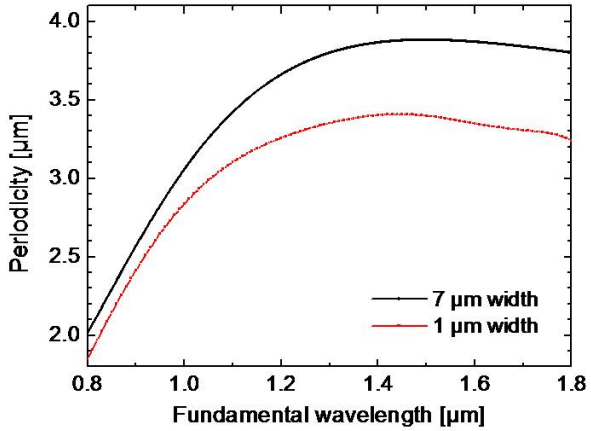

Figure 6.21: Periodicity of the QPM structure for 1st order SHG in photonic wires of a height of 730 nm and a width of 1 μm (red curve) and 7 μm (black curve) as function of fundamental wavelength. Fundamental and SH waves are in TM polarization.

Wavelength-tuning curves of SHG in periodically poled photonic wires of different lengths and periodicities are calculated and shown in figure 6.22 as examples. The photonic wires have a height of 730 nm and a width of 7 μm. The calculations are based on the assumption of lossless waveguides and no pump depletion. For an interaction length of 1.5 mm (i.e. the length of the periodically poled section), the phase matching wavelength in a photonic wire of 3.2 μm shifts by 24 nm towards the shorter wavelength compared to that in a photonic wire of 3.3 μm periodicity. The bandwidth of the wavelength tuning is 1.6 nm. SHG in a photonic wire of 0.1 mm interaction length and 3.2 μm periodicity has a lower efficiency, however, a broader bandwidth of 24 nm due to the short interaction length (see discussions in section 2.3).

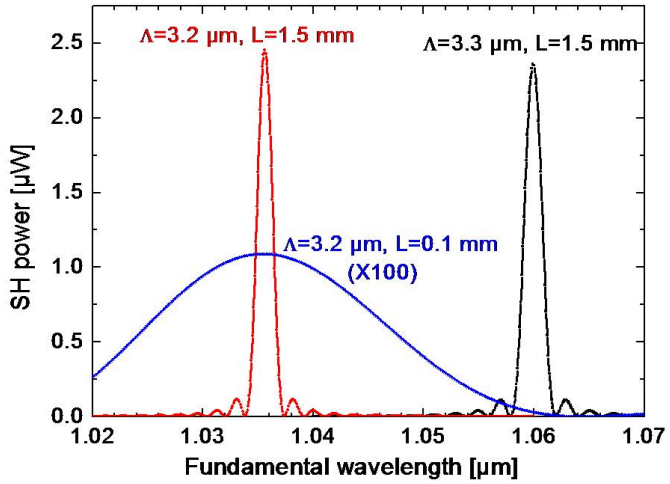

Figure 6.22: Calculated wavelength-tuning curves of SHG in a photonic wire of a height of 730 nm and a width of 7μm: Generated SH power as function of fundamental wavelength. Input pump power is 1 mW. The periodicity and the interaction length of the photonic wire are 3.2 μm and 1.5 mm (red curve), 3.3 μm and 1.5 mm (black curve), and 3.2 μm and 0.1 mm (blue curve, 100 times of the actual values) respectively.

SHG in a photonic wire of 9 μm periodicity

In the first attempt to demonstrate nonlinear interactions in photonic wires, a periodically poled LNOI photonic wire of 730 nm height, 1 μm width and 9 μm periodicity is used. The periodically poled sections is $\sim$100 μm long.

As discussed above, the 1st order SHG in such a photonic wire requires a periodicity of 3 μm; 9 μm periodical domains enable 3rd order SHG (i.e. m=3 in equation 2.26). The fundamental wave is provided by a diode laser at a wavelength of 1064 nm. A photomultiplier tube which is sensitive in the wavelength range of 300 - 650 nm is used to measure the generated SH power. The dependence of the generated SH power on the input fundamental power is shown in figure 6.23 (a); a parabolic dependence is observed. The mode distributions of the fundamental and SH modes are measured as shown in figure 6.23 (b) and (c) respectively.

SHG in a photonic wire of 3.2 μm periodicity

1st order SHG is demonstrated in a periodically poled photonic wire of 730 nm height, 7 μm width, 3.2 μm periodicity and 1.5 mm interaction length. As it is discussed in figure 6.22, the fundamental wavelength of 1064 nm is far outside the tuning range where efficient SHG can take place. Nevertheless, SHG is observed and the optical modes and

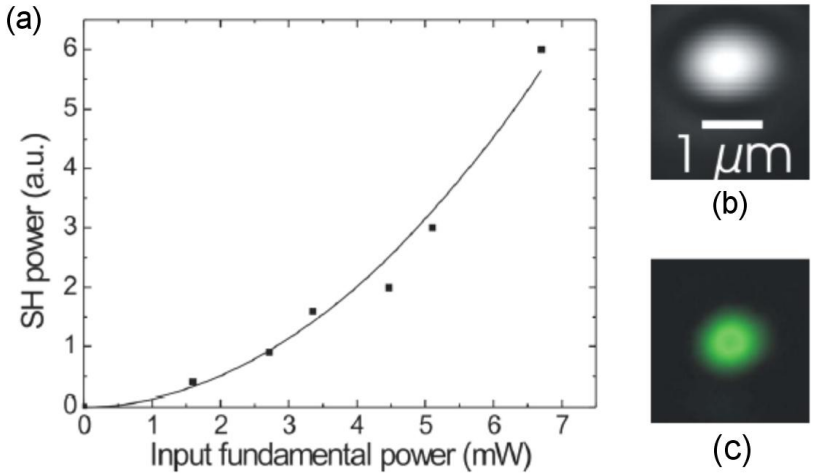

Figure 6.23: (a) Measured (dots) and fitted (line) SH power versus input fundamental power (measured in front of the coupling lens) in a PPLN photonic wire of 1 μm top width and 9 μm periodicity. Measured mode distributions at (b) fundamental and (c) SH wavelengths. This graph is taken from [4].

the powers of fundamental wave and generated SH wave are measured as shown in figure 6.24. A parabolic dependence of the generated SH power versus the fundamental power is observed. The mode distributions of the fundamental and SH modes, however, appear as overlappings of multiple optical modes.

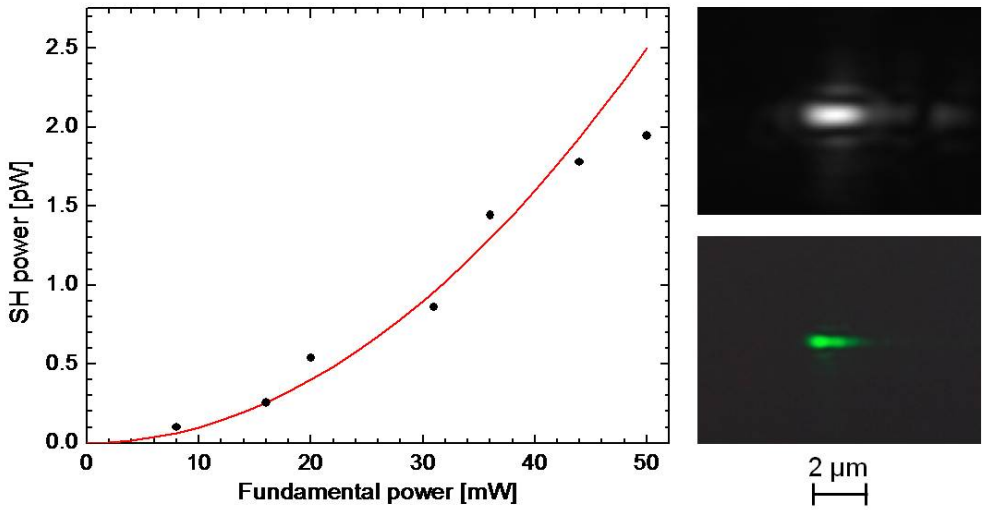

Figure 6.24: (Measured (dots) and fitted (line) SH power versus input fundamental power (measured in front of the coupling lens) in a PPLN photonic wire of 7 μm top width and 3.2 μm periodicity. Measured mode distributions at (b) fundamental and (c) SH wavelengths.

6.3 Summary

In this chapter, the recent progress of fabricating a periodically poled LNOI thin film and photonic wire and nonlinear interactions in such photonic wires are presented.

A LNOI thin film is fabricated using ion-slicing and crystal bonding (i.e. "smart-cut") technique. A high energy ion-implantation leaves a damaged layer $\sim$1 μm beneath the crystal surface. After carefully designed bonding and annealing steps, a thin layer of $LiNbO_3$ is left on top of a SiO_2-on-$LiNbO_3$ substrate, resulting in a $LiNbO_3$-on-Insulator thin film structure. A photonic wire is then fabricated by using ICP etching. The photonic wire has a high refractive index contrast with respect to the surrounding media and typical sub-micrometer dimensions (1 μm$\times$ 730 nm in this work). This gives rise to an enhanced light confinement and enables a reduced bending radius; therefore, it is a very promising material platform enabling an ultra-dense optical integration and highly efficient nonlinear interactions.

To enable efficient nonlinear interactions in a LNOI photonic wire, QPM structures of a suitable periodicity are required. Two methods are investigated to fabricate a periodically poled LNOI thin film. The first method is to directly bond an ion-implanted PPLN substrate onto a SiO_2-on-$LiNbO_3$ substrate. The PPLN substrates are fabricated using either conventional lithography and electric field poling (for a periodicity typically $\geq$4 μm) or holographic lithography (for a smaller periodicity) and electric field over-poling. Periodically poled LNOI thin films of a periodicity of 9 μm and 3.2 μm are successfully fabricated. The second method is to add a metal layer between the $LiNbO_3$ thin film and the SiO_2 layer serving as a bottom electrode, then to directly invert the spontaneous polarization of the $LiNbO_3$ thin film by applying an electric field between the lithographically defined top electrode and the bottom electrode. Domain inversion has been observed on the $LiNbO_3$ thin films; however, due to a dielectric breakdown, the electrode covered regions were not completely poled. The challenge of this method is to avoid dielectric breakdown during poling. This includes developing methods to recover the crystal defects induced by ion implantation, and improving the quality of the top and bottom electrodes as well as the contact between $LiNbO_3$ and the electrode material.

1st and 3rd order nonlinear interactions including SHG and SFG are demonstrated in periodically poled photonic wires of different parameters. Fof SHG in photonic wires of 3.2 μm and 9 μm periodicity, the parabolic dependences of the generated SH power vs. the fundamental power are observed and the mode distributions of both waves are measured. The low conversion efficiency is due to several factors including a high waveguide loss, a short interaction length and an unsuitable domain period. Further work is to improve the quality of the photonic wire and QPM structures as well as to precisely define the domain period.

Chapter 7

Conclusions and Outlook

7.1 Conclusions

The motivation of this research is to develop $LiNbO_3$ integrated nonlinear optical devices which have an enhanced nonlinear efficiency and enable nonlinear interactions such as counter-propagating nonlinear interactions. Novel $LiNbO_3$ waveguides of an enhanced light confinement and QPM structures are essential for developing such a device. We focused our efforts on two promising types of such waveguides: PPLN ridge waveguides and LNOI photonic wires. The technologies of fabricating periodically poled ridge waveguides and photonic wires are developed and nonlinear interactions in the waveguides are investigated. The main accomplishments are summarized in the following.

PPLN ridge waveguides on X(Y)-cut $LiNbO_3$ substrates

Ridge waveguides on a X-cut $LiNbO_3$ substrate are fabricated using conventional lithography and plasma etching followed by Ti in-diffusion. Electric field assisted local periodical poling is then applied. An electric field is applied in the body of the ridge to periodically reverse the spontaneous polarization of the crystal. Compared to the domain inversion of a bulk $LiNbO_3$ substrate, a very low voltage of a few hundred volts is sufficient for local periodical poling.

Single mode transmission at 1550 nm wavelength is observed in the ridge guides of a top width of 5 - 8 μm. The propagation losses in the ridge guides decrease with the increase of the top width. Ridge guides, which have been used in this work to demonstrate nonlinear interactions, have propagation losses of 0.7 - 1.2 dB/cm in TE polarization. The mode sizes of the ridge guide are evidently smaller than that of the conventional channel waveguide, typically $\sim$4 μm in the horizontal direction and $\sim$3 μm in the vertical direction in TE polarization. Ferroelectric domains are characterized by two different methods: selective chemical etching and nonlinear CLSM imaging. Selective chemical etching reveals that a successful poling in the ridge on X-cut $LiNbO_3$ induces a hexagonal domain shape which agrees with the common knowledge of $LiNbO_3$ ferroelectric domains. The inverted domain is as deep as up to $\sim$5 μm, sufficient to overlap the transmitted mode inside the ridge guide. The duty cycle of the periodic domains can

be controlled by optimizing the duty cycle of the comb-like electrodes together with the duration and voltage of the voltage pulse(s) applied during poling.

Nonlinear interactions are investigated using periodically poled Ti in-diffused ridge waveguides on X-cut $LiNbO_3$ at room temperature. A normalized SHG conversion efficiency of 16.5 % $W^{-1}cm^{-2}$ is obtained at a fundamental wavelength of ∼1550 nm. It is 50 % higher than that in a Ti in-diffused conventional channel waveguide. A stable SH power up to ∼50 mW is generated at room temperature. Wavelength conversion using a cascaded SHG/DFG scheme is also demonstrated using such a ridge waveguide. A conversion efficiency of −29 dB from a signal wave to an idler wave is measured when ∼200 mW fundamental power is coupled. Good stability of both the generated SH wave in SHG and the idler wave in cascaded SHG/DFG at room temperature shows that the Ti in-diffused ridge waveguides on X-cut $LiNbO_3$ are much less sensitive to the photorefractive effects compared to Ti in-diffused $LiNbO_3$ channel waveguides.

Periodically poled LNOI photonic wires

A LNOI thin film is fabricated using ion-slicing and crystal-bonding ("smart-cut") technique. Photonic wires are fabricated in a LNOI thin film by using plasma etching. LNOI photonic wires have a high refractive index contrast with respect to the surrounding media and typical sub-micrometer dimensions (1 μm× 730 nm in this work). The propagation losses in a photonic wire of 1 μm width and 0.7 μm height are 9.9 dB/cm and 12.9 dB/cm in TM and TE polarization, respectively.

In order to explore nonlinear interactions in LNOI photonic wires, periodical domain structures in the wires are required. Two different approaches are developed in this work. In the first approach, an ion-implanted PPLN wafer is bonded onto a SiO_2-on-$LiNbO_3$ substrate. The PPLN wafers are fabricated using either conventional lithography and electric field poling (for a periodicity typically ≥4 μm) or holographic lithography and electric field over-poling (for a smaller periodicity), respectively. Periodically poled LNOI thin films of a periodicity of 9 μm and 3.2 μm are successfully fabricated. In the second approach, a thin layer of Ti is deposited between the $LiNbO_3$ thin film and the SiO_2 layer serving as a bottom electrode. Electric field assisted poling is then applied directly to the $LiNbO_3$ thin film by applying an electric field between the lithographically defined top electrode and the bottom electrode. Triangular inverted domains are observed on the $LiNbO_3$ thin films after selective chemical etching.

1st and 3rd order SHG are investigated in PPLNOI photonic wires of 3.2 μm and 9 μm periodicity, respectively. The photonic wires are fabricated using the first approach of direct bonding of PPLN. A parabolic dependence of the generated SH power vs. the fundamental power is observed. However, the conversion efficiency is low due to high propagation losses, short interaction length and an unsuitable domain periodicity.

7.2 Outlook

Despite the accomplishments of this research, the great potentials of $LiNbO_3$ ridge type waveguides especially of LNOI photonic wires are not yet fully demonstrated. Efforts must be continued in optimizing the fabrication techniques to enhance the nonlinear efficiency to a higher level, and investigating new techniques of fabricating high quality QPM structures of sub-micrometer periodicity. These not only increase the nonlinear efficiency tremendously, but also enable a broad range of interactions such as counter-propagating interactions. Therefore, highly efficient, ultra-compact and versatile integrated nonlinear optical devices can be realized.

PPLN ridge waveguides on X(Y)-cut $LiNbO_3$ substrates

The normalized conversion efficiency of SHG in a Ti in-diffused ridge waveguide (16.5 % $W^{-1}cm^{-2}$) is significantly lower than the theoretically predicted value (36 % $W^{-1}cm^{-2}$). A further improvement of the conversion efficiency can be achieved by optimizing the dimensions of the ridge and the duty cycle of the periodical domains. For example, the nonlinear cross section S_{eff} of the ridge guides in this work is ∼40 μm^2. This value can be reduced to 30 μm^2 by using a Ti in-diffused ridge guide of 5 μm width (Ti thickness: 100 nm). The duty cycle of the periodical domains can be improved by improving the electrode quality, mainly the contact between the electrode material and the crystal and the symmetry of the counter electrodes with respect to the centerline of the ridge. We are confident that by improving these two aspects, a conversion efficiceny close to the theoretical prediction can be achieved.

Another attractive property of such a ridge guide is its lower susceptibility to the photorefractive effects. It enables room temperature operation of high power nonlinear interaction which generally is achieved by using expensive doped $LiNbO_3$ crystals (MgO:$LiNbO_3$ or ZnO:$LiNbO_3$). The characterization of SHG and cSHG/DFG at a high pump power level in a long ridge waveguide is to be studied in more detail. Besides SHG and cSHG/DFG, nonlinear interactions such as sum-frequency-generation (SFG), optical-parametric-scillation (OPO), can also be realized in a Ti in-diffused ridge guide. Packaged devieces can be designed without a complicated temperature control system as well as other complications introduced by high temperature operation.

Periodically poled LNOI photonic wires

LNOI photonic wires have a high refractive index contrast as discussed. This enables also a small bending radius (∼10 μm), which facilitates a high density integration of multiple functions in such a platform. Concerning nonlinear interactions, the high index contrast and the small cross section of the waveguide result in an extremely small mode size and excellent overlap between different modes, leading to an extremely high nonlinear efficiency in theory.

However, the fabricated photonic wires typically have high propagation losses ($\geq$ ∼10 dB/cm) and short interactions lengths (a few milimeters). This limits the nonlinear

efficiency significantly. Possible solutions are to improve the quality of the crystal-bonding (i.e. cleanliness of the bonding surfaces, low pin-hole deposition of SiO_2, etc.) and to reduce the surface roughness by the means of polishing and well controlled plasma etching.

In terms of fabricating periodically poled photonic wires, challenges exist in both approaches. In the 1st approach of direct bonding a PPLN substrate, the quality of the resulting photonic wire is mainly limited by the quality of crystal-bonding. For an efficient nonlinear interaction to take place, one has to precisely define the domain periodicity. This is especially critical in photonic wires because the required periodicity varies significantly with respect to the geometric dimensions of the waveguides. For this purpose, a computer controlled goniometer with a precise angle control is required in Lloyd holography setup. Another challenge is to fabricate high quality sub-micrometer periodical domain structures in a bulk $LiNbO_3$ substrate because a high contrast of the electric field strength between the electrode covered region and uncovered region is difficult to achieve using photoresist gratings. One proposal is to use SiO_2 gratings instead of photoresist gratings as the poling mask in over-poling [55]. It is highly promising that a high nonlinear efficiency close to the theoretical prediction can be achieved by improving the quality of both photonic wire and domain structures.

In the 2nd approach of directly inverting the spontaneous polarization of a $LiNbO_3$ thin film, the main challenge is to prevent the material from dielectric breakdown which inhibits the lateral progression of the domain inversion. We suspect that such a dielectric breakdown took place in the defect sites in the crystal. It is known that high energy ion-implantation tends to induce such defects into the material. The possible solution is to recover the crystal defects induced by ion-implantation as much as possible. Meanwhile, improving the quality of the top and bottom electrodes as well as the contact between $LiNbO_3$ and the electrode material enables domain nucleation to take place homogeneously under the electrode, therefore, domain inversion in a larger area can be realized. Moreover, using this approach, a high quality top electrode of a sub-micrometer periodicity can be fabricated using holographic lithography since only a very thin layer of photoresist grating is required. Due to the sub-micrometer thickness of the film, a high contrast electric field can be generated to induce the poling. Therefore, a $LiNbO_3$ waveguide of a submicron periodicity can be finally realized. This will enable a new class of nonlinear processes: counter-propagating nonlinear interactions as, for example, in a mirrorless optical parametric oscillator (OPO).

Although the concept of a mirrorless OPO using the QPM technique was proposed first in 1996 [56], it was not experimentally demonstrated until 2007 by Canalias et. al. [57] in a bulk PPKTP crystal. Fabricating a mirrorless OPO in a $LiNbO_3$ waveguide poses much higher challenges compared to in a bulk PPKTP crystal, mainly due to the difficulties of fabricating high quality submicron periodical domain structures in $LiNbO_3$ as previously discussed. Nevertheless, we would like to point out the advantages of such a device to encourage upcoming research in this area. Taking an OPO for the mid infrared spectral range (2.5 μm - 3.5 μm) as an example, the momentum conservation conditions and tuning characteristics of the counter-propagating (mirrorless) and conventional co-propagating OPOs are compared theoretically in figure 7.1.

The OPO is pumped at a wavelength around 1.55 μm. This allows the use of available high performance pump sources (DFB-lasers, tunable extended cavity semiconductor lasers, Erbium-doped fiber amplifiers). The required domain periodicity for the 1st order counter-propagating interaction is ~720 nm. In a counter-propagating scheme, the signal and idler waves propagate in opposite directions. This puts much stronger constraints on the momentum mismatch and gives rise to a special tuning behavior of the counter-propagating idler wave [57]. The bandwidth of the idler wave (red curve) is two orders of magnitude narrower than that of the co-propagating OPO, leading to possibilities of tuning a narrowband mid-infrared idler wave with high precision. This feature is of special interest also in quantum information processing using, for example, parametric down-conversion [37]. The other unique feature of the counter-propagating interaction is the inherent feedback of the idler wave, which means, no alignment, external mirrors or surface coatings are required to reflect the beam, hence, "mirrorless". This will simplify an OPO system design and enhance the stability of the device significantly.

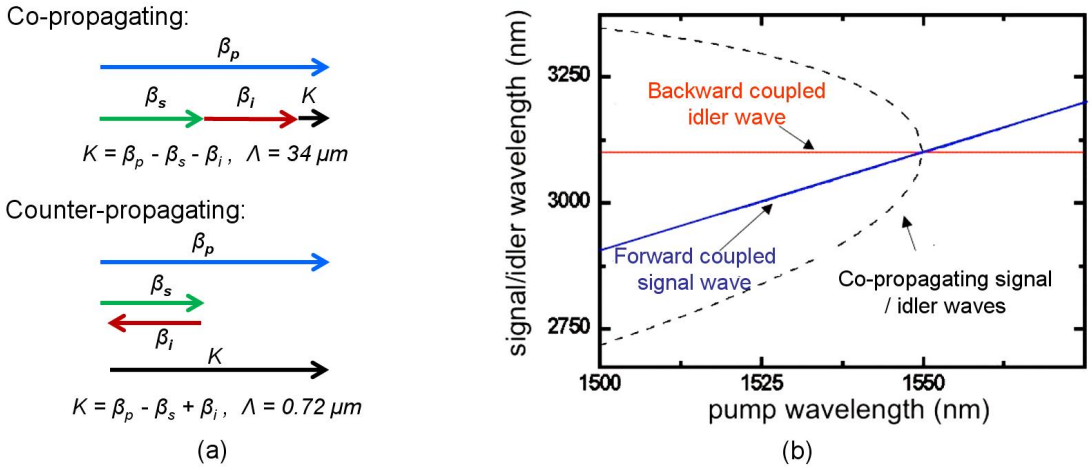

Figure 7.1: (a) Schemes of an OPO : co-propagating and counter-propagating. β: propagation constant; K: wave vector associated to periodical domain structures; Λ: periodicity of the domain tructures. (b) Calculated tuning characteristics for counter-propagating and conventional co-propagating OPOs. The red and blue curves represent the backward coupled idler wave and the forward coupled signal wave in the counter-propagating OPO; The black dashed curve represents the signal/idler wave in the co-propagating OPO.

In this thesis, we developed different techniques such as local poling, electric field over-poling assisted with holographic lithography, which are promising to achieve a small periodicity. Moreover, our ongoing progress in LNOI thin films certainly opens a new chapter of submicron domain engineering with great promises. We believe that, with further optimized techniques, high efficiency nonlinear interactions as well as counter-propagating interactions in a $LiNbO_3$ waveguide (photonic wire) can become a reality.

Appendix A

Holographic lithography

A simple Lloyd interferometric optical holography setup is used to fabricate submicron photoresist gratings on glass and $LiNbO_3$ substrates. The experimental setup and its schematic structure are shown in figure A.1 (a) and (b), respectively. An Ar-Ion laser (Innova 90C-6, Coherent Inc.) is used to provide a laser beam of an output power up to 2 W at $\lambda = 488nm$. Before the beam reaches the sample, it is expanded and collimated using Keplerian telescope scheme, which consists of a focal lens and a collimating lens. The rear focal point of the focal lens coincides with the front focal point of the collimating lens. A pinhole ($\phi = 8\mu m$) as a spatial filter is placed at the mutual focal point of these two lenses to remove aberrations in the beam. A rectangular aperture (20 mm X 5 mm) is placed behind the collimating lens to form a rectangular beam. The average intensity of the rectangular beam is in the range of 100 - 300 mW/cm^2.

The interference fringe pattern required for grating fabrication is generated using a Lloyd-type interferometer as shown in figure A.2 ((a) schematic diagram and (b) photograph of the experimental setup). The mirror and the sample holder are mounted on a rotational sample stage, and the mirror is oriented perpendicular to the surface of the sample. The sample stage is adjusted with respect to the laser beam such that the lower half of the beam reaches the sample directly and the upper half of the beam is reflected by a mirror and then reaches the sample. Due to the reflection, the phases of the wavefronts of the upper half of the beam changes slightly with respect to the lower half. As a result, when the directly incident beam and the reflected beam meet on the surface of the sample, the constructive and distructive interferences create a sinusoidal intensity pattern of a peiodicity Λ. By rotating the sample stage, we can easily change the incident angle of the laser beam onto the sample and thus the periodicity Λ of the interference patterns, which is determined by:

$$\Lambda = \frac{\lambda}{2\sin\theta}, \tag{A.1}$$

where λ is the wavelength of the laser beam, θ is the incident angle to the sample.

Figure A.3 explains how the sinusoidal intensity pattern of the illumination (figure A.3 (a) and (b)) is transferred to a photoresist grating of a rectangular profile (figure A.3 (c)). This works due to a nonlinear behavior of the developing rate of the photoresist in a diluted solvent with respect to the illumination intensity. There exists such a threshold

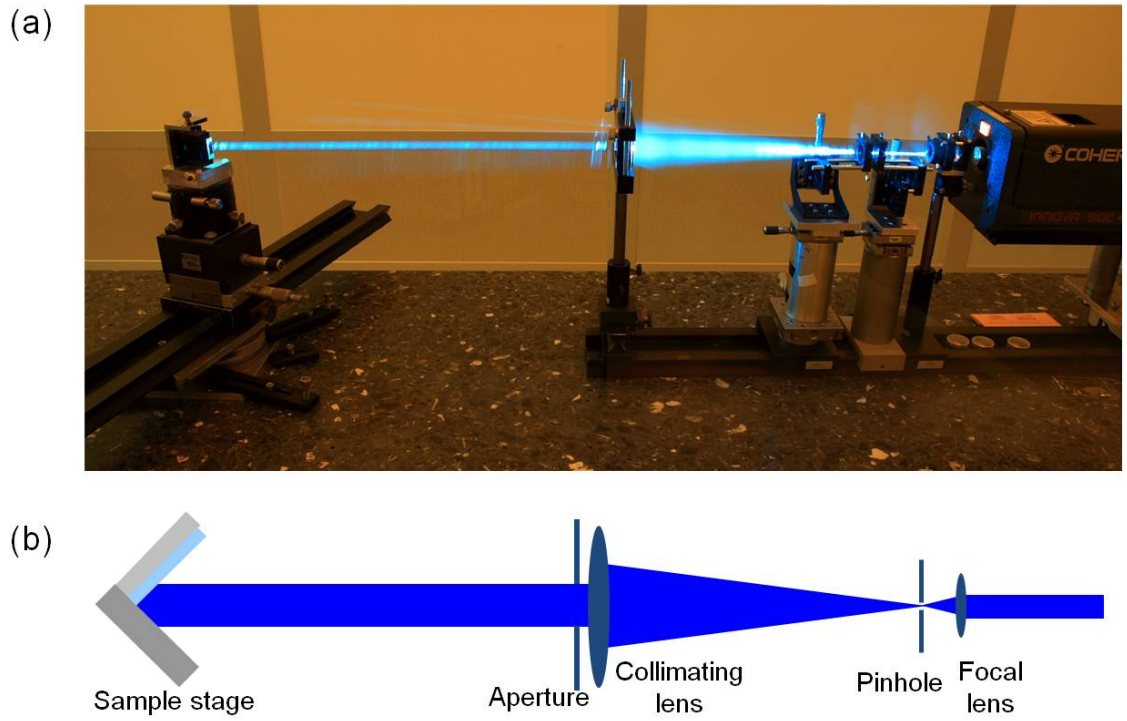

Figure A.1: Lloyd interferometric optical holography setup: (a) photograph of the setup and (b) schetch.

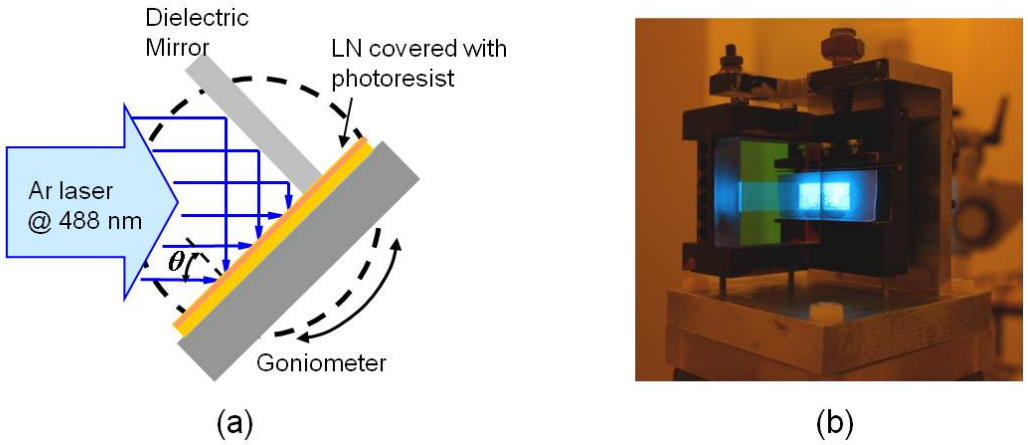

Figure A.2: Lloyd interferometer: (a) schematic diagram and (b)photograph of the sample stage.

intensity, below which the illuminated photoresist can not be developed in the solvent. As a consequence, the photoresist, which is illuminated with the intensity below the threshold will remain after developing; hence, a rectangular profile of the photoresist grating is obtained as shown in figure A.3 (c). The threshold intensity depends on the chemical composition of the photoresist and the concentration of the developing solvent.

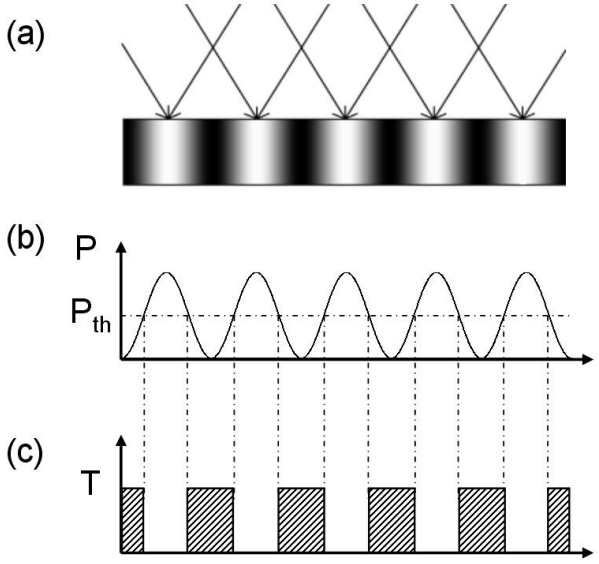

Figure A.3: Scheme of fabricating photoresist grating with rectangular profile: (a) interference of the beams; (b) the profile of the modulated illumination intensity; (c) the photoresist grating after exposure and development. P: Intensity of the illumination, P_{th}: the intensity threshold of the illumination, below which the photoresist can not be resolved in the developing solvent, T: thickness of the photoresist after development.

To fabricate photoresist gratings of a sub-micrometer periodicity, a thin layer of photoresist (SX AR-P 3500/6) is spin-coated on the sample and baked for 30 minutes at 90 °C. The sample is then mounted in the sample holder as shown in figure A.2 for exposure. The exposure time is determined by the actual irradiation density (∼700 mW/cm^2) and the thickness of the photoresist. Generally the sample is exposed for 10 - 20 seconds. Afterwards, the sample is immersed in a developing solvent. The developing solvent is often diluted in order to enhance the developing contrast. Photoresist gratings of a periodicity down to 350nm have been fabricated on glass substrates. Figures A.4 and A.5 display photoresist gratings of 720 nm and 420 nm periodicity, respectively, on glass substrates.

Fabricating submicron periodical photoresist gratings on a $LiNbO_3$ substrate is more challenging due to the much higher refractive index contrast between $LiNbO_3$ (∼2.2) and photoresist (∼1.6). With such a high index contrast, the light is reflected by the interface between photoresist and $LiNbO_3$, as well as by the rear surface of the $LiNbO_3$ substrate. The back-reflected light disturbs the interference pattern of the incident light, resulting in an inhomogeneous interference pattern. Another challenge is to create a photoresist grating of a thickness larger than 1.5 μm, because the irradiation density decreases with the depth due to the absorption in the photoresist. This results in either an uncleared surface (when it is not developed sufficiently) or a decreased height of the remaining photoresist (when it is developed for a longer time). Both situations are detrimental for subsequent applications such as periodical poling (see section 6.1.2). Figure A.6 displays a photoresist grating of 720 nm periodicity on a $LiNbO_3$ substrate.

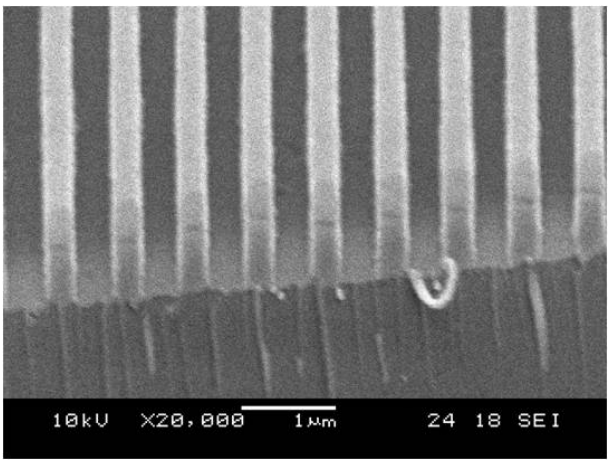

Figure A.4: Photoresist graing of 720nm periodicity on a glass substrate.

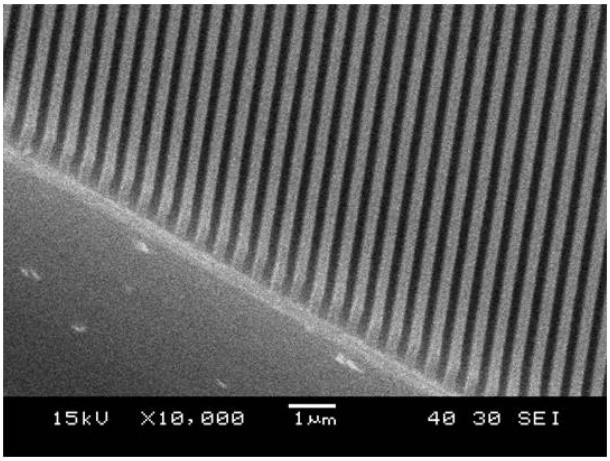

Figure A.5: Photoresist graing of 420nm periodicity on a glass substrate.

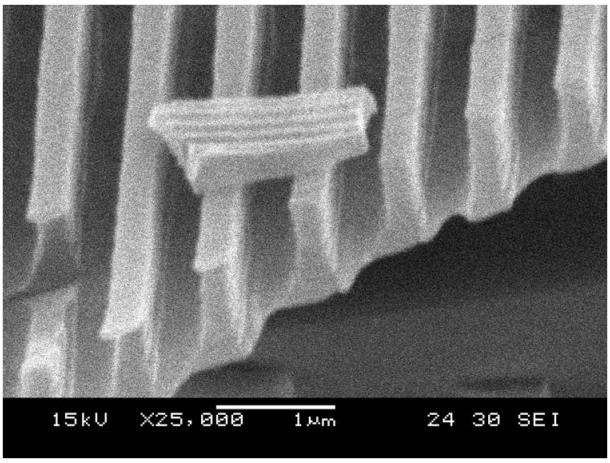

Figure A.6: Photoresist graing of 720nm periodicity on a $LiNbO_3$ substrate.

Bibliography

[1] Y. Kokubun, "High index contrast optical waveguides and their applications to microring filter circuit and wavelength selective switch," *IEICE Tran. Electron.*, vol. E90-C, p. 1037, 2007.

[2] http://cudos.org.au/content/view/5/39/.

[3] H. Hu, R. Ricken, and W. Sohler, "Lithium niobate photonic wires," *Optics Express*, vol. 17, p. 24261, 2009.

[4] H. Hu, D. Bchter, R. Ricken, and W. Sohler, "Periodically poled lnoi photonic wires," in *The proceedings of european conference of integrated optics' 2010*, 2010.

[5] B. T. Matthias and J. P. Remeika, "Ferroelectricity in the ilmenite structure," *Rhys. Rev.*, vol. 76, p. 1886, 1949.

[6] K. Nassau, H. J. Levinstein, and G. M. Loiacono, "Ferroelectric lithium niobate. 1. Growth, domain structure, dislocations and etching," *J. Chem. Phys. Solids*, vol. 27, p. 983, 1966.

[7] K. Nassau, H. J. Levinstein, and G. M. Loiacono, "Ferroelectric lithium niobate. 2. Preparation of single domain crystals," *J. Chem. Phys. Solids*, vol. 27, p. 989, 1966.

[8] S. C. Abrahams, J. M. Reddy, and J. L. Bernstein, "Ferroelectric lithium niobate. 3. Single crystal X-ray diffraction study at 24 °C," *J. Chem. Phys. Solids*, vol. 27, p. 997, 1966.

[9] S. C. Abrahams, W. C. Hamilton, and J. M. Reddy, "Ferroelectric lithium niobate. 4. Single crystal neutron diffraction study at 24 °C," *J. Chem. Phys. Solids*, vol. 27, p. 1013, 1966.

[10] S. C. Abrahams, W. C. Hamilton, and J. M. Reddy, "Ferroelectric lithium niobate. 5. Polycrystal X-ray diffraction study at 24 ° and 1200 °C," *J. Chem. Phys. Solids*, vol. 27, p. 1019, 1966.

[11] T. Izuhara, R. Roth, R. M. Osgood, S. Bakhru, and H. Bakhru, "Low-voltage tunable te/tm converter on ion-sliced lithium niobate thin film," *Electron. Lett.*, vol. 39, p. 1118, 2003.

[12] Y. Nishida, H. Miyazawa, M. Asobe, O. Tadanaga, and H. Suzuki, "0-dB wavelength conversion using direct-bonded QPM-Zn:$LiNbO_3$ ridge waveguide," *IEEE Photon. Technol. Lett.*, vol. 17, p. 1049, 2005.

[13] H. Hu, R. Ricken, W. Sohler, and R. B. Wehrspohn, "Lithium niobate ridge waveguides fabricated by wet etching," *IEEE Photon. Technol. Lett.*, vol. 19, p. 417, 2007.

[14] T. Sugita, K. Mizuuchi, K. Yamamoto, K. Fukuda, T. Kai, I. Nakayama, and K. Takahashi, "Highly efficient second-harmonic generation in direct-bonded MgO:$LiNbO_3$ pure crystal waveguide," *Electron. Lett.*, vol. 40, 2004.

[15] R. U. Ahmad, F. Pizzuto, G. S. Camarda, R. L. Espinola, H. Rao, and R. M. O. Jr., "Ultracompact corner-mirrors and T-Branches in Silicon-on-Insulator," *Photon. Tech. Lett.*, vol. 14, p. 65, 2002.

[16] Y. A. Vlasov and S. J. McNab, "Losses in single-mode silicon-on-insulator strip waveguides and bends," *Opt. Express*, vol. 12, p. 1622, 2004.

[17] P. Rabiei and W. H. Steier, "Lithium niobate ridge waveguides and modulators fabricated using smart guide," *Appl. Phys. Lett.*, vol. 86, p. 161115, 2005.

[18] A. Guarino, G. Poberaj, D. Rezzonico, R. Deglinnocenti, and P. Guenter, "Electro-optically tunable microring resonators in lithium niobate," *Nature Photonics*, vol. 1, p. 407, 2007.

[19] G. Poberaj, M. Loechlin, F. Sulser, A.Guarino, J. Hajfler, and P. Gnter, "Ion-sliced lithium niobate thin films for active photonic devices," *Optical Materials*, vol. 31, p. 1054, 2009.

[20] M. M. Fejer, G. A. Magel, and D. H. Jundt, "Quasi-phase-matched second harmonic generation: truning and tolerances," *IEEE Journal of Quantum Electronics*, vol. 28, p. 2631, 1992.

[21] E. J. Lim, M. M. Fejer, and R. L. Byer, "Second-harmonic generation of green light in periodically poled planar lithium niobate waveguide," *ELectronics Letters*, vol. 25, p. 174, 1989.

[22] J. Webjorn, F. Laurell, and G. Arvidsson, "Fabrication of periodically domain-inverted channel waveguides in lithium niobate waveguide," *Journal of Lightwave Technology*, vol. 7, p. 1597, 1989.

[23] M. Yamada, N. Nada, and M. Saitoh, "First-order quasi-phase matched $LiNbO_3$ Waveguide periodically poled by applying an external field for efficient blue second-harmonic generation," *Appl. Phys. Lett.*, vol. 62, p. 435, 1993.

[24] K. Mizuuchi, K. Yamamoto, and M. Kato, "Harmonic blue light generation in X-cut MgO:$LiNbO_3$ waveguide," *Electron. Lett.*, vol. 33, p. 806, 1997.

[25] T. Sugita, K. Mizuuchi, Y. Kitaoka, and K. Yamamoto, "Ultraviolet light generation in a periodically poled MgO:$LiNbO_3$ waveguide," *Jpn. J. Appl. Phys.*, vol. 40, p. 1751, 2001.

[26] T. Kishino, R. F. Tavlykaev, and R. V. Ramaswamy, "70+ μ m deep domain inversion in X-cut $LiNbO_3$ and its use in a high-speed bandpass integrated-optic modulator," *Appl. Phys. Lett.*, vol. 76, p. 3852, 2000.

[27] S. Sonoda, I. Tsuruma, and M. Hatori, "Second harmonic generation in a domain-inverted MgO-doped $LiNbO_3$ waveguide by using a polarization axis inclined substrate," *Appl. Phys. Lett.*, vol. 71, p. 3048, 1997.

[28] S. Sonoda, I. Tsuruma, and M. Hatori, "Second harmonic generation in electric poled X-cut MgO-doped $LiNbO_3$ waveguides," *Appl. Phys. Lett.*, vol. 70, p. 3078, 1997.

[29] K. Mizuuchi, T. Sugita, K. Yamamoto, T. Kawaguchi, T. Yoshino, and M. Imaeda, "Efficient 340-nm light generation by a ridge-type waveguide in a first-order periodically poled MgO:$LiNbO_3$," *Opt. Lett.*, vol. 28, p. 1344, 2003.

[30] F. Généreux, G. Baldenberger, B. Bourliaguet, and R. Vallée, "Deep periodic domain inversion in X-cut $LiNbO_3$ and its use for second harmonic generation near 1.5 μm," *Appl. Phys. Lett.*, vol. 91, p. 231112, 2007.

[31] P. A. Franken, A. E. Hill, C. W. Peters, and G. Weinreich, "Generation of optical harmonics," *Phys. Rev. Lett.*, vol. 7, p. 118, 1961.

[32] T. Suhara and M. Fujimura, *Waveguide nonlinear-optic devices*. Springer-Verlag, 2003.

[33] T. Tamir, E. Garmire, J. M. Hammer, H. Kogelnik, and F. Zernike, *Topics in applied physics: Integrated optics*. Springer-Verlag, 1979.

[34] D. A. Kleinman, "Nonlinear dielectric polarization in optical media," *Phys. Rev.*, vol. 126, p. 1977, 1962.

[35] J. A. Armstrong, N. Bloembergen, J. Ducuing, and P. S. Pershan, "Interactions between light waves in a nonlinear dielectric," *Phys. Rev.*, vol. 127, p. 1918, 1962.

[36] C. Canalias, V. Pasiskevicius, M. Fokine, and F. Laurell, "Backward quasi-phase-matched second-harmonic generation in submicrometer periodically poled flux-grown $KTiOP_4$," *Applied Physics Letters*, vol. 86, p. 181105, 2005.

[37] A. Christ, A. Eckstein, P. J. Mosley, and C. Silberhorn, "Pure single photon generation by type-i pdc with backward-wave amplification," *Optics Express*, vol. 17, p. 3441, 2009.

[38] G. I. Stegeman, D. J. Hagan, and L. Torner, "$chi^{(2)}$ cascading phenomena and their applications to all-optical signal processing, mode-locking, pulse compression and solitons," *Optical and Quantum Electronics*, vol. 28, p. 1691, 1996.

[39] M. Garcia-Granda, *High bandwidth integrated optical ridge guide modulator*. PhD thesis, University of Oviedo and Univesity of Paderborn, 2009.

[40] Y. Nishida, H. Miyazawa, M. Asobe, O. Tadanaga, and H. Suzuki, "Direct-bonded QPM-LN ridge waveguide with high damage resistance at room temperature," *Electron. Lett.*, vol. 39, p. 609, 2003.

[41] H. Hu, R. Ricken, and W. Sohler, "Etching of lithium niobate: micro- and nanometer structures for integrated optics," in *Topical meeting "Photorefractive materials, effects and devices - control of light and matter"*, 2009.

[42] S. Ganesamoorthy, M. Nakamura, S. Takekawa, S. Kumaragurubaran, K. Terabe, and K. Kitamura, "A comparative study on the domain switching characteristics of near stoichiometric lithium niobate and lithium tantalate single crystals," *Materials Science and Engineering B*, vol. 120, p. 125, 2005.

[43] D. Hofmann, *Nichtlineare, integriet optische Frequenzkonverter fuer das mittlere Infrarot mit periodisch gepolten Ti : $LiNbO_3$-Streifenwellenleitern*. PhD thesis, University of Paderborn, 2001.

[44] G. D. Miller, *Periodically poled lithium niobate: modeling, fabrication, and nonlinear-optical performance*. PhD thesis, Stanford University, 1998.

[45] R. Regener and W. Sohler, "Loss in low-finesse Ti:$LiNbO_3$ optical waveguide resonators," *Appl. Phys. B*, vol. 36, p. 143, 1985.

[46] P. Ferraro, S. Grilli, and P. D. natale, eds., *Ferroelectric crystal for photonic applications: including nanoscale fabrication and characterization techniques*. Springer, 2009.

[47] G. Berth, *Visualisierung ferroelektrischer Domnenstrukturen in Lithiumniobat mittels konfokaler nichtlinearer Mikroskopie*. PhD thesis, University of Paderborn, Germany, 2009.

[48] H. Yamada, T. Chu, S. Ishida, and Y. Arakawa, "Si photonic wire waveguide devices," *IEEE Journal of Quantum Electronics*, vol. 12, p. 1371, 2006.

[49] M. Bruel, "Silicon on insulator material technology," *Electron. Lett.*, vol. 31, p. 1201, 1995.

[50] H. Hu, R. Ricken, and W. Sohler, "Large area, crystal-bonded $LiNbO_3$ thin films and ridge waveguides of high refractive index contrast," in *Topical Meeting "Photorefractive Materials, Effects and Devices - Control of Light and Matter", Bad Honnef*, 2009.

[51] A. C. Busacca, C. L. Sones, V. Apostolopoulos, R. W. Eason, and S. Mailis, "Surface domain engineering in congruent lithium niobate single crystals: A route to submicron periodic poling," *Applied Physics Letters*, vol. 81, p. 4946, 2002.

[52] E. Dulkeith, F. Xia, L. Schares, W. M. J. Green, and Y. A. Vlasov, "Group index and group velocity dispersion in silicon-on-insulator photonic wires," *Opt. Express*, vol. 14, p. 9, 2006.

[53] A. Sakai, G. Hara, and T. Baba, "Propagation characteristics of ultrahigh-Δ optical waveguide on silicon-on-insulator substrate," *Jpn. J. Appl. Phys.*, vol. 40, p. 383, 2001.

[54] D. Duchesne, P. Cheben, R. Morandotti, B. Lamontagne, D.-X. Xu, S. Janz, and D. Christodoulides, "Group index birefringence and loss measurements in silicon-on-insulator photonic wire waveguides," *Opt. Eng.*, vol. 46, p. 104602, 2007.

[55] A. C. Busacca, A. C. Cino, S. Riva-Sanseverino, M. Ravaro, and G. Assanto, "Silica masks for improved surface poling of lithium niobate," *Electron. Lett.*, vol. 41, p. 2, 2005.

[56] Y. J. Ding and J. B. Khurgin, "Backward optical parametric oscillators and amplifiers," *IEEE Journal of Quantum Electronics*, vol. 32, p. 1574, 1996.

[57] C. Canalias and V. Pasiskevicius, "Mirroless optical parametric oscillator," *Nature Photonics*, vol. 1, p. 459, 2007.

Acknowledgment

I would like to thank all the people who have helped me to make this work possible.

First of all, I would like to express my gratitude to Prof. Sohler, who had kindly accepted me as one of his Ph.D. students in his group nearly four years ago. I was fortunate to study in an internationally recognized "integrated optics group"led by him. This thesis work has been benefitted enormously from his guidance helpful discussions and advices. I have learned from him not only the science but also his passion and scientific attitude in the research.

This work was funded by the Deutsche Forschungsgemeinschaft (DFG) within the framework of the project "Materials World Network: Nanoscale Structure and Shaping of Ferroelectric Domains" in collaboration with four other research groups in Germany and US. I am thankful to DFG and the people who were involved in our collaboration and contributed many discussions and suggestions.

This work has been carried out in close collaboration with Dr. Hu. He developed the techniques of fabricating ridge waveguides and LNOI structure, provided excellent material platforms which enable novel poling techniques. He also kindly shared with me a lot of his technological experiences. I thank also Dr. Berth and Mr. Wiedemeier from Prof. Zrenner's group for characterizing ferroelectric domains in our samples using CLSM.

I would like to thank Dr. Suche and Dr. Herrmann for their help in my work. I have learned a lot from them in many aspects such as domain engineering, designing electric circuit for poling, characterization and etc.

During my experiments of fabricating waveguides and performing periodical poling, Raimund Ricken and Viktor Quiring had helped me a lot with the technologies. I thank them for their continuous support in the cleanroom.

I give special thanks to Mrs. Zimmermann for her invaluable help not only in all the official works but also in my everyday life in Paderborn. She helped me to deal with all sorts of problems which a foreigner could encounter here.

I would like to thank also my other friends who I met during these years, Sergey Orlov, Selim Reza, Ansgar Hellwig, Stephan Krapick, etc. Special thanks go to those who study with me in the same period of time, Daniel Buechter, Mathew George, Abu Thomas and Rahman Nouroozi, who have helped me in many academic aspects as well as in my everyday life.

Special thanks to Miguel who is extremely patient and caring, and companied me through the difficult moments during my Ph.D. time.

Finally, I want to thank my family, who are far far away and know "nothing" about physics, but they are always my spiritual support wherever I am.